UNIVERSITÀ DEGLI STUDI DI PADOVA

PHD COURSE ON INFORMATION ENGINEERING

Information and Communication Science and Technologies (I.C.T.)

XXXII CICLO

DEVELOPMENT OF PHOTOCURRENT AND OPEN CIRCUIT VOLTAGE DECAY MODELS FOR THE CHARACTERIZATION AND RELIABILITY STUDY OF BULK HETERJUNCTION SOLAR CELLS

Coordinator:

Prof. ANDREA NEVIANI

Supervisor:

Prof. *ANDREA CESTER*

PhD student:

LORENZO TORTO

ANNO ACCADEMICO 2018/2019

Index

Abstract

Renewable energies are nowadays one of the primary field of study of the entire scientific community. The most industrialized countries already make a strong use of alternative energy sources (geothermal energy, wind energy, solar energy, ...), and it would be desirable that this example would be followed by the countries of the whole world. In order to provide a widespread diffusion of renewable energy, a big effort must be done by the scientific research both to improve efficiency and to reduce the fabrication and maintenance cost of those facilities which are suitable for energy production. Electronics, and in particular microelectronics engineering, covers one of the biggest role in this endeavor. In particular, the research in photovoltaic technologies has already led to a massive diffusion of photovoltaic facilities, both for solar field applications, and for domestic-applications. Indeed, the research for new sources of alternative energies is still far from over. During the last decade, for example, the third generation photovoltaic has begun to be developed. Devices such as organic solar cells (which is the main argument of this work) and hybrid solar cells belong to this new technology.

The strengths of organic solar cells reside in their peculiarities: among them, the most important are transparency and flexibility. This makes them very suitable for many applications, such as architectonical integration or wearable electronics. The possibility of integration of these cells on many fields compensate for the low efficiency that characterizes the devices. In a few words, the energy harvesting may come from a plenty of small sources rather than being concentrated in a single high efficiency power source. Despite the many advantages these technology has to offer (beyond the possibility to use them in many new different applications, it may be cited the extremely low cost of the devices), it still suffers from many weak points.

The most significant weak point is the low reliability, which inevitably brings to a low device lifetime. It is well-known that organic semiconductors are very sensitive to the interaction with environment agents like temperature, humidity and/or light. In fact, they act on the material causing oxidation, or even breaking the bonds between the atoms that form the material itself. Many efforts are still being done to study third generation photovoltaic materials and devices, but so much more is needed in order to extend the operative condition lifetime of the organic solar cells. From here it comes the necessity of studying new investigation procedures that may help to find solutions, which in turn may eventually lead to the reliability problem resolution. It is desirable that such techniques were nondestructive, so that they may be employed easily to monitor the health of the device during its operative life or on accelerated life tests.

In this scenario, this research activity aims to develop a methodology for the characterization and the reliability study of the bulk hetero junction solar cells, which represent one of the possible most important development of photovoltaic technology, and in particular of organic photovoltaic. In this work are proposed some methodologies that aim to fulfill this goal. In particular, two models have been developed, together with the description of an innovative measure: the open circuit voltage decay (OCVD).

The first model is presented in Chapter 3 and it is based on the analysis of the photocurrent density vs. voltage in an organic solar cell. It is based on other models already developed in literature (they are briefly described in Chapter 2), but it also takes into consideration some aspects that have never been taken into account before.

In the first place, it accounts for the band bending near the electrodes caused by a charge accumulation in the active layer. It has been found that these charge accumulations have a strong impact on the photocurrent produced by the device, but it is not strictly related to the charge accumulated-spatial shape. Instead, it is related to the total accumulated charge, which acts as a barrier during transport of the charges toward the electrodes.

Furthermore, the model explains several discrepancies that arise between experimental results and other models, previously presented in literature. Among them, it may be cited the value of the built-in voltage - which in the photocurrent vs. voltage curve does not correspond to the difference between the work functions of the electrodes - and the appearance of multiple inflections in the shape of the photocurrent. In particular, the first discrepancy is once again related to the band bending at the interfaces with electrodes, which cause a voltage drop in the bulk of the cell, and a modification of the active layer internal electric field. The second

discrepancy is shown to be strictly connected to the degradation of one interface with the electrode with respect to the other. This limits the extraction of one carrier with respect to other, de facto making selective one of the two contacts.

The second model, which is described in Chapter 4, is based on the analysis of an already mentioned innovative measurement technique, called open circuit voltage decay (OCVD). It is a nondestructive measurement that monitors the open circuit voltage decay transient starting from right after the moment at which the light incident on the solar cell is turned off. Thanks to the model, it has been shown that the shape of the voltage decay transient is related to the free charges separation and recombination mechanisms. The recombination mechanisms here considered are the bimolecular recombination and the trap-assisted recombination. The first is very common in the organic materials, while the second comes from the well-known recombination mechanisms mostly present in the inorganic solar cells. During the first part of the voltage decay (which shows the smoothest slope in all the decay) it has been shown that the main recombination mechanism is bimolecular. On the contrary, the second part of the decay (which is characterized by a sharper slope than the first) is dominated by the trap-assisted recombination.

Thanks to the OCVD model, many parameters describing the polymeric solar cells can be extrapolated. Among them, the model permits to extrapolate the recombination rates, the charge intrinsic concentration of the active layer and the Energy Gap of the materials that compose the active layer. Remarkably, this is a very important result, because the parameters are estimated via only purely electrical and non-destructive measurements.

In order to improve the fit and the precision of the parameters extrapolated by the OCVD model, the spatial non-constant charge distribution inside the active layer are also taken into account in the evaluation of the bimolecular and the trap assisted recombination (Chapter 6). In order to evaluate numerically their role on the voltage decay transient, some drift-diffusion simulations are used. Eventually, this analysis leads to an enhancement of the OCVD model, which leads to a better fit and a more accurate parameter evaluation, which does not require the computational effort of the drift diffusion simulation. The new model also permits to quantify the amount of charge accumulated at the electrode/organic interfaces, gaining further information about the electronic band structure of the solar cell, and in particular the alignment between the electrode work functions and the organic transport bands.

In order to understand perfectly how the variation of the parameters describing an organic solar cell impacts on the open circuit voltage decrease, several simulation are done using the

model. In particular, it is shown how the OCVD measurements change by varying the bimolecular and trap-assisted recombination rates, the barrier with electrodes height and the temperature.

The second part of the work makes large use of the models developed in the first part. In particular, they are applied to experimental data obtained from solar devices.

Chapter 5 presents two case studies of application of two models.

- In the first study, the two models are used to characterize four types of solar cells. The analysis aims to highlight the differences between these devices.

  The four types of solar cells differs from the donor polymer present in the active layer. On each class of devices are performed several photocurrent and open-circuit voltage-decay transient measurements. The measurements were performed at different temperature and during different moment of some stressing procedures.

  Using the two models, several information about the recombination mechanisms that undergo inside the active layer and about the band diagram of the organic solar cells blend (active layer) are extrapolated. By analyzing and comparing the data obtained by means of the OCVD transients and by means of the conventional DC measurements in the four polymers-based solar cells, the origin of the lower performance associated to some devices with respect to others are identified.

  In particular, it is discovered that the reason why some devices do not fail during strong reverse bias electrical stress resides in the high lifetime of the charges, which do not undergo trap-assisted recombination even after a long period of stress. Besides, at the same time, these device do not significantly increase the rate at which the free charges are subjected by bimolecular recombination.

  Temperature-based experimental measurements allows to extrapolate the band diagram of the materials that compose the solar cells. This results is then extended to the estimation of the band diagram of the entire device in Chapter 6.
- In the second case, the models are used to monitor the condition of some cells during accelerated life tests. This permits to see what is the main degrading factor that characterize the analyzed solar cells.

The stresses that are used are of multiple nature (electrical, thermal, light soaking), and they aim to simulate the stressing condition an organic solar cell may undergo during its normal operation.

The analysis made by means of the models on the experimental results made during accelerated life tests shows that the electrical stress only damages the active layer by reducing the polaron generation rate, the polaron separation probability and the carrier lifetime. From the analysis of the photocurrent shape it has also been observed that the thermal stress also degrades the anode interface.

Chapter 1 **Introduction**

The importance of the research in the photovoltaic field is demonstrated by the many worldwide conferences and journals and by the conspicuous funding allocated in its favor. In fact, photovoltaic is one of the primary concerns in the scientific community, due to the interest demonstrated by economy and politics, and being one of the solutions to climate change problem.

The interest is very well justified. In fact, the Sun is one of the biggest source of renewable energy in the world: it has been estimated that the one-year energy received by emerged continents (including a 65% loss by atmosphere and clouds) is more than 1500 times larger than the one-year energy world consumption [Per09]. It is not a surprise, then, that the energy produced by photovoltaic technologies has exponentially increased during the last years.

From an economic point of view, photovoltaic is an important alternative to the constantly increasing cost of non-renewable energy (like fossil fuels). This nurtures the whole world interest on renewable energies, be them solar energy, geothermal energy, wind energy and so on. Furthermore, it would be desirable to get free from the dependence on fossil fuels due to the strong relation of their cost and of their availability to political and to economic crisis.

In addition, non-renewable energy sources have a strong impact on the environment, due to the pollution they cause. Instead, due to the fact that photovoltaic is one of the most promising renewable energies, it is also one of the most attractive. In strict connection with this reason, photovoltaic will be of great help to humanity in their fight against the global warming problem. In order to address it, in fact, the European Union climate and energy framework has set three key targets to achieve by 2030:

- The emissions must be cut by at least 40% by 2030, with respect to the emissions levels of 1990. This will enable the EU countries to move towards a low-carbon economy and to implement its commitments under the Paris Agreement (which aims to avoid dangerous climate change and to limit global warming to well below 2°C, pursuing efforts to limit it to 1.5°C).
- The total energy consumption of EU must be composed of at least 32% from renewable energy. The original target was set at least at 27%, but it was revised upwards in 2018.
- Energy efficiency must improve at least of 32.5% by 2030. Initially it was set to 27%, but it was revised upward in 2018.

Without any doubts, photovoltaic will contribute to make these goals easier to achieve, and for this reason it is mandatory to study it in all of its forms. Conventional photovoltaic is of great help in pursuing the EU targets because of its high efficiency and high reliability (developed during decades of studies). Unfortunately, it has some disadvantages, which are mainly related to the cost of photovoltaic panels: in fact, in order to fabricate them, expensive equipment and complex procedures are required. In fact, they need high vacuum atmosphere and high temperatures (silicon melds at 1414°C). In addition, the energy payback time is on the order of years.

An alternative to inorganic photovoltaic is organic III generation photovoltaic, which is a younger and less expensive technology due to its lower fabrication costs and to its better payback time, which is estimated to be of 6 months in Mediterranean countries and 9 months in Northern European countries [Kre14]. This generation of photovoltaic may be divided into two main classes: organic photovoltaic and hybrid photovoltaic, depending on their structure and on the materials on which the devices are composed.

Organic photovoltaic is divided into two sub-categories:

- Polymeric solar cells: the active layer of these devices contains at least one polymer. When the active layer is based on two polymers, the device is an all-polymer solar cell.
- Small molecules solar cells: the active layer of the solar cells is generally composed of small molecules (characterized by a defined structure and a defined molecular weight).

Hybrid photovoltaic is composed of two types of solar cells as well:

- Dye sensytized solar cells (DSSC): their working principle is based on electrochemical reactions, which are allowed thanks to the presence of an organic dye material.
- Perovskite-based solar cells: these devices use both organic and inorganic materials, and can be seen as the evolution of the electrochemical reaction-based organic solar cells. Organic materials (in particular polymers) are mostly used as transport layer for charges, while the Perovskite is the inorganic material responsible for the photogeneration.

Among the above mentioned organic solar cells classes, this work is focused on the study of polymeric solar cells, also called bulk hetero junction solar cells (the name is due to the presence of an active layer in the bulk of the device. Specifically, it forms a relatively large junction area between two materials, for instance a polymeric material and a small molecule-based material). These organic solar cells are made of one or more polymers sandwiched between two transparent and conductive electrodes. The working principle is somewhat similar to that of inorganic solar cells, even though there are some differences [Hop15]. Details about the working principles and about the weak points of this technology will be described throughout all this work.

1.1 Advantages and disadvantages of organic photovoltaic

Organic photovoltaic has been taken in serious consideration by the European Union, which has identified it as one of the key factors that will contribute to achieve the 2030 goals. In fact, organic photovoltaic may offer a strong contribution to the energy production of the next years, which might become even comparable to the energy produced by Silicon-based inorganic solar cells. This in spite of the low efficiency that characterized organic photovoltaic during the first years of its development. It is clear from Figure 1.1 that organic photovoltaic is able to reach an efficiency value comparable to the values obtained by Silicon-based solar cells. During the last years, in fact, the efficiency of the organic solar cells increased very much [Nre19], [Kim06], [Sch13], [Zha15]. For example, some Perovskite-based solar cell prototypes have reached 25% efficiency, while polymeric solar cell prototypes have reached 16% efficiency. Of course, the data reported in Figure 1.1 refer to prototypes, and it is plausible that industrial organic solar cells will be characterized by a far lower efficiency. Anyway, this does not represent a real obstacle to their success at all. In fact, organic photovoltaic does not aim to overcome efficiency levels of inorganic photovoltaic technology. Instead, it aims to produce energy in cases where inorganic photovoltaic could not. This thanks to the peculiarities that characterize organic photovoltaic. Among them:

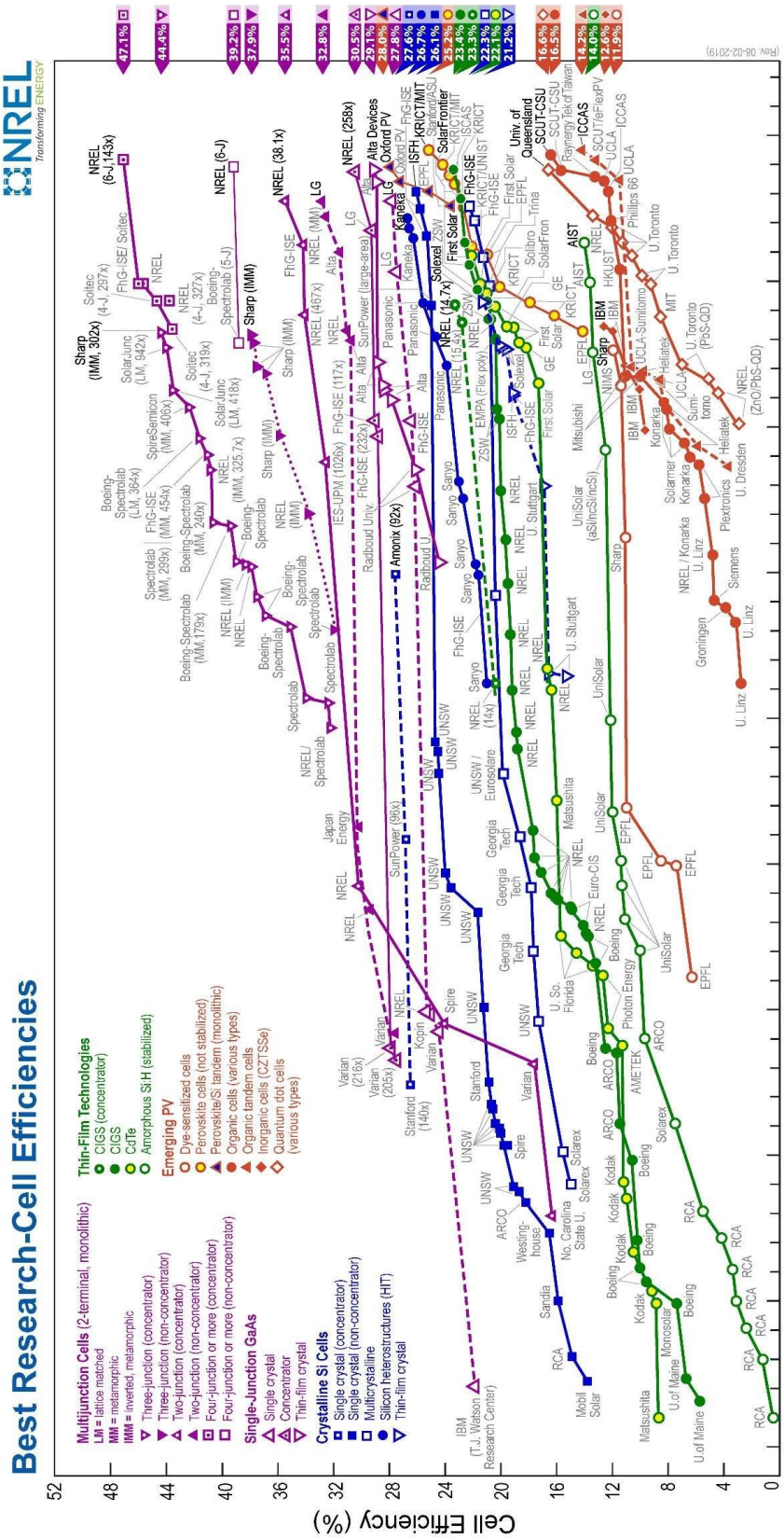

Figure 1.1 Efficiency record evolution of the of all the types of solar cells developed from 1975 to 2020. Organic solar cells can be found starting from 2010 [Nre19].

- Architectonic advantages: organic materials permit to realize colored and semi-transparent devices, which can be modeled in any shape. This allows to use them in several different places, like building facades, windows, greenhouse roofs and so on. Noticeably, these applications are possible only using organic photovoltaic, and would be impossible for their inorganic counterpart.
- Flexibility: the materials used to fabricate organic solar cells grants flexibility. This peculiarity allows their integration in new particular places. For instance, they might be applied to clothes, bags and so on.
- Reduced costs: as already mentioned, organic-based technology is less expensive than inorganic-based one. This thanks to the fabrication procedures used, which are much simpler and cheaper. In fact, the fabrication process are based on processes used in industrial typography. In particular, it is based on the deposition of organic materials by means of printers or similar techniques. For more information about the fabrication techniques see [Kre09]
- Indoor application: organic materials are very suitable for indoor applications. In fact, their efficiency is good even at low illumination level, allowing to use the organic technology even inside buildings.

In other words, the strength of organic solar cells does not reside on the efficiency, but rather on their potentiality of energy harvesting. This thanks to the organic solar cells peculiarities, which make them usable in contests where energy would be otherwise be wasted (think for instance to the energy passing through windows during hot summer days).

Nevertheless, organic solar cells have some limits, and (almost surprisingly) low efficiency does not fall within them. In fact, the biggest problem that afflicts organic photovoltaic is the low device reliability in time, which causes their extremely fast degradation. This is due to the high sensibility of the organic materials to ultraviolet light and to blue light coming from the Sun, as well as to temperature and to humidity. In addition, the devices may suffer from voltage bias polarization kept for long periods of time. See [Jør08] [Jør12] [Zha09] for more information.

For all these reasons, it is clear that in order to bring organic solar cell to their success, it is necessary to extend the knowledge of their working principles and on their degradation mechanisms [Kre13]. This will allow to find a way to fix the problems that characterize these solar devices, and to develop more reliable organic solar cells.

1.2 Aim of this work

The main aim of this work is to develop a methodology for the characterization and the reliability study of the bulk heterojunction solar cells (i.e. polymeric solar cells). As it was said previously, one of the biggest goal that the scientific community should achieve is to extend the reliability of the organic solar cells, preventing a too fast degradation and ensuring their good efficiency. In order to do this, it is necessary to find an easy and non-invasive way of monitoring the solar devices, and to extrapolate as many significant information as possible about the device. In this is provided an innovative and simple approach to accomplish these results.

In particular, the main argument of this work regards an innovative measurement technique, the open circuit voltage decay. The measurement was initially developed in other works, see for example [Zab03]. It has the advantage of being a very simple measurement to be implemented, and its results treatment provides very important information about the device. Equally important is the fact that this measurement is absolutely non-invasive: it can be performed even during the normal operation of the device and, due to its simplicity, it does not damage the solar cell. In fact, it requires only to monitor the decay transient of the open circuit voltage once the incident light is turned off.

In order to study the results obtained by the open circuit voltage decay measurements, an analytical model based on the voltage decay transient will be developed. Its main goal is to extrapolate information about the degradation of a solar cell, as well as about the different peculiarities of several devices made of different materials and/or structure.

The open circuit voltage model will be supported by the analysis of current vs. voltage measurements produced by a solar cell under illumination. In particular, the current will be analyzed by means of an analytical model which will provide information about the working mechanisms of the solar devices. Noticeably, also this approach is a non-invasive method, which can be used even during the normal operating condition of the device.

1.3 Summary

This work is organized in five main chapters. In the following, these chapters will be listed and briefly described, in order to give a comprehensive picture of all the work done.

- Chapter 2 gives some basic concepts about organic electronics and organic chemistry. The information given here are helpful to understand the next chapters, but it does not seek to give information about organic electronics in

general (the interested reader may refer to the very large number of papers that can be found in literature. Some of them are listed in this work in the end of each chapter).

In particular, it will be given information about the working principle of the bulk hetero junction solar cells, as well as terminology used throughout all this work.

In the second part of this chapter, a comprehensive picture of organic photovoltaic state of the art will be given. In particular, three models will be described. They are fundamental to understand the arguments of the following chapters, onto which most of the work is based.

- Chapter 3 describes a photocurrent model which extrapolates some typical parameters of the organic solar cell. This chapter will heavily use the terminology and the concepts introduced in Chapter 2. In fact, the model developed here can be intended as an evolution of the previously described models. The main peculiarities of this model regard the extrapolation of information about polaron recombination and separation, as well as the free charges of the organic solar cells analyzed.
- Chapter 4 introduces the open circuit voltage decay (OCVD) model. In the first part of this chapter the measure will be described, while the second part analyzes the OCVD from an analytical point of view. The transient voltage curves will be fitted by means of an analytical model here developed, and the characterizing parameters of the cell will be extrapolated. In the last part of the chapter, the model will be validated using a reference device whose active layer is made of standard polymers.
- Chapter 5 uses the model developed in Chapter 3 and 4 to analyze some experimental data obtained from different solar cells. The chapter may be thought as divided into two main parts.

  The first aims to analyze several solar cells with identical structure, but with four different active layer materials. The main differences highlighted by the model applied to OCVD measurements between each device will be shown.

  The second part is focused on the reliability study of polymeric solar cells. The cells have a slightly different structure from those studied in the first part of the chapter, and the analysis will be mostly focused on the measurement results obtained during accelerated stresses of different nature.

  This chapter is intended to give a practical application example of the model, and to show its potentiality.

- Chapter 6 describes an evolution of the OCVD model described in Chapter 5 to account for the non-uniform charge distribution within the active layer. In particular it will introduce some new corrective hypotheses regarding the charge distribution inside the active layer during the voltage decay. This will lead to a better voltage decay curve fit and to a better parameters extrapolation.
  At the end of the chapter, the model will be validated using some experimental data. Furthermore, some important results will be shown about, for instance, the extrapolation of the complete device band diagram.

1.4 References

[Hop15] H. Hoppe, N.S. Sariciftci, Organic solar cells: An overview, J. Mater. Res. 19 (2011) 1924–1945. doi:10.1557/JMR.2004.0252.

[Jør08] M. Jørgensen, K. Norrman, and F. C. Krebs, "Stability/degradation of polymer solar cells," Sol. Energy Mater. Sol. Cells, vol. 92, no. 7, pp. 686–714, Jul. 2008.

[Jør12] M. Jørgensen, K. Norrman, S. a. Gevorgyan, T. Tromholt, B. Andreasen, and F. C. Krebs, "Stability of polymer solar cells," Adv. Mater., vol. 24, no. 5, pp. 580–612, 2012.

[Kim06] Y. Kim, S. Cook, S. M. Tuladhar, S. A. Choulis, J. Nelson, J. R. Durrant, D. D. C. Bradley, M. Giles, I. McCulloch, C. Ha, M. Ree, "A strong regioregularity effect in self-organizing conjugated polymer films and high-efficiency polythiophene:fullerene solar cells", *Nature materials*, Vol. 5, p. 197-203, March 2006. doi: 10.1038/nmat1574

[Kre09] F. C. Krebs, "Fabrication and processing of polymer solar cells: a review of printing and coating techniques", Solar Energy Materials and Solar Cells (SOLMAT), Vol. 93, no. 4, p. 394 – 412, April 2009, doi: https://doi.org/10.1016/j.solmat.2008.10.004.

[Kre13] F.C. Krebs, M. Hoesel, M. Corazza, B. Roth, M. V. Madsen, S. a. Gevorgyan, et al., Freely Available OPV-The Fast Way to Progress, Energy Technol. 1 (2013) 378–381. doi:10.1002/ente.201300057.

[Kre14] F. C. Krebs, N. Espinosa, M. H. O. Sel, R. R. Søndergaard, M. Jørgensen, "25th anniversary article: rise to power – OPV – based solar parks", Advanced material, vol. 26, pp. 29-39, 2014.

[Mad14] M. V. Madsen, S. A. Gevorgyan, R. Pacios, J. Ajuria, I. Etxebarria, J. Kettle, N. D. Bristow, M. Neophytou, S. A. Choulis, L. Stolz Roman, T. Yohannes, A. Cester, P. Cheng, X. Zhan, J. Wu, Z. Xie, W.-C. Tu, J.-H. He, C. J. Fell, K. Anderson, M. Hermenau, D. Bartesaghi, L. Jan Anton Koster, F. Machui, I. González-Valls, M. Lira-Cantu, P. P. Khlyabich, B. C. Thompson, R. Gupta, K. Shanmugam, G. U. Kulkarni, Y. Galagan, A. Urbina, J. Abad, R. Roesch, H. Hoppe, P. Morvillo, E. Bobeico, E. Panaitescu, L. Menon, Q. Luo, Z. Wu, C. Ma, A. Hambarian, V. Melikyan, M. Hambsch, P. L. Burn, P. Meredith, T. Rath, S. Dunst, G. Trimmel, G. Bardizza, H. Müllejans, A. E. Goryachev, R. K. Misra, E. A. Katz, K. Takagi, S. Magaino, H. Saito, D. Aoki, P. M. Sommeling, J. M. Kroon, T. Vangerven, J. Manca, J. Kesters, W. Maes, O. D. Bobkova, V. A. Trukhanov, D. Y. Paraschuk, F. A. Castro, J. Blakesley, S. M. Tuladhar, J. Alexander Röhr, J. Nelson, J. Xia, E. A. Parlak, T. A. Tumay, H.-J. Egelhaaf, D. M. Tanenbaum, G. Mae Ferguson, R. Carpenter, H. Chen, B. Zimmermann, L. Hirsch, G. Wantz, Z. Sun, P. Singh, C. Bapat, T. Offermans, and F. C. Krebs, "Worldwide outdoor round robin study of organic photovoltaic devices and modules," Sol. Energy Mater. Sol. Cells, vol. 130, pp. 281–290, Nov. 2014.

[Nre19] National Renewable Energy Laboratory, https://www.nrel.gov/pv/cell-efficiency.html.

[Per09] R. Perez, M. Perez, *"A fundamental look at energy reserves for the planet"*, Jan 09, URL: http://asrc.albany.edu/people/faculty/perez/2015/IEA.pdf

[Sch10] J. Schafferhans, A. Baumann, A. Wagenpfahl, C. Deibel, and V. Dyakonov, "Oxygen doping of P3HT:PCBM blends: Influence on trap states, charge carrier mobility and solar cell performance," Org. Electron., vol. 11, no. 10, pp. 1693–1700, Oct. 2010.

[Zab03] A. Zaban, M. Greenshtein, and J. Bisquert, "Determination of the Electron Lifetime in Nanocrystalline Dye Solar Cells by Open-Circuit Voltage Decay Measurements", Chem. Phys. Chem., Vol. 4, p. 859–864, August 18, 2003.

[Zha09] J. Zhao, A. Swinnen, G. Van Assche, J. Manca, D. Vanderzande, and B. Van Mele, “Phase diagram of P3HT/PCBM blends and its implication for the stability of morphology.,” J. Phys. Chem. B, vol. 113, no. 6, pp. 1587–91, Feb. 2009.

[Zha15] Q. Zhang, B. Kan, F. Liu, G. Long, X. Wan, X. Chen, Y. Zuo, W. Ni, H. Zhang, M. Li, Z. Hu, F. Huang, Y. Cao, Z. Liang, M. Zhang, T.P. Russell, and Y. Chen, “Small-molecule solar cells with efficiency over 9%”, *Nature Photonics* Vol. 9, p.35–41, Nov. 2015, doi:10.1038/nphoton.2014.269

Chapter 2 Basic concepts on organic photovoltaic

2.1 Organic materials

The research activity on organic photovoltaic is focused on the study of organic solar cells. These devices are particular photovoltaic devices in which the active layer is made of organic materials, i.e. Carbon-based small molecules or polymers[1].

A molecule is a simple organic compound with a well-defined structure and dimension, and characterized by a specific molecular weight. Sometimes, when the molecule is characterized by big dimension and big molecular weight, it is named macromolecule.

In some cases, a macromolecule is characterized by the repetition of many standard molecules bound each other. These molecules might be intended as the base-unit that builds a macromolecule, and they are named monomers. Depending on the monomers number, the macromolecule assumes different names: when the number of monomers is well defined, the macromolecule is named oligomer. Otherwise, the macromolecule is named polymer.

In both oligomers and polymers, the monomers carbon atoms are bound each other by means of covalent bonds. Thus, the monomers form a sort of "chain", composed of a well-defined number of monomers for oligomers, or an undefined number of monomers for polymers. In particular, a polymer may be characterized by a huge number of monomers (varying from

[1] The organic solar cells that have already been developed employ many different materials. Sometimes (as in Perovskite-based solar cells) the devices are made by both organic and inorganic materials.

hundreds to thousands), and it may be characterized by a big molecular weight. Being composed of a large number of carbon atoms, both polymers and oligomers are a subsets of organic compounds.

In organic compounds one (or more) carbon atom is covalently bond to other carbons atoms or to different atoms (most commonly Hydrogen, Oxygen, or Nitrogen atoms). In particular, in oligomers and in polymers, the bonds formed between each monomer can be single, double or triple covalent bonds. Thus, each carbon atom is bound to four more atoms, in particular carbon, hydrogen, or atoms belonging to another molecule (similar or very different from the basic monomer).

In some cases, a particular structural unit named functional group can be bound to the molecular backbone of a polymer. When this happens, they may grant to the polymers several physical and/or chemical properties. For instance, some functional groups may enhance the polymer solubility, which is a very important property for a correct and easy fabrication of the organic-based electronic devices. Instead, other functional groups may modify the energy gap value, or enhance the agglomeration between two different polymers.

In this work only polymer-based devices will be analyzed. For this reason, in the following the attention will be focused onto these chemical species.

2.1.1 Polymers classification and representation

The polymers can be classified basing on the geometric shape of their Carbon main chain. In the following, a list of three different polymer categories will be shown:

- Linear polymers: the main Carbon chain is made of single monomers. Each monomer is rigidly bound to another, and the main Carbon chain forms a line. Generally, these polymers dispose themselves tidily.
- Branched polymers: the main Carbon chain has some pending side-“branching”. A material made of branched polymers is softer and less thick if compared to linear polymers-materials.
- Cross-polymers: these polymers form complicated ramifications, often intersecting each other. Materials composed by these kind of polymers are stiff and are characterized by an amorphous structure.

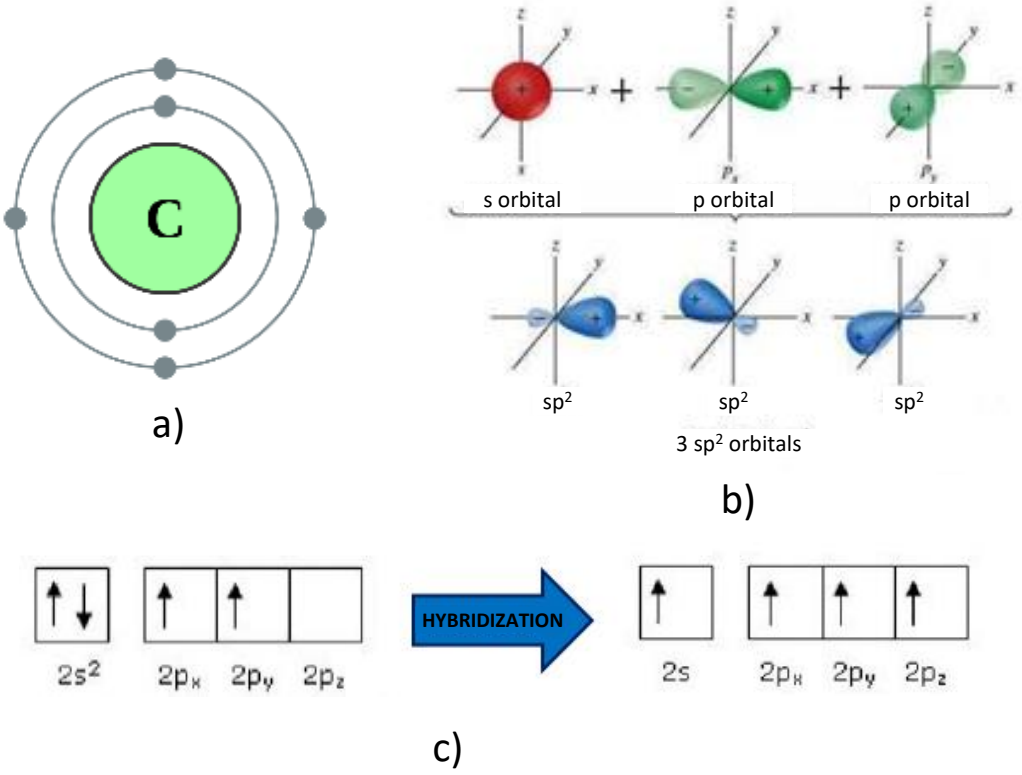

Figure 2.1 a) Schematic representation of the Carbon atom. b) Form of the sp^2-hybrid orbitals. c) Disposition of the electrons inside the orbitals. The arrows represent the spin of the electrodes.

2.2 Electronic behavior of the polymers

In this section, some basic concepts about organic electronics will be given. The interested reader may refer to any quantum mechanics text book for further details.

2.2.1 Carbon characteristics

Organic compounds are very frequent in nature, thanks to the carbon atom properties. It possess 6 electrons (disposed as shown in Figure 2.1(a)), with electronic configuration $1s^2 2s^2 2p^2$. This normally allows the atom to form two covalent bonds with other atoms. Nonetheless, in some specific cases (such as what happens for the Carbon atoms that form a polymer), the atom may form up to 4 bonds. In order to do this, the atom modify the shape of one, two or three of its orbitals (hybridization), allowing it to form a larger number of bonds with other atoms. This configuration is energetically more stable, making it a far more favorite situation. The form of the new orbitals can be obtained from Schrodinger equation. Depending on how many orbitals are hybridized, the following hybridization types can be defined:

- *sp hybridization*: one s-orbital and one p-orbital are hybridized.
- *sp^2 hybridization*: one s-orbital and two p-orbitals are hybridized.
- *sp^3 hybridization*: one s-orbital and three p-orbitals are hybridized.

Figure 2.1(b) shows the new shape of the orbitals after sp^2-hybridization, which a very common hybridization for carbon atoms forming a polymer. The hybridized atom now possess three hybridized orbitals and one non-hybridized orbital, and in each orbital only one electron can be found, as depicted in Figure 2.1(c). *sp^2* hybridization is very important for the polymers used in organic electronics, and this is due to the presence of a *p* non-hybridized orbital, whose orientation is orthogonal to the *sp^2*-hybridized orbitals, which are coplanar.

sp^2 hybridization is typical of those molecules in which it is possible to find double bonds (for instance C=C, C=O, ecc…). In these cases, Carbon forms two types of bond: the first is a double bond, formed when two different coplanar hybridized orbitals share an electron (σ bond). The second is a single bond made by two non-hybridized *p* orbitals (π bond). It is positioned on a plane which is parallel to the plane of the nuclei (and to the σ bond plane as well).

The double bond is always present in conjugated polymers, in which the main Carbon chain is made of single and double bonds alternating. In these structures, Carbon forms three bonds with other Carbon, and one bond with a Hydrogen (or with an atom of a functional group). π bonds are weaker that the σ bonds, thus π bonds can be broken more easily with respect to the σ bonds.

2.2.2 Bond energy in a molecule

Whenever an electron moves inside a crystal lattice, it is influenced by the periodic potential of the lattice itself. Quantum mechanics demonstrated that in crystalline solids there are some forbidden energy levels that no electron is allowed to possess inside a crystal lattice. In fact, electrons are only allowed to possess some well-defined energies which depend on the type of atoms that form the crystal lattice. A similar concept is valid also for organic materials like polymers, which are characterized by a periodic structure.

When a new bond is formed, the superimposition of the orbitals of the atoms involved in the bond form two new molecular orbitals, named bond orbital and an antibond orbital. They can be described mathematically by means of the Schrodinger equation as a linear combination of the

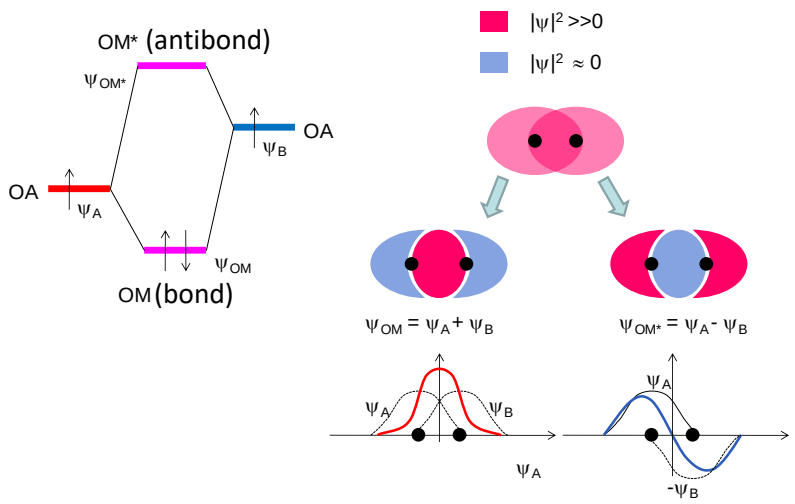

Figure 2.2 Schematic and simplified picture of the bond configuration when a new bond is formed.

atoms orbitals (see the simplified picture in Figure 2.2). In figure, the electron inside the s-s bond orbital is characterized by a wave function with a probability maximum in the space between the nuclei of the atoms (right part of Figure 2.2). On the contrary, the wave function of the anti-bond electron has a probability maximum placed outside the nuclei space. In the first case, the wave function suggests that electrons are present in the region between the nuclei, thus balancing the molecule charge and leading to a low energy configuration. In the second case (anti-bond), electrons do not neutralize the charge of the nuclei, thus the molecule is in a higher energy, and less stable, configuration (band diagram on the left part of Figure 2.2). The shape of the molecular orbitals depends on whether the forming atoms orbitals are σ or π. Of course, this is a simplified description of what quantum mechanics describe in more detail. Once again, this chapter only intends to give a qualitative description of the very complex arguments involved. The interested reader may refer to quantum mechanics text books for more details.

π bonds in a molecule are characterized by a lower energy with respect to the σ bonds. For this reason, π bonds are more delocalized and partially shared between the surrounding atoms. The superimposition of all the π orbitals forms something like a micro band of possible allowed levels very close in energy, which is called molecular orbital. The allowed energy levels number grows with the number of involved atoms. Among these levels it is possible to choose a particular level called Highest Occupied Molecular Orbital (HOMO) and a level called Lowest Unoccupied Molecular Orbital (LUMO). The first is associated to the highest energy level which is occupied by an electron, the latter is associated to the lowest energy level which is not occupied by any electrons.

The energy range between the HOMO level and the LUMO level is the polymer energy gap, and no charge is allowed to have an energy comprised in this energy range. Instead, for energies lower than the HOMO level and higher than the LUMO level there are two ranges of allowed energies, identified as HOMO and LUMO bands. The similarities with the band diagrams used for inorganic materials are clear: the HOMO band plays the role of the valence band, while the LUMO band plays the role of the conduction band.

2.2.3 Characteristics of the polymers depending on the Energy Gap

The polymer is strongly influenced by the Energy Gap. In fact, it affects many properties of the material, in particular the electrical and optical properties.

Electrical properties

Normally, an organic material is characterized by a very high energy gap, which gives to the material insulating properties.

Nevertheless, the properties of a polymer can be altered adding some extra-atoms (different from those bounded to the main Carbon chain), or adding some functional groups. This may alter the energetic position of the polymer energy bands, but it is necessary to ensure that the electronic delocalization remains unaltered, preventing a degradation of the material.

Optical properties

The optical properties of a polymer regards its behavior when it absorbs electromagnetic radiations (for instance, visible light). In fact, electromagnetic radiation may act in several different ways on a polymer: for example, it may generate free charges, or it may degrade (especially when spectrum contains a strong UV component, which may be extremely dangerous for an organic material).

Depending on the absorbed radiation frequency, the polymer has different reactions. Infrared light, for instance, acts on the bonds between atoms, while ultra violet light breaks the bond between atoms, generating free radicals which oxidize the polymers main chain. For this reason, UV light exposure is one of the major cause of the polymeric solar cell degradation.

The optical properties are related to the electrical properties by means of the Energy Gap of the material. In fact, the light that can be absorbed by a polymer must have an energy higher or equal to the Energy Gap itself ($h\nu \geq E_G$). On the contrary, low-energy light (i.e. lower than the material Energy Gap) cannot be absorbed, but it can be transmitted through the material, which results transparent to the corresponding light wavelength. For this reason, in order to investigate the optical properties of a polymer it is of fundamental importance to estimate its Energy Gap. In turn, it is important to understand to which physical properties the Energy Gap is related. In a polymer, the Energy Gap is related to four factors:

- To the aromatic rings present in the polymer.
- To the energy associated to the π bonds length.
- To the energy associated to the torsion angle that is formed between the polymer molecules.
- To the functional groups energy.

2.2.4 Fullerenes and PCBM

The core of a polymeric solar cell, as will be extensively discussed later, is the active region, which is a thin film made of a photoactive semiconductor material, generally sandwiched between to electrodes. Basically, it is made of two materials, an electron-acceptor material (for example PCBM, which is a small molecule as will be discussed in the following) and an electron-donor polymer (for example P3HT). The most used acceptor material in polymeric solar cells is PCBM, which is a particular material which belongs to the family of Fullerenes. Remarkably, Fullerens are no polymers: their structure is characterized by a finite and precise number of atoms, thus it is more correct to name PCBM a small molecule. Fullerenes are some of the most important class of materials in the industry of organic electronics (especially organic photovoltaics). Their structure is tridimensional and spherical, and it is made of several hexagonal and pentagonal small molecules, mainly composed of Carbon atoms (*buckyball* structure, see Figure 2.3).

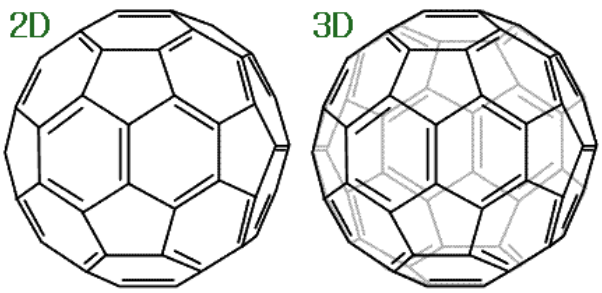

Figure 2.3 Fullerene graphic representation.

There exists many specific molecules belonging to the family of Fullerenes, each possessing a different functional group or a different numbers of hexagonal and pentagonal molecules. The first discovered Fullerene had 20 hexagons and 12 pentagons (60 double bonded atoms on the whole, from which derives the name C_{60}). Other versions of a similar macromolecule have got 70 or 84 Carbon atoms. C_{70}, for instance, is obtained adding a hexagonal ring in the equatorial *buckyball* region. This makes C_{70} structure more ovoid than spherical.

However, the most interesting Fullerene macromolecule in Organic photovoltaic is the C_{60}. Similarly to Graphene, in these macromolecules each Carbon is bonded to three Carbon atoms by means of covalent bonds, thanks to sp^2 hybridization. For this reason, C_{60} might be seen as a modification of a Graphene sheet wrapped on itself. Of course, it might be observed that - due to sp^2 hybrid orbitals coplanarity - this configuration should lead to a planar structure as well. In the case of C_{60}, though, hybridized orbitals are not exactly sp^2, but they are partially mixed with the p-orbital, whose axis is orthogonal to the sp^2 orbitals plan. This process is the main responsible for the curving of the sphere surface.

In C_{60}, each pentagonal ring is adjacent to a hexagonal ring, and each hexagon is adjacent to three pentagons and three hexagons (alternated on each side, see Figure 2.3). On those sides where a hexagon is adjacent to a pentagon, the bond between Carbon atoms is a single covalent bond. Instead, on those sides where two hexagons are adjacent, the bond is double covalent. In this configuration, each Carbon atom has three electrons on the σ bonds (like in Graphene sheets), and it has a partially hybridized p orbital orthogonal to the sphere surface.

Due to mixed - sp^2 hybridization, the sphere surface contains many delocalized electrons. This lends some semiconductor properties to the Fullerene macromolecules: in particular this heavily alters the electronic affinity of the molecule, allowing C_{60} to host up to 12 free electrons, making it an acceptor material.

Table 1 reports the molecular orbitals structure for C_{60} (see 2.2.2 for information about the molecular orbitals of a polymer). The first column indicates the energy levels, the second column indicates the corresponding maximum number of electrons the level may host, while the third column shows how many electrons are necessary to completely fill the energy levels (up to the number indicated by the corresponding line in the second column).

The 60 delocalized electrons completely fill the fourth energy level, while the fifth remains partially filled. In particular, the HOMO in this level is completely filled, while the LUMO remains empty (with an Energy Gap of 1.92eV, which is a value comparable to those of the inorganic crystals). Being the electronic affinity in C_{60} lower than the ionization potential, it is easier to reduce the molecule rather than oxidize it. For this reason, Fullerenes are considered very suitable materials for electrons transport in organic electronic devices.

Fullerenes macromolecules might be very useful in photovoltaic applications as acceptor materials. Unfortunately, those molecules have a strong drawback: they are insoluble. For this reason, a variation of C_{60} is used in organic solar cells: the above mentioned *PCBM* (Phenyl-C61-

Energy level	Electrons/states	Total
0	2	2
1	6	8
2	10	18
3	14	24
		26
		32
4	18	40
		42
		50
5	22	56
		60
		62
		66
		72
…	…	…

Table 1 C_{60} energy levels. The first column indicate the atom energy level, while the second column indicate how many electrons that level is capable of containing. The third column indicates the number of electrons necessary to completely fill the corresponding level (i.e. the one indicated in that line).

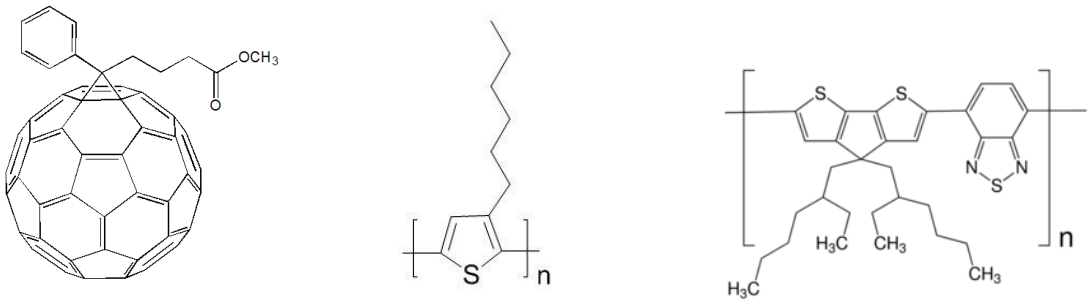

(a) (b) (c)

Figure 2.4 (a) PCBM molecular structure, (b) P3HT molecular structure, (c) PCPDTBT molecular structure.

butyric acid methyl ester). PCBM is a C_{60} macromolecule modified with the addition of a functional group (a benzene ring and an OCH_3 group), which makes C_{60} soluble in chlorobenzene. After the process of solubilization, the macromolecule can be mixed with other polymers such as P3HT. Figure 2.4(a)[2] shows the PCBM macromolecule. On the north pole of the sphere the functional group can be seen.

2.2.5 P3HT (3-hexylthiophene-2,5-diyl)

P3HT (3-hexylthiophene-2,5-diyl) is a polymer, generally mixed with PCBM inside the active layer of an organic solar cell. Its chemical structure can be observed in Figure 2.4(b), and it is an electron-donor material (i.e. it is a good hole conductor). It is a cheap material and its band gap is 1.9eV, which allows for the absorption of only the 27% of the solar spectrum power. In order to broaden the power absorption spectrum, it is possible to add another material as functional group, the PCPDTBT (*Poly[2,1,3-benzothiadiazole-4,7-diyl[4,4-bis(2-ethylhexyl)-4H-cyclopenta[2,1-b:3,4-b']dithiophene-2,6-diyl]]*). Its structure is shown in Figure 2.4(b). This polymer band gap is lower than in P3HT, and this allows for the photon absorption even in the infrared range.

2.3 Basic concepts in organic electronics

In the previous sections some general information about organic electronics were given. In particular, these information regarded the chemical structure of the polymers and some of their electrical characteristics. In this sections, some extra information will be given about organic electronics in general. In particular, the attention will be focused on the current conduction and on the current photogeneration.

2.3.1 Current conduction in an organic material

When an organic semiconductor is sandwiched between two electrodes, it may conduct electric charges, acting as a semiconductor. Current conduction is made of two phases: the carrier

[2] When a polymer is graphically represented, the Carbon atoms in the main chains are not shown, as well as Carbon-bound Hydrogen atoms. The Hydrogen atoms are not shown as well, because the Carbon-Hydrogen bond is very common in polymers. In particular, it can be found when no other atom is bounded to the main chain. The bonds between atoms are represented by a single, double or triple lines (depending on the covalent bond type). Instead, when another atom (different from Hydrogen) or molecule is bound to the main chain, it is necessary to represent both the chemical species and the covalent bond.

Furthermore, in the graphical representation of a polymer, only the repeated monomer is shown. Sometimes, it is represented among brackets, with a number stating how many times that monomer is repeated (in case of an oligomer), or an n when the monomer is repeated an undefined number of times (in the case of a polymer).

injection in the organic material and the carrier transport in the organic materials. These two phases takes some time to fulfill:

- Charge injection, which lasts a period of time T_{INJ} (related to the band alignment between the electronic bands of electrodes and the electronic bands of the organic film).
- Charge transport inside the organic material, which lasts a period of time T_{TR}.

Depending on the duration of these two phases, the current conduction inside an organic material is characterized by different properties. When $T_{INJ}>T_{TR}$, the conduction is limited by the charge injection in the contact (i.e. the injection takes more time than the transport inside the organic material). When $T_{INJ}<T_{TR}$, the conduction in the organic material is limited by the carrier velocity.

In the first case (contact-limited injection), the injection is limited by a potential barrier in the interface between organic material and the electrode. Current conduction exponentially depends on the barrier height (Φ_B) and on the applied voltage.

In the second case (transport-limited injection), the potential barriers at the interface between organic material and electrodes are very small. The current density is expressed by the drift current equation: $J = -\rho(x) \cdot \mu \cdot F(x)$, where ρ(x) is the carrier concentration in the film, μ is the charges mobility and *F(x)* is the electric field in the film. In this case, the solar cells work in a regime that may have the properties of both the two following cases, which should be intended as "limit case conditions":

- Ohmic regime: when the number of injected charges is much lower than the number of free carriers that are already present in the semiconductor, the total current is given by the pre-existing charges. The current density value is described by the drift current equation written above and the electric field is constant inside all the active layer. As in inorganic materials, the free charges number can be approximated to the charge given by the ionized atoms present inside the organic material. Current density is described by the following law[3], where N_D is the ionized atoms density and *L* is the organic material thickness:

$$J = qN_D\mu\frac{V}{L} \qquad (2.1)$$

[3] The equation comes from the drift current equation.

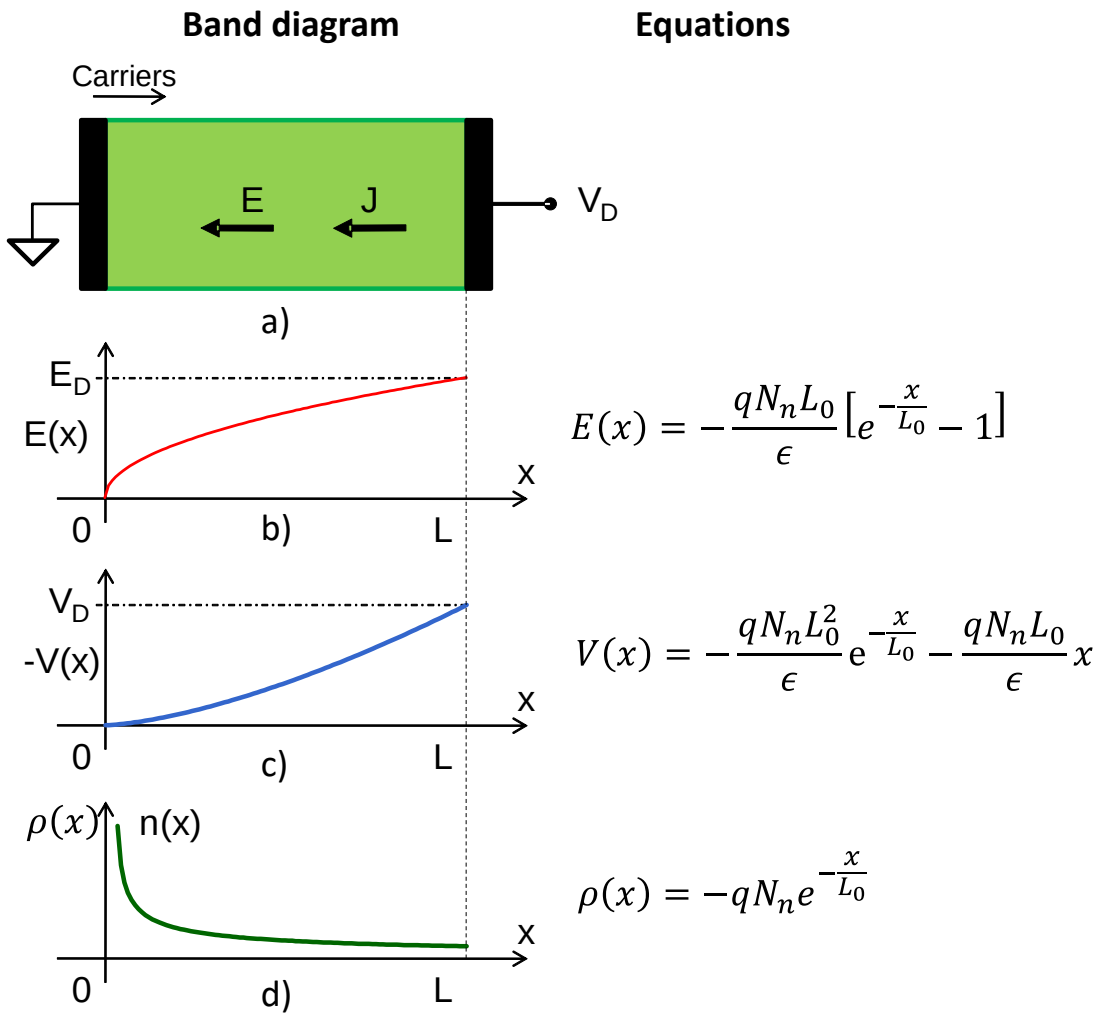

Figure 2.5 a) MIM system sketch: electrodes on both sides of the device are black, organic material is between the electrodes and it is green. b), c) and d) represent the electric field, potential and charge concentration behavior inside the organic layer, respectively. On the right are reported the equations that permit to calculate the electric field and the voltage as a function of the position inside the film (in the case of exponential charge distribution). The formulae on the right part of the figure shows the expression of electric field, voltage and charge density (ε is the dielectric constant of the material, L is the film thickness and q is the elementary charge).

- SCL regime (Space Charge Limited): in this condition, the pre-existing free charges are negligible if compared to the number of charges injected by the electrode, which determines the electric field and the potential profile in the active layer. Supposing that the organic material is interposed between two metallic electrodes (MIM system: Metal – Insulating material – Metal), it can be demonstrated that the current density dependence on the applied voltage V_D is expressed by this law:

$$J = \frac{9}{8}\mu\epsilon\frac{V_D^2}{L^3} \qquad (2.2)$$

Figure 2.5 shows the electric field, potential and charge density as function of the position inside the active layer. The charge concentration has an exponential distribution, and its maximum value is placed close to the electrode (x=0). Consequently, electric field and voltage are not constant inside the active layer.

When conduction is space charge-limited, the MIM system can be approximated to an RC circuit. The equivalent resistance value *R* depends on the applied voltage (inversed proportionality dependence), while equivalent capacitance depends on the dielectric constant and on metal thickness[4] (as if the MIM system were a plane capacitor).

2.3.2 Excitons generations and characteristics

In a molecule in its ground state all electrons are placed in the π orbitals of the HOMO band, while the LUMO band remains empty. For instance, the first line in Figure 2.6 shows a

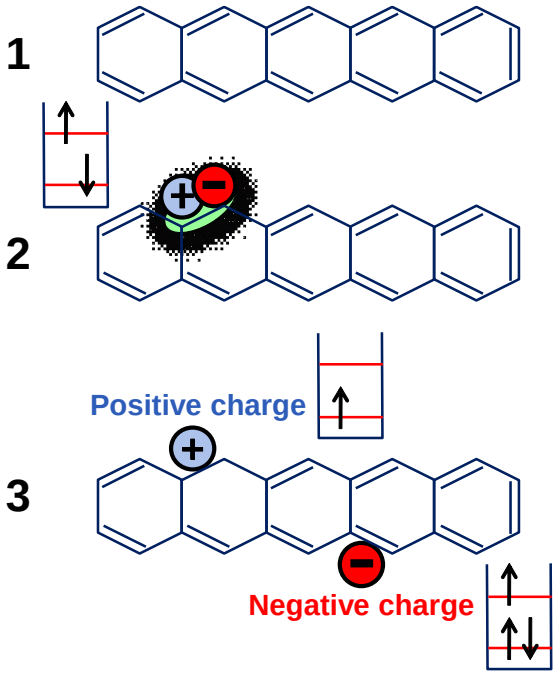

Figure 2.6 Exciton formation inside a Pentacene molecule

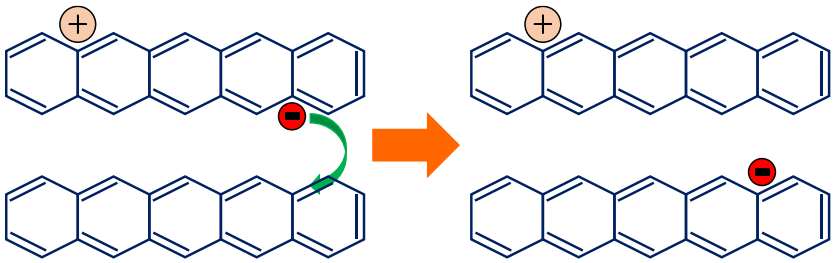

Figure 2.7 Exciton separation schematization

[4] The situation is similar to a plane capacitor, where C=Aε/d. A is the area of the electrodes, ε is the active layer dielectric constant, d is the active layer thickness.

Pentacene molecule in its ground state, in which there are no excited atoms. When the molecule absorbs a photon, an electron passes from the HOMO energy band to the LUMO energy band. The electron now occupies one of the anti-bond orbital π*, while an electron vacancy is left in the HOMO band. This situation is depicted in Figure 2.6, where the spin of the charges in the respective energy levels is represented as well. The electron and the hole are still bound together, forming a couple named exciton which can be approximated to an electrostatic dipole. An exciton is characterized by a spin value and an energy and its global charge is neutral. As will be explained better in the following, this is the first step of the creation of free electron/hole couples inside a polymeric solar cell.

The energy of an exciton depends on the presence of free charges inside the material (in fact the presence of a huge number of charges may shield the dipoles) and on its dielectric constant (which is related to the energy with a reverse-proportionality law). Generally, in organic materials the excitons are characterized by high binding energy. For this reason it is required a relatively huge amount of energy to break it. As a consequence, the electron and hole recombination could become easier than separation in some cases. This makes difficult the charge extraction induced by photons in an organic material, as will be discussed later.

2.3.3 Polarons

Under some circumstances, the electron or the hole of an exciton may pass into an orbital of an atom belonging to a different molecule (Figure 2.7). This is another step toward the formation of free charges inside a molecule, which can be extracted by the contacts. Before this phase, though, the electron/hole bound state must become another entity named polaron.

When an exciton loses an electron or a hole (i.e. when one of these particles moves from a molecule to another), the exciton becomes a polaron (i.e. a charged exciton). Similarly to an exciton, a polaron is an electron/hole bound state which influences the entire molecule it is placed on. In fact, when the electron passes into another molecule, the negative charge is not balanced by the respective hole. This induces a modification in the reticular structure of the molecule itself, and the entity of this deformation depends on the period of time the charge remains on the molecule and on the reaction time of the molecule itself. The spatial perturbation may extend even for tens of nanometers.

When a polaron is formed, three different phases come in succession:

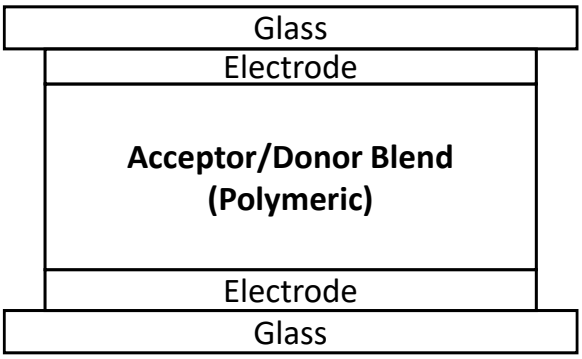

Figure 2.8 Schematic and basic structure of a polymeric solar cell. Each box represents a layer of the device. Electrodes are metallic layer or metallic grids, and in some cases there may be some additional layer between the active layer and the electrodes.

1. Electronic polaron: the charge generates an electric field that polarizes the electron cloud of the molecule. This phases lasts between *0.1fs* and *1fs*. The charge and the reticular deformation is called *electronic polaron*.
2. Molecular polaron: if the charge stays on the molecule after the formation of the electronic polaron, the electrons of the molecule begin to redistribute in order to minimize the total energy. The molecule is deformed and this situation begins between *1fs* and *10fs*.
3. Reticular polaron: the entire molecular lattice (not only on the region where the charge is placed) is deformed by the presence of the charge. This phase begins after *100fs*.

The polaron is very important to understand the working principle of the solar cells. In fact, as will be analyzed in the description of the Braun-Onsager model (see 2.7), the polarons are always present in the process of charge extraction of an organic solar cell.

2.4 Bulk hetero-junction organic solar cells

The structure of a polymeric solar cell (also called bulk hetero-junction solar cell) is shown in Figure 2.8. It has a stacked structure in which a thin film layer containing at least one polymer is sandwiched between two electrodes and two transparent materials (e.g. glass), which allows light transmission and gives mechanical stability to the device. The polymeric layer is made of a mixture of an acceptor material (for example PCBM, see 2.2.4) and a donor polymer (for example P3HT, see 2.2.5). This mixture aims to maximize the contact surface between the two materials, in order to enhance the separation probability of the photo-generated excitons. This is one of the

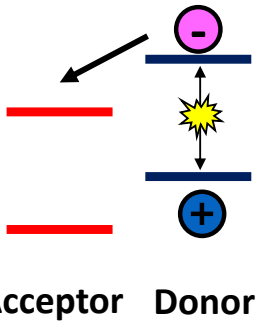

Figure 2.9 Representation of the generation of an exciton in the donor material. When this happens, the electron is suddenly transferred to the acceptor material Of course, the generation may happen even in the acceptor material. In this case, the hole is suddenly transferred to the donor material.

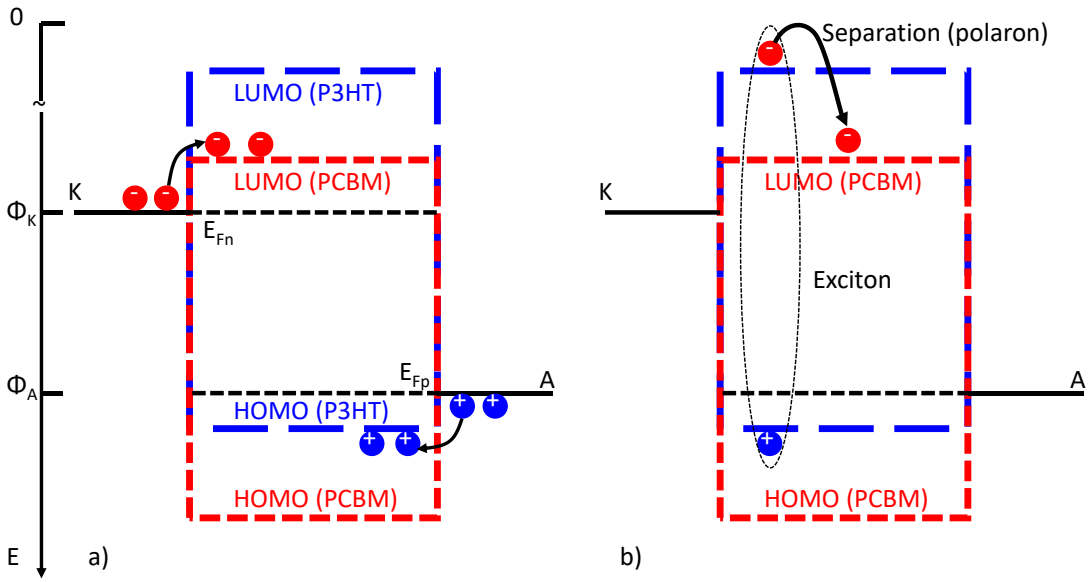

Figure 2.10 Band diagrams of a hetero junction junction solar cell (polymer solar cell). a) Schematic representation of carrier transport inside the respective electronic bands. b) Generation and separation of an exciton.

most important working principle in this type of organic solar cell and in order to discuss it, some clarifications about the representation of the polymeric solar cells band diagram need to be done.

2.4.1 Blend and working principle

In this part, the working principle of a polymeric solar cell will be described. For now, the description will be very simple and intuitive, but it will be further analyzed in the description of the Braun-Onsager model.

During the organic solar cell photogeneration process, the following phases can be identified:

1. Due to the absorption of a photon, an exciton is generated (Figure 2.9, see 2.3.2). The exciton migrates inside the polymers in which has been generated, until it reaches the interface with the other polymer.
2. The electric field separates the electron and the hole of the exciton, eventually generating free charges. When an electron belonging to an excitons generated in the donor material is separated, it passes to the acceptor material, while the respective hole can now be moved inside the donor material. On the contrary, when an exciton generated inside the acceptor material is separated, the hole passes to the donor material and the electron is conducted by the electric field toward the electrode.
3. The electric field moves free electrons and free holes placed in their transport materials towards electrodes, where they can be extracted.

Remarkably, the free charges come from the separation of the excitons. This process is enhanced when the interface between the two polymers inside the blend materials is enhanced: the larger the surface, the more excitons are separated. For this reason, the quality of the polymers blend is very important in the fabrication of a polymeric solar cell. Many efforts are done to maximize the mixture of the polymers. For example, using different functional groups in the polymers fabrication may determine a strong variation in the efficiency of the photovoltaic device. This is the reason why the study of several different polymers is needed to maximize efficiency and reliability.

2.4.2 Band diagram for the polymeric active layer

It would be impossible to represent the blend by means of precise a band diagram, due to the disordered structure of the polymer blend. Nevertheless, it is usefull to find an easy equivalent band diagram representation method, as similar as possible to the conventional band diagrams used for inorganic semiconductors.

First of all, in order to do this, it is necessary to suppose that the blend is homogeneous and that the interface between the two active layer materials spans everywhere in the active layer (i.e. every spot of the blend is a point of interface between the two materials). Furthermore, it is necessary that when electron/hole couple is formed, the electron suddenly passes to LUMO and the hole suddenly passes to HOMO.

This second hypothesis implies that the blend could be treated as a superimposition of both donor and acceptor materials. Thus, the band diagram could be seen as the overlapping of the involved polymers band diagram, as shown in Figure 2.10(a), where the blue diagram is the

band diagram of the donor material and the red diagram is the band diagram of the acceptor material. Due to the hypotheses made, this representation must be valid in every part the film. The carriers may move from a material to another, provided the potential barrier allows it. Of course, this representation does not fulfill the desirable requirement of simplicity. In order to simplify the diagram, the behavior of the charges in the active layer should be analyzed.

The carriers are injected by electrodes: the cathode injects electrons in the LUMO of the acceptor material, the anode injects holes in the HOMO of the donor material. A similar situation occurs when one of the two materials absorbs a photon, generating an exciton. When this happens, the electron is on the LUMO level and the hole is on the HOMO level. As will be better described in the next section, in order to generate free charges the exciton must be separated: the electron and the hole move inside their respective transport materials. For example, if the exciton is generated in the donor material, its electron will be transferred to the LUMO of the acceptor material, where it can be transported (Figure 2.10(b)). The opposite holds true when the exciton is generated in the acceptor material.

Thus, the most important energy levels of the blend are the LUMO of the acceptor material and the HOMO of the donor material, that are the energy levels where the charges are hosted and move (electrons in the acceptor material, hole in the donor material).

This is an important characteristics of the organic solar cells based on an inter-diffused hetero-junction and it can be used to obtain an easy and comprehensible representation of the blend band diagram. In fact, in the light of these last considerations, the junction between the two polymers can be approximated with these two energy levels only. This representation is very similar to the classic band diagrams used in inorganic electronics, but there is a fundamental difference. The HOMO and the LUMO energy levels (that correspond to the valence and conduction bands) belong to different materials, but they are considered to be a unique entity. On the contrary, in the inorganic materials the valence band and the conduction band were part of the same entity and do not belong to different materials.

2.4.3 Typical electrical parameters of a solar cell

In order to describe a classic solar cell, some key parameters are defined. Organic solar cells make no exception, and the most useful parameters are listed in the following and used in this work as important indicators for the study of solar cell quality and health:

- **Short circuit current I_{SC}**: the current given by the solar cell in light condition when the applied voltage is zero. If the short circuit current is divided by the area of the active layer, the short circuit current density J_{SC} is obtained.
- **Open circuit voltage V_{OC}**: the voltage generated by the solar cell when the device is illuminated and no voltage is externally forced.
- **Maximum power point**: the maximum power given by the solar given voltage and current. In fact, $P_{MAX} = I_{MAX} \cdot V_{MAX}$, where the couple (V_{MAX}, I_{MAX}) is called maximum power point.
- **Fill Factor (FF)**: the ratio between maximum power given by the cell and the product $J_{SC}V_{OC}$: $FF = \frac{P_{MAX}}{V_{OC} \cdot J_{SC}}$.
- **Efficiency η**: the ratio between the maximum power and the power given by the incident light: $\eta = \frac{P_{MAX}}{P_S} = \frac{V_{OC} \cdot J_{SC} \cdot FF}{P_S}$

In the last equation the term P_S was used. This parameters identifies the incident light power on the solar cell, and it is generally measured in Sun (where *1Sun = 100mW/cm²*). Of course, in order to compare the efficiency parameters of different solar cells, the same incident light power is needed. Thus, it is assumed that in all the standard measurements made in this work, the light power is 1Sun and the temperature is 25°C (room temperature).

2.5 Inter diffused junction solar cells: state of the art

Some knowledge about organic chemistry and microelectronics were given in the previous sections. In this part, some knowledge about models and about the working principle of the polymeric solar cells will be given.

The current produced by the solar cell when it is illuminated is named Light current (J_{LIGHT} to indicate the light current density, or I_{LIGHT} to indicate the light current[5]).

Light current is given by the summation of two contributes, named dark current (I_{DARK} or J_{DARK}) and photocurrent (I_{PH} or J_{PH}). The first is the current conducted by the organic material when a voltage is applied (as described in 2.3.1), the latter is the current given by only the extracted photogenerated charges:

$$J_{LIGHT} = J_{DARK} + J_{PH} \qquad (2.3)$$

[5] J_{LIGHT} = I_{LIGHT} / Active layer area. In general, the letter *I* will be referred to current absolute value, while *J* will be referred to current density.

Photocurrent is the most characterizing entity for a solar cell. It was mathematically described by the Sokel-Hughes model, described in Section 2.6, and it was extended by the Braun-Onsager (see 2.7). The model developed in this work (more precisely in 0 is a further evolution of these two models, and it describes the photocurrent behavior as a function of the applied voltage as well.

In particular, three models will be described:

- Sokel-Hughes model, which provides an equation that relates the photocurrent produced by a solar cell to the applied voltage.
- Braun-Onsager model, which gives some information about the separation and recombination of the excitons in the active layer. Basing on these information, the model modifies the photocurrent equation given by Sokel and Hughes.
- Limpinsel model, which is based on the first two models, but allows to explain some discrepancies in the theoretical models and the experimental data obtained measuring the photocurrent given by a solar cell.

2.6 Photocurrent I-V measurement: Sokel-Hughes model

Sokel-Hughes model describes the photocurrent as a function of the voltage applied to the device [Sok82]. The model was initially developed for an insulating material, but its results can be also applied to a device made on organic semiconductor. This because, as previously observed, the organic materials share many properties with insulating materials (such as the broad bandgap).

The model takes into consideration the generation mechanisms of excitons and free charges (the same mechanisms analyzed in 2.3 and 2.4). For simplicity, though, it is supposed that the free carriers cannot recombine once generated. As a consequence, the photogenerated excitons can only be separated by means of the electric field, thus every exciton generates an electron/hole couple.

The current due to the charges present inside the film can be expressed as the superposition of some drift and diffusion effects:

$$J_P(x) = \mu_P F q p(x) - \mu_P kT \frac{dp}{dx}$$
$$J_n(x) = \mu_n F q n(x) - \mu_n kT \frac{dn}{dx} \qquad (2.1)$$

In these equations, *n* and *p* refer to electron and hole concentrations in the active layer, respectively. *J* is the current density, *μ* is the carrier mobility, *F* is the electric field inside the active layer (supposed constant), *q* is the elementary charge and $k = 1.38 \cdot 10^{-23} J/K$ is the Boltzmann constant.

The continuity equations for electrons and holes equations (2.1) it can be obtained are:

$$\frac{dJ_P}{dx} = \mu_p F q \frac{dp}{dx} - \mu_p kT \frac{d^2p}{dx^2} = G$$
$$\frac{dJ_n}{dx} = \mu_n F q \frac{dn}{dx} + \mu_n kT \frac{d^2n}{dx^2} = -G \qquad (2.2)$$

Where *G* represents the generation rate of free electrons and holes due to illumination.

Equations (2.2) can be solved by taking as boundary condition the carrier concentrations at the interface of the active layers with electrodes (i.e. in *x=0* and *x=L*, where *L* is the active layer thickness). In fact, n(0)=p(0)=n(L)=p(L)=0. This leads to the following solutions:

$$n(x) = \frac{GL}{\mu_n F}\left[\frac{e^{-\frac{qFx}{kT}} - 1}{e^{-\frac{qFL}{kT}} - 1} - \frac{x}{L}\right]$$
$$p(x) = \frac{GL}{\mu_p F}\left[\frac{e^{-\frac{qFx}{kT}} - 1}{e^{-\frac{qFL}{kT}} - 1} + \frac{x}{L}\right] \qquad (2.3)$$

Using (2.3) into (2.1) it is possible to obtain the current values for electrons and holes as functions of the position inside the active layer. For this reason, it is possible to calculate the current value in any point of the active layer, for example in x=0. Thus:

$$J = J_n(0) + J_P(0) = q\mu_p F p(0) - \mu_p kT p'(0) + q\mu_n F n(0) + \mu_n kT n'(0)$$

Being *n(0)=p(0)=0*,

$$J = -\mu_p kT p'(0) + \mu_n kT n'(0)$$

Where p' and n' indicate the derivatives $\frac{dn}{dx}$ and $\frac{dp}{dx}$:

$$n'(0) = -\frac{qGL}{\mu_n kT}\frac{1}{e^{\frac{qFL}{kT}} - 1} - \frac{G}{\mu_n F}$$
$$p'(0) = -\frac{qGL}{\mu_p kT}\frac{1}{e^{\frac{qFL}{kT}} - 1} + \frac{G}{\mu_p F} \qquad (2.4)$$

Thus, the photocurrent is:

$$J = qGL\left[-\frac{2kT}{qFL} + \frac{e^{\frac{qFL}{kT}}+1}{e^{\frac{qFL}{kT}}-1}\right] \qquad (2.5)$$

Equation (2.5) can be simplified by using $\coth(x) = \frac{1+e^{-2x}}{1-e^{2x}}$. The following expression is obtained:

$$J = qGL\left[-\frac{2kT}{qFL} + \coth\left(\frac{qFL}{2kT}\right)\right]$$

The product $F \cdot L$ is the voltage drop inside the active layer, thus $F \cdot L = V - V_{BI}$, where V_{BI} is the difference between the work functions of the electrodes. Substituting this in the previous equation,

$$J = qGL\left[\coth\left(\frac{V-V_{BI}}{2V_T}\right) - \frac{2V_T}{V-V_{BI}}\right] \qquad (2.6)$$

Where V_T is the thermal potential (*25mV* at room temperature).

2.7 Photocurrent I-V measurement: Braun-Onsager model

Sokel-Hughes model takes into account the free carriers generation rate *G*, which is supposed independent from the position inside the active layer. This might be true in a normal

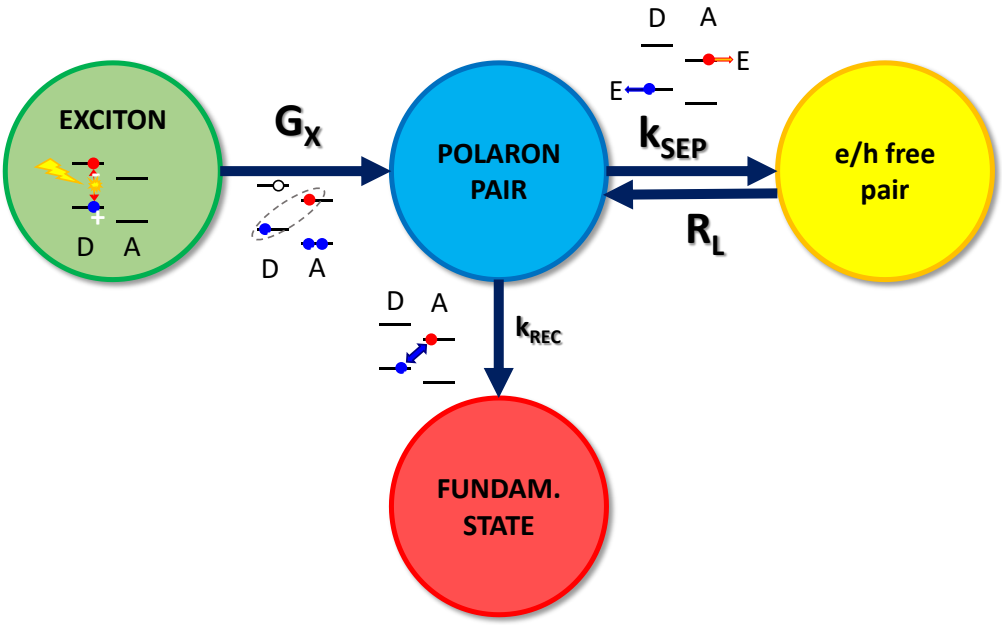

Figure 2.11 Diagram of exciton kinetics inside the active layer.

insulating material, but it is not verified in an organic semiconductor (such as polymeric blends), where the generation of free electron/hole pairs is preceded by the creation and the separation of an exciton. Furthermore, this phenomenon (and in turn the generation rate G) depends on the electric field.

Thus, in order to extend the Sokel Hughes model to organic materials, the generation rate *G* should be related to the electric field. The model proposed by Braun quantifies the separation rate of an exciton taking into account the electric field-dependent parameter P_{SEP}. In more detail, it defines the polaron pairs separation probability (and thus the probability of creating a free electron-hole pair).

The model was developed by Braun in 1984 [Bra84], and it extends the studies made by Onsager in 1938 about the photogenerated charge transport in an insulating material [Ons38]. The changes in the Onsager model became clear when Braun attempted to apply it to solids composed of a mixture of acceptor and donor materials.

When an exciton is generated in proximity of the interface between the acceptor/donor material interface, it might be separated with a high probability. The exciton is now spatially "separated", forming a polaron pair. When the electron and the hole are far enough not to be influenced by electrostatic attraction, they are completely separated, becoming a free electron and a free hole.

Differently from the Onsager theory, in Braun theory the separated carriers could return to the previous form (i.e. the polaron state), as summarized as in Figure 2.11, where the parameters G_X, k_{SEP}, R and k_{REC} express the rate of the corresponding phenomenon and, in particular, have the following meanings:

- G_X expresses the polaron pairs generation rate (or, equivalently, the rate of excitons separation) and is measured in $cm^{-3}s^{-1}$. It depends on the exciton separation velocity k_D and on the exciton concentration inside the active layer. k_D, in turn, depends on the molecule capability of splitting the exciton between an acceptor and a donor molecule
- k_{SEP} is the polaron pairs separation velocity and it is measured in s^{-1}. The dependence on this parameter from the electric field is of fundamental importance, as will be further analyzed later in this section.
- k_{REC} expresses the velocity of polaron pairs recombination to fundamental state. Also this parameter is expressed in s^{-1}. Note that this parameter refers to the

polaron pairs recombination, and not to the exciton recombination (which will not be taken into consideration here, as was done by Braun).

- The parameter R_L expresses the rate of an electron-hole pair to return to its polaron state. Same as G_X, R_L is measured in $cm^{-3}s^{-1}$. According to the Langevin theory, in disordered solids, and in particular in organic semiconductors, bimolecular recombination between an electron and a hole happens only when an electron is captured by the Coulomb radius of the hole (and viceversa). When this happens, the two carriers return to a polaron state. Refer to 2.7.1 and to 4.3.1 for more information.

The following analysis will focus on the relation between the polaron pairs dissociation and the recombination of electrons and holes. In order to do this, the recombination rate and separation rate will be further analyzed.

2.7.1 Langevin bimolecular recombination and k_{SEP} expression

The electron/hole recombination rate R_L was calculated by Langevin. According to his studies, R_L depends on the concentration of both electrons and holes inside a material, and this fact is expressed by the relation $R_L = np\gamma$, where $\gamma = \frac{<\mu>q}{\epsilon_0 \epsilon_R}$ and is called Langevin coefficient. In the last expression $<\mu>$ is the average mobility of the carrier inside the analyzed material, and it depends on both the contribution of electrons and holes, q is the elementary charge, ϵ_R and ϵ_0 are the relative dielectric constant of the material ($\epsilon_R \cong 3$ in organic materials) and the dielectric constant in vacuum ($\epsilon_0 = 8.85 \cdot 10^{-12} \frac{C^2}{Nm^2}$).

k_{SEP} has a more complicated expression, if compared to the expression of R_L. It depends on the electric field and it is given by the product of two expressions:

$$k_{SEP}(F) = k_{SEP0} \cdot B(F) \qquad (2.7)$$

In the last equation, both k_{SEP0} and $B(F)$ have an important meaning, and they will be analyzed in the following.

According to some analysis made before the development of the Braun model found that the ratio k_{SEP0} is given by

$$k_{SEP0} = \gamma \frac{3}{4\pi a^3} e^{-\frac{\Delta E}{kT}} \qquad (2.8)$$

Where a is a constant equal to the average distance between two adjacent molecules inside the material. Generally, in an organic material this value is around 1nm. ΔE is the energy

bond of the excitons, and it correspond to the energy needed by an exciton to promote its electron into the transport band. Its analytical expression is $\Delta E = \frac{q^2}{4\pi\epsilon\epsilon_0 a}$.

Instead, the function *B(F)* expresses the electric field *F* dependence on the polaron pairs separation rate. It depends on the first order Bessel function J_1:

$$B(F) = \frac{J_1\left(2\sqrt{-2|b|}\right)}{2\sqrt{-2|b|}} \qquad (2.9)$$

The parameter b is electric field linear dependent, and its complete expression is:

$$b = \frac{q^3 F}{8\pi\epsilon\epsilon_0 k^2 T^2} = \frac{qF}{8\pi\epsilon\epsilon_0 V_T^2} \qquad (2.10)$$

In this expression, V_T indicated the thermal potential. Figure 2.12 shows Equation (2.9) as a function of a general argument *x*. The function is normalized by its argument, and it shows a minimum when x=0 (*min(B(x))* = 1). For this reason, when the electric field is zero, the dissociation rate k_{SEP} is at its lowest level.

Conversely, when the electric field increases, the Bessel function states that the excitons dissociation rate must increase.

For small values of *b*, (2.9) can be approximated using the following polynomial:

$$B(F) = 1 + b + \frac{b^2}{3} + \frac{b^3}{18} + \cdots \qquad (2.11)$$

Thus, substituting in (2.7),

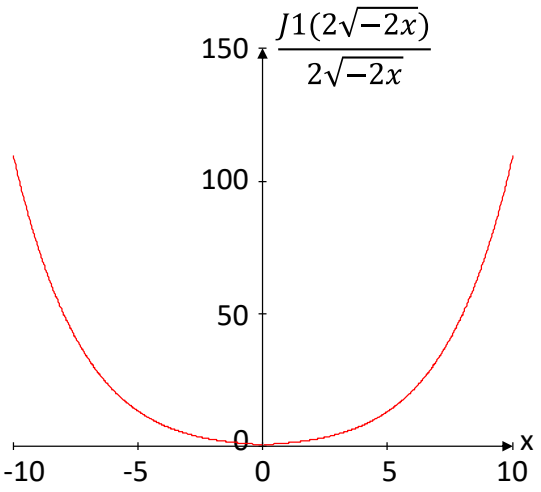

Figure 2.12 Bessel function B(x) normalized by the value of its argument.

$$k_{SEP} \cong \frac{<\mu> q}{\epsilon_0 \epsilon} \frac{3}{4\pi a^3} e^{-\frac{\Delta E}{kT}} \left(1 + b + \frac{b^2}{3} + \frac{b^3}{18} + \cdots\right) \quad (2.12)$$

This equation depends, once again, on the electric field (due to the presence of the variable *b*, which, in turn, depends on the electric field). k_{SEP} is an even function, and this suggests that the polaron separation does not depend on the direction of the electric field, but only on its intensity.

2.7.2 Polaron pairs separation probability P_{SEP}

When the solar cell is illuminated and it is in steady state condition, the number of polaron pairs (generated by the excitons separation process and by the recombination of free electron/hole to a polaron state, as depicted in Figure 2.11) must equal the number of electron/hole pairs separated plus the polaron pairs that recombines to a fundamental state. In other words, naming *X* the polaron pairs concentration inside the active layer, the following relation holds true:

$$G_X + R_L = (k_{SEP} + k_{REC})X$$

From this relation, it can be obtained the expression for X:

$$X = \frac{G_X + R_L}{k_{SEP} + k_{REC}} \quad (2.13)$$

Furthermore, being:

$$G_{np} = k_{SEP} X \quad (2.14)$$

The generation rate of free electrons/holes pairs is defined using (2.14) and (2.13):

$$G_{np} = \frac{k_{SEP}}{k_{SEP} + k_{REC}} (G_X + R_L) = P_{SEP}(G_X + R_L) \quad (2.15)$$

The parameter P_{SEP} is the separation probability introduced by Braun. It is worth to notice that this equation does not contradict the theory proposed by Sokel and Hughes. In fact, supposing the bimolecular recombination excluded (i.e. $k_{REC}=0$) and supposing that a free electron and a free hole cannot return to the polaron pair state (i.e. the Langevin recombination rate $R_L=0$), G_{np} becomes the same parameter used in the Sokel-Hughes model.

In order to include in the photocurrent function the effects described so far, the photocurrent expressions must be corrected by introducing the contribution of $P_{SEP}(E)$ [Alt11].

$$J = qG_X P_{SEP}(F)L\left[\coth\left(\frac{V - V_{BI}}{2V_T}\right) - \frac{2V_T}{V - V_{BI}}\right] \qquad (2.16)$$

2.8 Effects of the charges accumulations close to the electrodes

2.8.1 Band bending in the polymeric solar cell

The band banding diagram associated to the active layer of a solar cell can be obtained solving the equations that describe the electric field and potential.

Figure 2.13 shows the band diagram of the active layer for different polarization of the device. Figure 2.13(a) represent the ideal situation in which there is no contact between the electrodes and the active layer. In this situation, there is no bending in the band diagram.

As it can be easily noticed in Figure 2.13(b), the bands are bent in proximity of the contacts when equilibrium is reached. Of course, this is due to the presence of a charge accumulation given by the difference between the Fermi levels and the work functions of the electrodes. The bulk energy levels are bent linearly, and the bending slope changes with the applied voltage, as in a normal PIN diode [Mul03]. In equilibrium conditions, the charge extraction from electrodes is promoted. In particular, the cathode extracts the electrons in the HOMO band, and the anode extract holes in the LUMO band.

When the applied voltage is negative ($V_{ANODE} < V_{CATHODE}$), the bending condition is very similar to those obtained in equilibrium condition, but the slope of the bands is sharper. If photogenerated carriers are present, they drift towards electrodes where they are completely extracted. If the applied voltage grows, no large variations are observed in the number of extracted carriers, justifying the presence of a constant current (photocurrent I_{PH} becomes negative[6]).

Vice versa, when the applied voltage is positive ($V_{ANODE} > V_{CATHODE}$), the bending is reduced. In Figure 2.13(c), the applied voltage is enough to reach a quasi-flat band condition in which the bands in the bulk of the solar cell are flat. Conversely, the bands close to the electrodes are bent due to charge accumulations. Figure 2.13(d) shows the band diagram when the applied voltage

[6] The photocurrent is supposed positive when electrons flows from the photovoltaic cell bulk region to the cathode (or, equivalently, when holes flows from the bulk region to the anode).

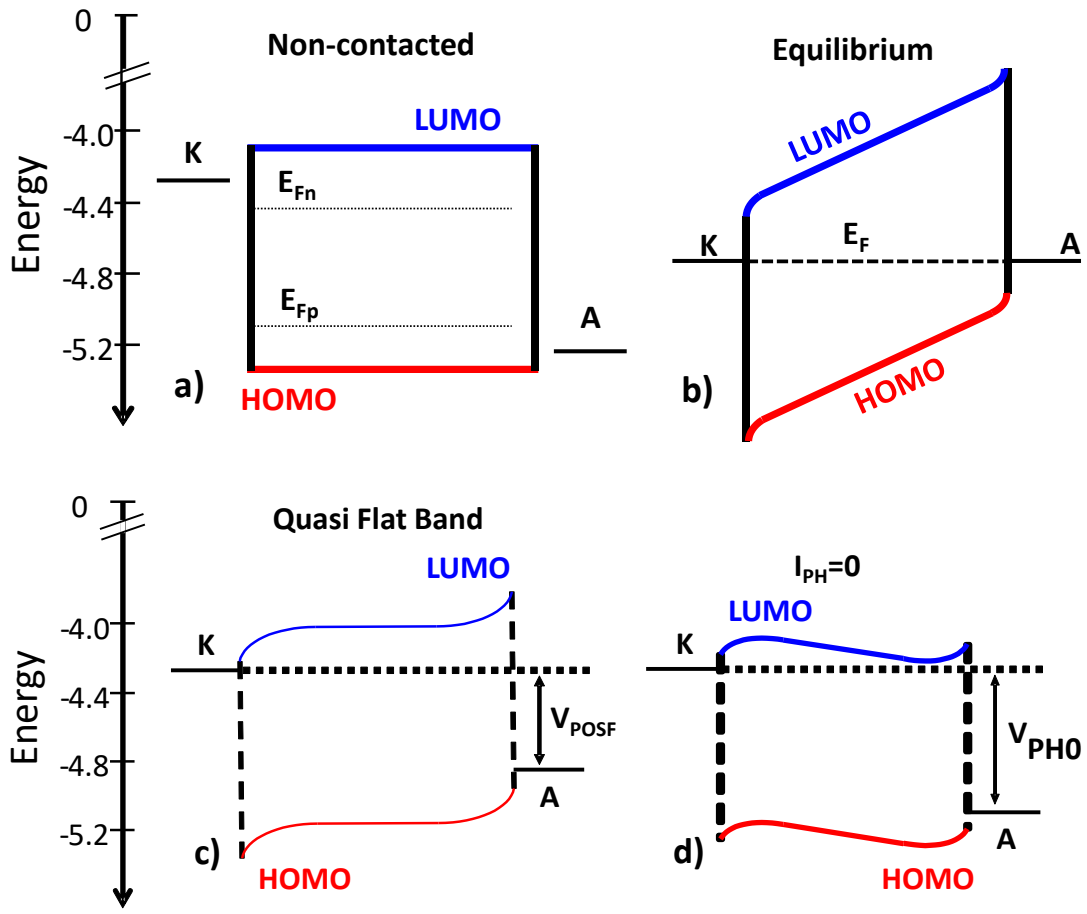

Figure 2.13 Band diagram of an organic solar cell in four different conditions. a) The active layer is not contacted with the electrodes: it is not polarized and its bands are completely flat. The same holds true for electrodes. b) Equilibrium condition in the active layer (zero applied voltage). c) The applied voltage induces a quasi flat band condition in the bulk region (zero field, constant voltage). The regions close to the electrodes are still bent. d) Zero photocurrent condition: the applied voltage is enough to "cancel" the photocurrent produced by the solar cell.

nullifies the photogenerated current ($I_{PH}=0$). This situation will be further discussed later due to its importance in the improvements of the models shown this far.

2.8.2 Limpinsel model

The models developed by Sokel-Hughes and by Braun-Onsager (see 2.6 and 2.7), were further modified by Limpinsel, as presented in [Lim10], and by Ooi et al. [Ooi08a], [Ooi08b].

The main reason that led to this modification is based on some experimental evidence and to their confrontation with the models. In particular:

- According to the models illustrated in 2.6 and 2.7, when the voltage V applied to an organic semiconductor is equal to the built-in potential V_{BI} (i.e. the difference between the work functions of the electrodes), the photocurrent should be zero. This is predicted by the equations that describe the models and by the band diagram, which shows no bending, suggesting that no charges should be extracted

from the device. However, experimental results do not confirm this theory: the extrapolated photocurrent becomes zero when the applied voltage reaches the value V_{PH0}, which depends on the solar cell under test and is not equal to V_{BI}. Remarkably, $V_{PH0} < V_{BI}$.

- The I-V experimental characteristics exhibits a point of optymal symmetry (POS) at a voltage V_{POS}. In the original Sokel-Hughes model, V_{POS} was equal to the voltage V_{BI} and to the voltage where the curve of the photocurrent exhibits an inflection. As will be described in this section, according to Limpinsel, V_{POS} does not correspond to V_{BI} nor to V_{PH0}.

The main result obtained by the studies of Limpinsel regards the photocurrent generated by the solar cell. In fact, according to Limpinsel, the photocurrent is given by the sum of two contributes: the first depends on the voltage (and is given by the Sokel-Hughes analyzed); the second is a constant value (J_{OFFSET}) which translate the photocurrent characteristics to higher values. In order to understand the reason that led to this modification, the cell photocurrent at different polarization values should be analyzed.

Clearly, the band diagram of an ideal MIM structure is not enough accurate to justify the observations made by Limpinsel. Things change if also the charge accumulations described in 2.8.1 are taken into consideration. Considering this case, when the applied voltage is equal to V_{POS}, the bands condition is the same represented in Figure 2.13(c): flat bands in the bulk region, bending in the electrodes regions. The voltage V_{POS} is lower than the built-in voltage and the measured current can be related to the presence of diffusion phenomena. In fact, in the interface regions the electric field is strong enough to separate the polaron pairs generated in close proximity to the electrode. The free electrons and free holes are extracted by the electrodes, generating a region of low carrier concentration. This attracts other charges from the bulk region of the device, arising a diffusion current $J_{OFFSET}=J_{PH}(V_{POS})$.

This result is confirmed by experimental evidences. In fact, the change in the electrode thickness, or in the electrodes material itself, reflects on the growth of the photocurrent as a vertical shift of the photocurrent curve, as reported in Figure 2.14. This has been related to the modifications on the band bendings in the interface regions, which are influenced by the characteristics of the devices [Lim10].

In order to take into account the observations made, the photocurrent equation changes as in the following:

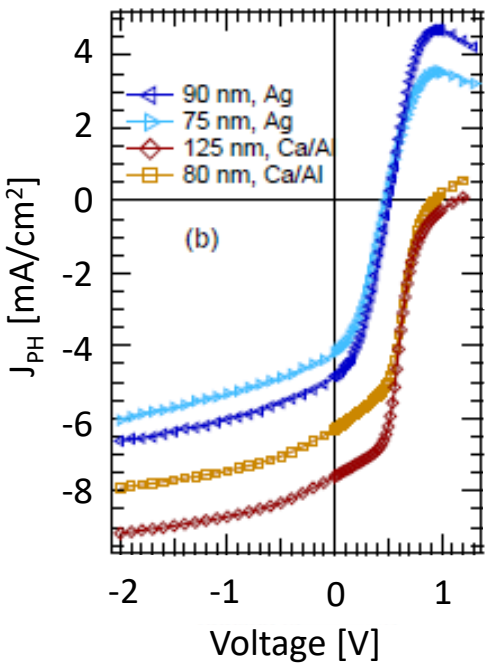

Figure 2.14 Photocurrent curves associated to different electrode types. Changing electrodes material and/or thickness, the photocurrent shifts vertically, due to a change in the charge accumulations in proximity to the electrodes. [Lim10]

$$J = qG_X P_{SEP}(F)L\left[\coth\left(\frac{V - V_{POS}}{2V_T}\right) - \frac{2V_T}{V - V_{POS}}\right] + J_{OFFSET} \qquad (2.17)$$

When the applied voltage approaches V_{POS}, the first term in the sum becomes zero, and $J=J_{OFFSET}$. When V becomes higher than V_{POS}, the energy bands are bent in the opposite sense with respect to what happened in condition of reverse voltage. Now the electric field pushes electrons and holes towards anode and cathode, respectively, giving a positive contribute to the photocurrent.

The photocurrent becomes zero when the applied voltage is equal to V_{PH0}. According to the Sokel-Hughes-Braun theory, this voltage should be equal to the built –in voltage ($|V_{BI}|=|\Phi_A-\Phi_K|$). Taking into consideration the interface band bending, though, this is not correct. As shown in Figure 2.13(d), this voltage only manages to bring the barrier peaks to the same energy level, vanishing the photocurrent. The energy bands in the bulk region are not constant in this condition. In order to reach V_{PH0}, the electrode barrier heights Φ_B must be added to the voltage corresponding to the point of best symmetry (V_{POS}):

$$\Phi_B = V_{PH0} - V_{POS} \qquad (2.18)$$

2.9 References

[Bra84] C. L. Braun, "Electric field assisted dissociation of charge transfer states as a mechanism of photocarrier production", *J. Chem. Phys.*, Vol. 80, n. 9, pp. 4157–4161, 1984, doi:10.1063/1.447243

[Lim10] M. Limpinsel, A. Wagenpfahl, M. Mingebach, C. Deibel, and V. Dyakonov, "Photocurrent in bulk heterojunction solar cells," *Phys. Rev. B*, Vol. 81, n. 8, p. 085203, Feb. 2010. doi: 10.1103/PhysRevB.81.085203

[Mul03] Richard S. Muller, Theodore I. Kamins, "Device Electronics for Integrated Circuits, 3rd Edition", 2003, ISBN: 978-0-471-59398-0.

[Ons38] L. Onsager, "Initial recombination of ions," *Phys. Rev.*, vol. 54, n. 8, pp. 554–557, Oct. 1938. doi: 10.1103/PhysRev.54.554

[Ooi08a] Z. E. Ooi, R. Jin, J. Huang, Y. F. Loo, A. Sellinger, and J. C. deMello, "On the pseudo-symmetric current–voltage response of bulk heterojunction solar cells", Journal of Materials Chemistry, Vol. 18, p.1644-1651, Feb. 2008. doi: 10.1039/B718563D

[Ooi08b] Z. E. Ooi, T. L. Tam, A. sellinger and J. C. deMello, "Field-dependent carrier generation in bulk heterojunction solar cells", *Energy & Environ. Sci.*, Vol. 1, p. 300-309, May 2008. doi: 10.1039/B805435E

[Pet07] Michael C. Petty, "Molecular Electronics: From Principles to Practice", Wiley 2007.

[Sok82] R. Sokel and Hughes "Numerical analysis of transient photoconductivity in insulators", *J. Appl. Phys.*, Vol. 53, n. 11, p. 7414, Nov. 1982. doi: 10.1063/1.330111

Chapter 3 **The photocurrent model**

3.1 Introduction

Despite the models presented in Chapter 2 are good approximations of the behavior of a solar cell, they do not account for solar cells second-order effects, such as non-constant electric field and non-constant free carrier generation rate across the active layer. To give a short summary of the models presented so far, Table 2 shows the photocurrent equations predicted by the models summarized in Chapter 2. In addition, Figure 3.1 shows the simulations of some J_{PH}-V curves. Each curve was generated using the corresponding equation provided by the above mentioned model. For each curve, the most significant points are reported (such as V_{POS}, V_{BI} etc.).

In this chapter it will be presented the new model developed in this work, which includes some effects that that the previous models neglected. In fact, unlikely the previous models, this one also takes into account the band bending at the interfaces induced by the accumulated charge at the electrodes. In other words, it considers the effects of non-constant electric field on the photocurrent behavior. Furthermore, a non-uniform carrier generation rate and the field dependent polaron pairs separation probability will be included.

The model will be also validated in the last part of the chapter, correlating the theoretical and experimental results for fresh and aged devices. In doing so, some problems that were only partially explained by the models presented in Chapter 2 will be clarified. In particular, it will be explained which is the role of the band bending at the interfaces in the offset current, in the J_{PH}-V shape, and in the appearance of multiple inflection points in the J_{PH}-V curve.

Model	Equation
Sokel-Hughes	$J_{PH} = qGL\left[coth\left(\frac{V-V_{BI}}{2V_T}\right) - \frac{2V_T}{V-V_{BI}}\right]$
Braun-Onsager	$J_{PH} = P_{SEP} \cdot qGL\left[coth\left(\frac{V-V_{BI}}{2V_T}\right) - \frac{2V_T}{V-V_{BI}}\right]$
Limpinsel	$J_{PH} = P_{SEP}qGL\left[coth\left(\frac{V-V_{POS}}{2V_T}\right) - \frac{2V_T}{V-V_{POS}}\right] + J_{OFFSET}$

Table 2 Equations described by the models presented in Chapter 2. In the first column, it is also provided a reference where to find further details about the model.
The models refer to [Sok82], [Alt11], [Lim10], [Bra84].

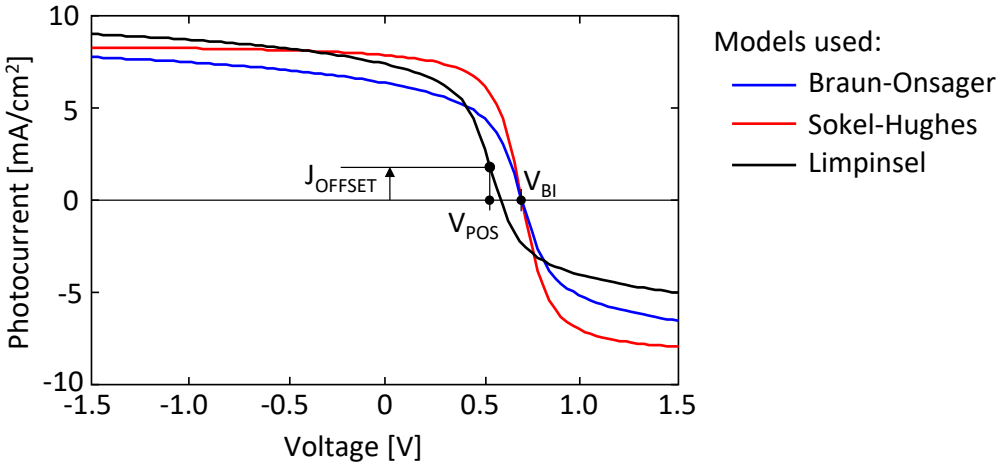

Figure 3.1 Comparison between the photocurrents predicted by Sokel-Hughes model [Sok82]; The Limpinsel model [Lim10]; Braun-Onsager model [Bra84], [Alt11].

3.2 Constant charge distribution model description

In order to develop an analytic photocurrent model capable of taking into account the factors which the Sokel-Hughes and Braun-Onsager model did not take into account, it is necessary to make some assumptions and approximations of different nature. These approximations, listed above, will allow to develop a model which will be simple and clear, but still accurate.

1. As described in 2.8, the difference between the Fermi levels in the active layer and the electrodes work functions leads to an accumulation of negative charges at the cathode interface. The same holds true at the anode interface, where positive charges are accumulated. The charge distributions extend into the active layer for some tens of nanometers, as verified by some drift diffusion numerical simulations (see the black bold solid lines in Figure 3.2(a)). The charge

Symbol	Meaning	Values assumed in this model
μ_n	Electron mobility	$0.006 cm^2V^{-1}s^{-1}$
μ_p	Holes mobility	$0.01\ cm^2V^{-1}s^{-1}$
V_T	Thermal potential	25mV (at room temperature)
k	Boltzmann constant	$1.38 \cdot 10^{-23} JK^{-1}$
T	Absolute temperature	300K
a	Average molecular distance	1nm
ΔE	Exciton binding energy	$q/(4\pi\varepsilon a)$=0.48eV
ε	Dielectric permittivity	$3\varepsilon_0 = 2.65 \cdot 10^{-13} F/cm$
λ	Absorption coefficient	$8.33 \cdot 10^4 cm^{-1}$
L	Active layer thickness	300nm or 315nm

Table 3 Notations and constants used for the photocurrent model developed in this chapter.

accumulations produce a voltage drop at the interfaces, which makes the electric field non-constant across the layer.

In Figure 3.2 the constant charge at the interface are described by both the depths of the accumulation (W_n and W_p, for electrons and holes, respectively) and by the charge density value (N_n and N_p). The charge accumulations give rise to a potential barrier Φ_B which can be calculated with the following equations:

$$\Phi_{Bn} = \frac{qN_nW_n^2}{2\epsilon} \quad \Phi_{Bp} = \frac{qN_pW_p^2}{2\epsilon}$$

2. The charge distribution is considered independent on the applied bias, at least at reverse or moderate forward bias, i.e. when carrier injection is negligible.
3. Similarly, the charge distribution is assumed independent on light conditions. This approximation holds true if the concentration of photogenerated carrier is much small than compared to the accumulated charge density at the interface.
4. The photogeneration rate $G(x)$ was considered exponentially decreasing within the active layer. Its spatial distribution is described by the following equation:

$$G(x) = G_0 e^{-\lambda x} \qquad (3.1)$$

Where λ>0 is the absorption coefficient. In all the simulations it is assumed that the cell is illuminated from the cathode side (x=0). Since the absorption length of PCBM:P3HT blend depends on the incident light wavelength, λ was set to 1/120nm. This value is close to the peak wavelength within the absorption spectrum, as reported in some works in literature [Kim06][Lee10].

5. Finally, the bimolecular recombination was neglected, in agreement with what reported in [Ces15] and [Mar08]. In fact, it was verified that in the polymeric solar cells there is a perfect linear dependence between the short circuit current and

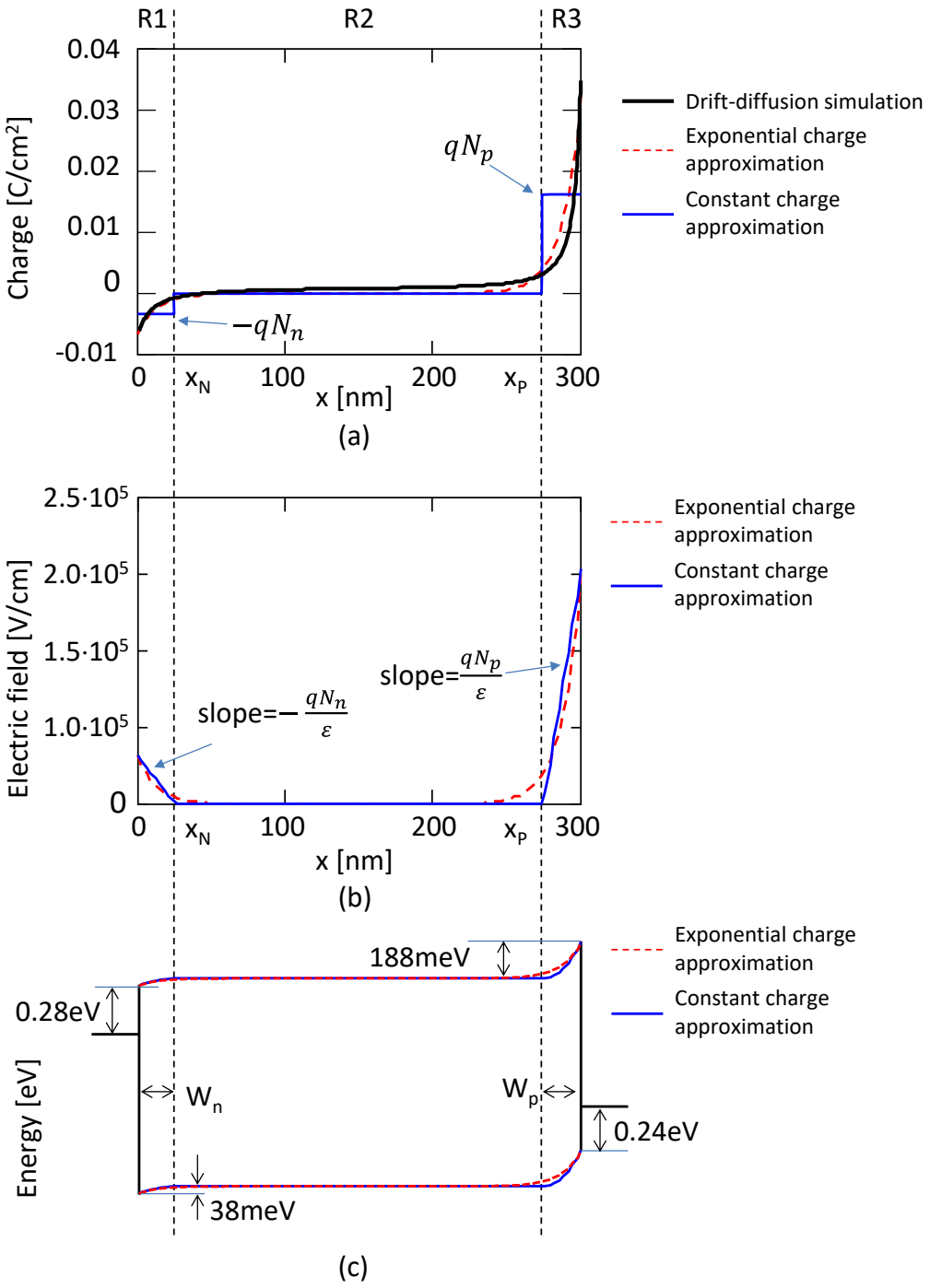

Figure 3.2 a) Simulation of the charge carrier accumulation. Solid blue lines represent the constant charge approximation at the interfaces, the red dashed curve is the exponential charge approximation, the bold black solid line is the charge profile predicted by a self-consistent drift diffusion simulation. The cathode is at x=0, and the anode is at x=L=300nm (in this case). b) Electric field in the case of constant charge approximation (blue solid line) and exponential approximation (red dotted line). c) Band diagram in the case of constant charge approximation (blue solid line) and exponential approximation (red dotted line). The values of the band bending are those obtained with the parameters values used to fit the curves in Figure 3.3(a).

the incident light power. This is a signature of negligible bimolecular recombination, as demonstrated in [Mar08].

In order to calculate the real shape of the charge distribution inside the active layer, a drift-diffusion simulation is needed. Such a simulation might be very complex and potentially very time-consuming if used on a huge number of measured devices. Thus, for the sake of simplicity, in this work two different possible shapes are used for the accumulated charge distribution at the interfaces with the electrodes: constant and exponential. Both of these options are shown in Figure 3.2(a) (blue line for the constant charge distribution, red dashed line for the exponential charge distribution). In addition, in the same figure a drift diffusion simulation for the charge accumulation distribution is shown (black, solid line).

It has been verified that the exponential distribution is close to the drift diffusion simulations results, but the transport equations are more difficult to be solved analytically. On the contrary, the constant charge distribution is easier to handle, and allows to simplify the development of the analytical model. Incidentally, the band bending predicted by the exponential charge distribution and constant charge distribution are very close to each other (see Figure 3.2(c)). For these reasons, the following analysis will be developed using the constant charge accumulation at the interface. The comparison between the constant and exponential distribution is postponed to the last part of this chapter (see 3.5).

The constant charge approximation allows to divide the cell into three regions (in Figure 3.2 they are separated by a dashed line):

R1) A negative charge accumulation region at the cathode ($x<W_n$);

R2) A central quasi-neutral region ($W_n < x < L-W_P$)

R3) A positive charge accumulation region at the anode ($x>L-W_P$).

Remarkably, W_n and N_n are the values of band bending extensions and constant charge concentration for negative charges. Correspondingly, W_p and N_p are the band bending values due to positive charge accumulations.

The charge accumulation in R1 and R3 generate an electric field (Figure 3.2(b)) and, in turn, a voltage drop responsible for the band bending at the contacts (Figure 3.2(c)). The electric field is linear, and the band bending is parabolic. In the quasi-neutral region R2 the electric field is constant. In Table 5 are shown the equations describing the charge distributions, the electric field and the voltage as functions of the position inside the active layer.

The model is obtained starting from the continuity equations for electrons and holes:

$$-G(x)P_{SEP}(E) = \mu_n \frac{\partial E}{\partial x} n + \mu_n E \frac{\partial n}{\partial x} + V_T \mu_n \frac{\partial^2 n}{\partial x^2}$$
$$G(x)P_{SEP}(E) = \mu_p \frac{\partial E}{\partial x} p + \mu_p E \frac{\partial p}{\partial x} - V_T \mu_p \frac{\partial^2 p}{\partial x^2} \qquad (3.2)$$

Where *n* and *p* are the photogenerated electron and hole concentrations inside the blend, respectively. See Table 3 for other constant values and notations. Noticeably, in contrast with previous analytical models approach [Sok82][Alt11], here it is considered a spatially variable electric field (as in Figure 3.2, where the electric field is linear in proximity of the electrodes).

The exciton separation probability (P_{SEP}) is accounted for using the Braun-Onsager model already described in 2.7, and reported in literature in [Bra84]. The coefficient P_{SEP} is:

$$P_{SEP}(F) = \frac{k_{SEP}(F)}{k_{SEP}(F) + k_{REC}} \qquad (3.3)$$

In this equation k_{REC} is the polaron pairs recombination rate and k_{SEP} is the polaron pairs separation rate, which is field dependent. In 2.7 it is also reported the extended expression for k_{SEP}, which can be expressed by means of a non-linear function.

At this point, it is worth to note that the electric field is not constant across the active layer. In particular, *F(x)* is constant inside the region *R2*, but it linearly increases in regions *R1* and *R3* (see Figure 3.2(b)). Hence, being the separation probability related to the electric field *F*, it features a minimum in the bulk of the active layer (region *R2*) and it increases close to the electrodes (regions *R1* and *R3*).

It is now possible to make another approximation. It is about the value of $P_{SEP}(E)$, which from now on is assumed constant all over the active layer. Its value is that calculated in *R2*. This approximation is reasonable because R2 represents the majority of the blend volume. Even though this might introduce a slight underestimation of the photocurrent, it strongly simplifies the analytical solution of the model equations, at least under the constant charge distribution approximation.

Solving (3.2) for *n(x)* and *p(x)* in each region, the electron and hole concentrations equations can be written:

$$n(x) = \begin{cases} A_{R1} n1_{R1}(x) + B_{R1} n2_{R1}(x) + n0_{R1}(x) & in\ R1 \\ A_{R2} n1_{R2}(x) + B_{R2} n2_{R2}(x) + n0_{R2}(x) & in\ R2 \\ A_{R3} n1_{R3}(x) + B_{R3} n2_{R3}(x) + n0_{R3}(x) & in\ R3 \end{cases} \qquad (3.4)$$

Symbol	Value for electron continuity equation	Value for hole continuity equation
a_1	$-qN_n/\varepsilon V_T$	$qN_n/\varepsilon V_T$
a_2	E_0/V_T	$-E_0/V_T$
a_3	$qN_p/\varepsilon V_T$	$-qN_p/\varepsilon V_T$
x_1	$W_n + \frac{\varepsilon E_0}{qN_n}$	
x_3	$L_{W_P} - \frac{\varepsilon E_0}{qN_p}$	

Table 4 Notations and coefficients used in the homogeneous and particular solutions of equation (3.2).

$$p(x) = \begin{cases} C_{R1}p1_{R1}(x) + D_{R1}p2_{R1}(x) + p0_{R1}(x) & in\ R1 \\ C_{R2}p1_{R2}(x) + D_{R2}p2_{R2}(x) + p0_{R2}(x) & in\ R2 \\ C_{R3}p1_{R3}(x) + D_{R3}p2_{R3}(x) + p0_{R3}(x) & in\ R3 \end{cases}$$

In these equations: $n1_{Ri}$ and $n2_{Ri}$ (where i=1,2,3) are solutions for the homogeneous equations for electron concentrations, $p1_{Ri}$ and $p2_{Ri}$ are solutions for the homogeneous equations for holes concentrations, and n_{0i} and p_{0i} are particular solutions in the region R_i for electrons and holes respectively. In the following, the expressions of the homogenous and particular solutions used in equations (3.4) will be given.

a) Electron and holes concentration

In region R1 and R3 the homogeneous solutions are:

$$n1_{R1}(x) = p1_{R1}(x) = e^{-\frac{a_1(x-x_1)^2}{2}}$$

$$n2_{R1}(x) = p2_{R1}(x) = \sqrt{-\frac{\pi}{2a_1}}e^{-\frac{a_1(x-x_1)^2}{2}}\operatorname{erf}\left(x\sqrt{-\frac{a_1}{2}}\right) \qquad (3.5)$$

$$n1_{R3}(x) = p1_{R3}(x) = e^{-\frac{a_3(x-x_3)^2}{2}}$$

$$n2_{R3}(x) = p2_{R3}(x) = \sqrt{-\frac{\pi}{2a_3}}e^{-\frac{a_3(x-x_3)^2}{2}}\operatorname{erf}\left(x\sqrt{-\frac{a_3}{2}}\right)$$

Where a_1 and a_3 are constants defined in Table 4 (second column for electrons and third column for holes), x_1 and x_3 are constants shown in Table 4 as well.

In region R2, where the electric field is constant, the homogeneous solutions become:

$$n1_{R2}(x) = p1_{R2}(x) = 1$$
$$n2_{R2}(x) = p2_{R2}(x) = e^{-a_2 x} \quad (3.6)$$

Where a_2 is a constant defined in Table 4 as well.

The particular solutions in the three regions, are expressed in (3.7):

$$n0_{R1} = -\frac{G_0}{V_T \mu_n}\frac{1}{\lambda}\sqrt{-\frac{\pi}{2a_1}}e^{\frac{\lambda^2 - a_1^2(x-x_1)^2}{2a_1}}\operatorname{erf}\left(\frac{\lambda - a_1(x-x_1)}{\sqrt{-2a_1}}\right)$$
$$p0_{R1} = -\frac{G_0}{V_T \mu_p}\frac{1}{\lambda}\sqrt{-\frac{\pi}{2a_1}}e^{\frac{\lambda^2 - a_1^2(x-x_1)^2}{2a_1}}\operatorname{erf}\left(\frac{\lambda - a_1(x-x_1)}{\sqrt{-2a_1}}\right)$$

$$n0_{R2} = \frac{G_0}{V_T \mu_n}\frac{1}{\lambda^2 - a_2\lambda}e^{-\lambda x} \quad (3.7)$$
$$p0_{R2} = \frac{G_0}{V_T \mu_n}\frac{1}{\lambda^2 - a_2\lambda}e^{-\lambda x}$$

$$n0_{R3} = -\frac{G_0}{V_T \mu_n}\frac{1}{\lambda}\sqrt{-\frac{\pi}{2a_3}}e^{\frac{\lambda^2 - a_3^2(x-x_3)^2}{2a_3}}\operatorname{erf}\left(\frac{\lambda - a_3(x-x_3)}{\sqrt{-2a_3}}\right)$$
$$p0_{R3} = -\frac{G_0}{V_T \mu_p}\frac{1}{\lambda}\sqrt{-\frac{\pi}{2a_3}}e^{\frac{\lambda^2 - a_3^2(x-x_3)^2}{2a_3}}\operatorname{erf}\left(\frac{\lambda - a_3(x-x_3)}{\sqrt{-2a_3}}\right)$$

b) Coefficients

A_{Ri}, B_{Ri}, C_{Ri}, and D_{Ri} of (3.4) are integration constants determined using the boundary conditions listed in the next lines:

- The electron and hole concentration continuity in the point x_N and x_P. These points separate region R1 from R2 and R2 from R3, respectively (see Figure 3.2).
- The electron and hole current continuity in the points x_N and x_P.
- The zero carrier concentration at the electrodes, i.e. n(0) = p(0) = 0 at the cathode and n(L) = p(L) = 0 at the anode.

3.3 Model validation and Discussion

3.3.1 Model validation using experimental data of a stressed cell

The model was validated using P3HT:PCBM cells with an active layer of 315nm and an area of 1 cm^2. The cells were fabricated at DTU (Roskilde, Dk) and were assembled in roll-to-roll compatible process with a mini-roll coater [Car13]. The front electrode (Flextrode) is composed of

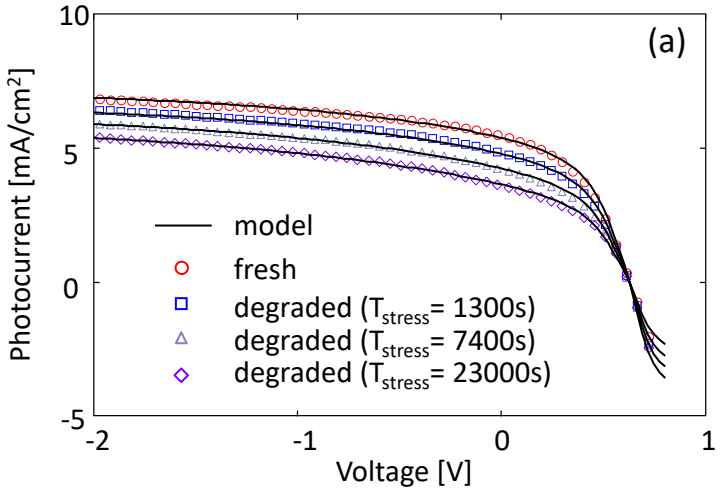

Fitting parameter	Values			
	Fresh	T_{STRESS}=1300s	T_{STRESS}=7400s	T_{STRESS}=23000s
V_{BI}	0.78 V	0.78 V	0.78 V	0.78 V
W_n=W_p	25 nm	25 nm	25 nm	25 nm
N_n	$2{\cdot}10^{16}cm^{-3}$	$2{\cdot}10^{16}cm^{-3}$	$2{\cdot}10^{16}cm^{-3}$	$2{\cdot}10^{16}cm^{-3}$
N_p	$10^{17}cm^{-3}$	$10^{17}cm^{-3}$	$10^{17}cm^{-3}$	$10^{17}cm^{-3}$
G_0	$4.2{\cdot}10^{21}cm^{-3}s^{-1}$	$3.9{\cdot}10^{21}cm^{-3}s^{-1}$	$3.7{\cdot}10^{21}cm^{-3}s^{-1}$	$3.45{\cdot}10^{21}cm^{-3}s^{-1}$
k_{REC}	$5{\cdot}10^{3}s^{-1}$	$6{\cdot}10^{3}s^{-1}$	$7{,}75{\cdot}10^{3}s^{-1}$	$10{\cdot}10^{3}s^{-1}$
k_{SEP}	$10^{4}s^{-1}$	$10^{4}s^{-1}$	$10^{4}s^{-1}$	$10^{4}s^{-1}$
	Band bending derived from parameters above			
Cathode	38 meV	38 meV	38 meV	38 meV
Anode	188 meV	188 meV	188 meV	188 meV

(b)

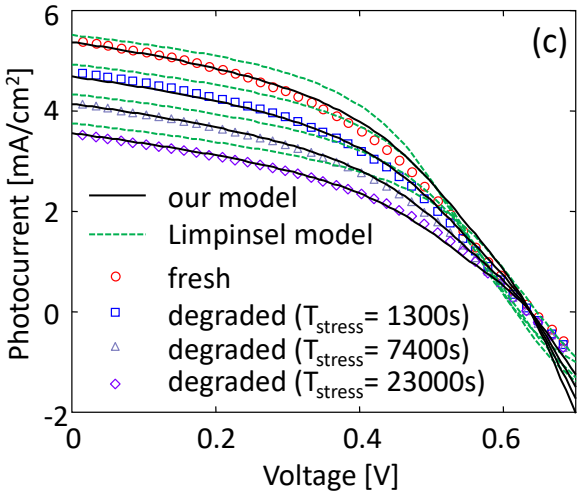

Figure 3.3) Comparison between experimental data and this model of fresh and stressed cells. b) Model parameter values used to fit the experimental data in Fig. 3a. c) Comparison between this model and the model proposed in [Lim10] in the range between 0V and 0.6V. The better fit of the proposed model obtained thanks to the analytical approach accounting for the band bending at the interface is highlighted.

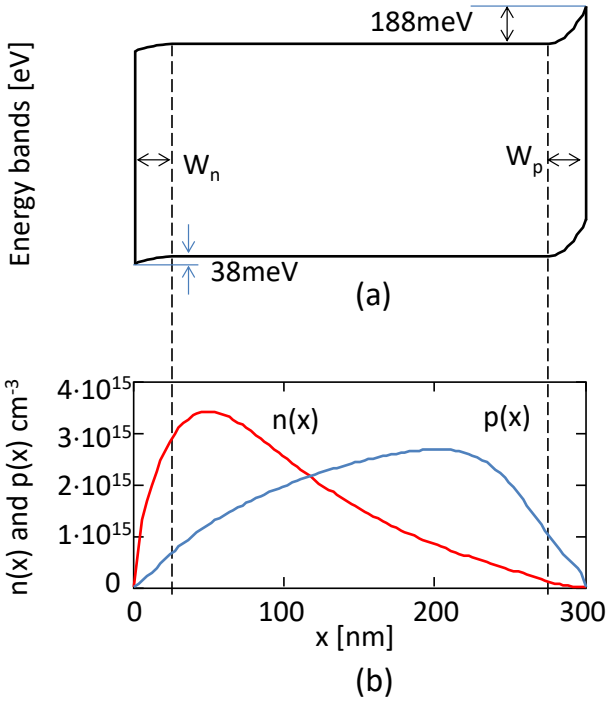

Figure 3.4 a) Energy bands in quasi-flat band conditions. The value of the band bending at the interface is highlighted. b) Concentrations of the photogenerated carriers in the same conditions of Figure 3.3(c).

an Ag grid, PEDOT:PSS and ZnO. The back electrode, consisting of PEDOT:PSS, and an Ag grid enclose the blend of P3HT:PCBM.

Incidentally, for the correct photocurrent estimation, the experimental data needed to be adjusted considering the parasitic series resistance of the active layer, which had the effect to reduce the photocurrent. Using impedance spectroscopy measurement technique, it was calculated that the bulk resistance is 10Ω. The value is in agreement with the values by other works in literature (for example [Lim10]). The measurements were done by means of thermally controlled sample holder at the temperature T=300K.

In all the measurement, the cell was illuminated using a white LED illuminator. The LED intensity was calibrated to reach a cell illumination level of 1Sun. See Refs. [Riz16a] and [Ces15] for further details.

In Figure 3.3(a) are shown the photocurrent experimental data extracted from P3HT:PCBM cells during constant current stress degradation. The stressing current was 70mA/cm^2. The data has been taken from a previous work, reported in Ref. [Riz16a]. The interested reader may refer to that work for more details about the experimental procedures and results. In the photocurrent plot it can be found the photocurrent data produced by the fresh

device (i.e. before the beginning of the degradation) and the values produced by the cell during some degradation steps.

In the same figure, superimposed to the experimental values (dotted lines), are shown the photocurrent values predicted by the model (black solid lines). It is clear that the model (when the correct fitting parameters are used) excellently fits the experimental data in both fresh and degraded cells (symbols). The values of the fitting parameters are shown in Figure 3.3(b), and they mainly describe the charge characteristics inside the active layer.

A correct fit of the experimental data allows to understand which parameters are affected by the stress procedure. In the case examined in this Chapter, it can be inferred that the degradation only changes the generation rate G (which decreases from $4.2 \cdot 10^{21} cm^{-3} s^{-1}$ to $3.45 \cdot 10^{21} cm^{-3} s^{-1}$) and the recombination rate k_{REC} (which increases from $4 \cdot 10^{3} s^{-1}$ to $8 \cdot 10^{3} s^{-1}$). More information about the extracted parameters can be found in Figure 3.3(b).

3.3.2 Comparison with Limpinsel model

A representation of the simulated band bending in quasi-flat band condition (i.e. when the electric field is zero in the bulk of active layer) is shown in Figure 3.4(a). The corresponding simulation for photogenerated electron and hole concentrations in quasi-flat band conditions is shown in Figure 3.4(b). It is worth to be noticed that the distributions predicted by the model shows asymmetrical electron and hole distributions with respect to the center of the active layer. This is the main responsible for the presence of the additional diffusion current J_{OFFSET}, which is

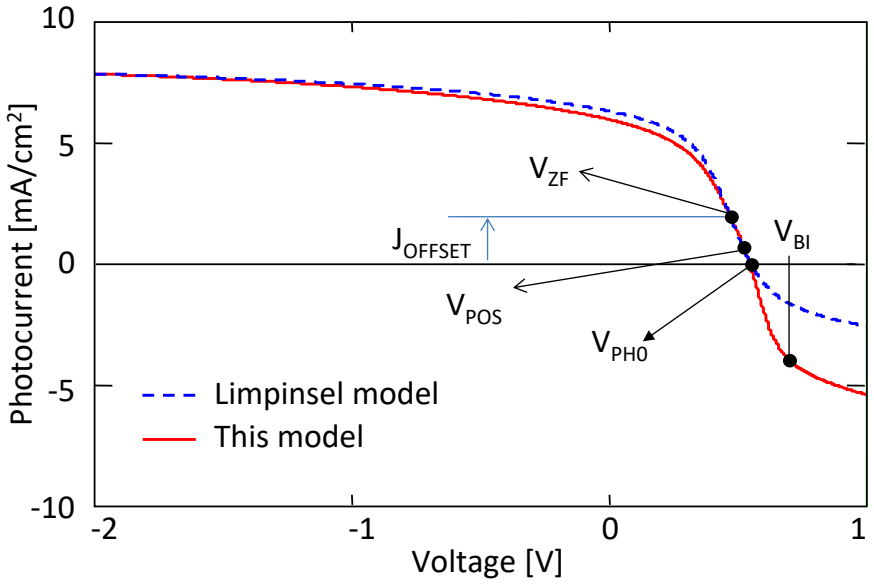

Figure 3.5 Output of the photocurrent model (red solid line) compared to Limpinsel model (blue dotted line). The plot shows the quasi-flat band condition voltage (V_{ZF}), the point of best symmetry (V_{POS}), the built-in potential (V_{BI}) and the offset current $J_{OFFSET}=J_{PH}(V_{ZF})$ referred to this model.

present in quasi-flat band condition (in agreement with what was only qualitatively predicted by Limpinsel [Lim10]).

Incidentally, from Figure 3.4(b) it can be yielded that photogenerated electron concentration is on the order of $10^{15}\ cm^{-3}$ at the cathode, i.e. one order of magnitude smaller than the fixed electron charge ($N_n = 2 \cdot 10^{16} cm^{-3}$ in this case). Similarly, at the anode, the photogenerated hole concentration is two orders of magnitude smaller than the fixed charge ($N_p = 10^{17} cm^{-3}$ in this case).

Figure 3.5 shows the plot of one output of the constant charge distribution model (solid red line). The following points are marked:

1. The point of optimal symmetry of the simulated photocurrent curve (corresponding to the voltage V_{POS}), defined as in [Lim10];
2. The Built-In voltage V_{BI} (which is known because it depends from the simulation parameters);
3. V_{ZF} corresponding to the quasi-flat band condition, i.e. the voltage required to achieve zero-field in R2. Remarkably, this parameter is calculated analytically (and it does not correspond to the point of optimal symmetry, as V_{POS}).

In the same plot, it is also shown a comparison with the photocurrent predicted by the Limpinsel model (dotted line). The two curves are plotted in a way that guarantees their best overlapping, thus the generation rate is tuned in order to achieve the best overlapping between the two models in the region from -2V to 0.6V. The curve of the Limpinsel model is simulated using V_{ZF} as the point of best symmetry.

Comparing the two curves in Figure 3.5, it is easy to notice that the voltage V_{POS} ais not the same as V_{ZF}, in contrast to what was predicted by Limpinsel model. In particular, $V_{ZF} < V_{POS}$. In other words, the point of optimal symmetry of the curve is not equal to the voltage at which the bands inside the active layer are flat. This implies that a correct evaluation of the operative voltages that characterize a solar cell cannot be done following that procedure, but needs a more accurate model.

Remarkably, it is possible to demonstrate that the carrier mobility values (μ_n and μ_p) do not affect the photocurrent shape simulated in Figure 3.5. However, the electron and hole mobilities impact on the electron and holes concentrations, respectively: by increasing the mobility, the corresponding carrier concentration decreases. The mobility values can be obtained

by the analysis of the J-V characteristics in dark [Riz16a] and/or other more sophisticated techniques, such as impedance spectroscopy [Riz16b].

3.4 Effects of the fitting parameters on the modeled photocurrent

In this Section will be analyzed the variations of the photocurrent shape as a consequence of the variations of one or more simulation parameters. This is a very important tool to understand

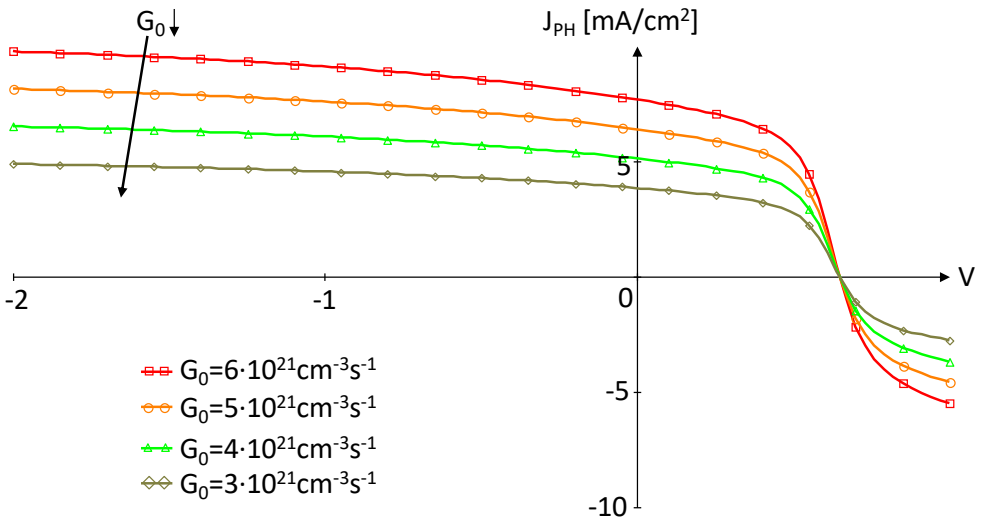

Figure 3.6 Photocurrent curve simulated for different values of the free charges generation parameter G_0. The other parameters used for the simulation are Φ_{Bn}= Φ_{Bp}=100meV, V_{BI}=0.8V, μ_n=0.006cm^2/Vs, μ_p=0.01cm^2/Vs, K_{SEP}=8·10^{3}s^{-1}, k_{REC}=5·10^{3}s^{-1}.

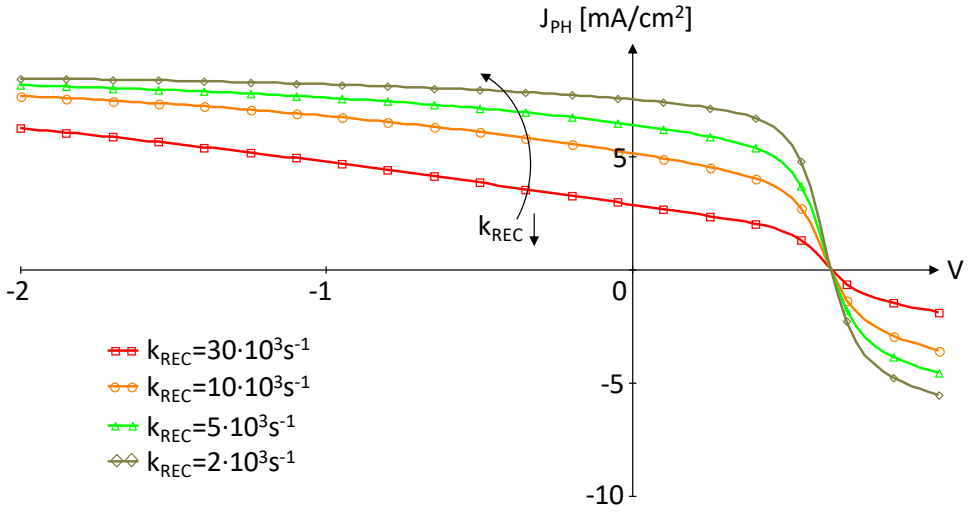

Figure 3.7 Photocurrent curve simulated for different values of the polaron pair recombination rate k_{REC}. The other parameters used for the simulation are ΦBn= ΦBp=100meV, VBI=0.8V, μn=0.006cm2/Vs, μ_p=0.01cm2/Vs, K_{SEP}=8·103s-1, G_0=5·1021cm-3s-1.

immediately which cell parameter is changing as a consequence of degradation. The photocurrent will be analyzed varying G_0, k_{REC}, V_{BI}, ΦBn and ΦBp.

3.4.1 G_0 variation

Figure 3.6 shows the variations of the curve J_{PH}-V as a function of the parameter G_0 in the point of interface with the illuminated electrode. As expected, reducing the generation rate, also the photocurrent reduces. In particular, the photocurrent is vertically shifted almost in every

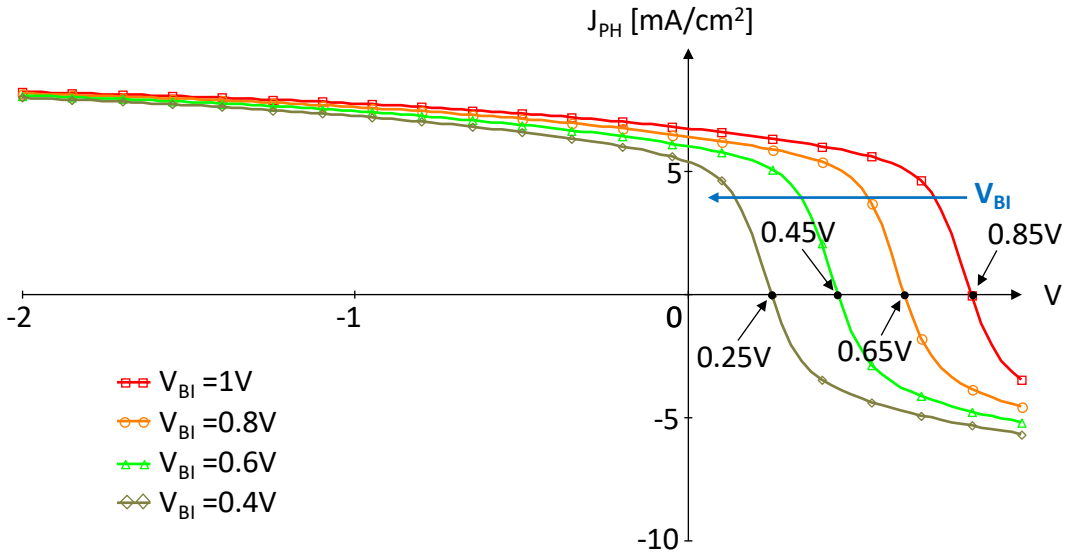

Figure 3.8 Photocurrent curve simulated for different values of the Built-In voltage V_{BI}. The other parameters used for the simulation are $\Phi_{Bn}= \Phi_{Bp}=100meV$, $\mu_n=0.006cm^2/Vs$, $\mu_p=0.01cm^2/Vs$, $K_{SEP}=8\cdot10^3s^{-1}$, $k_{REC}=5\cdot10^3s^{-1}$, $G_0=5\cdot10^{21}cm^{-3}s^{-1}$.

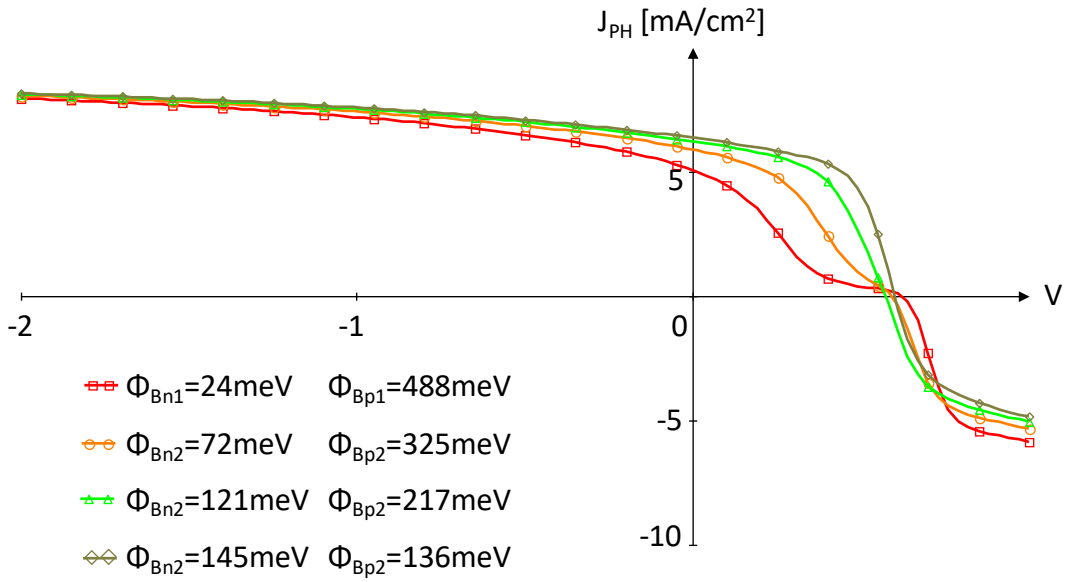

Figure 3.9 Photocurrent curve simulated for different band bending at the interface with electrodes. The other parameters used for the simulation are $W_n=20\cdot10^{-7}cm$, $W_p=30\cdot10^{-7}$, $\mu_n=0.006cm^2/Vs$, $\mu_p=0.01cm^2/Vs$, $V_{BI}=0.8V$, $K_{SEP}=8\cdot10^3s^{-1}$, $k_{REC}=5\cdot10^3s^{-1}$, $G_0=5\cdot10^{21}cm^{-3}s^{-1}$

region. On the contrary, the region where the photocurrent is almost zero is not affected by G_0 variation.

3.4.2 k_{REC} variation

An increase in the recombination parameter k_{REC} should lead to a decrease in the photocurrent. In fact, electron/hole couples recombination is stronger, and this prevents the generation of free electrons and holes that might be extracted from the solar cell. This can be observed in Figure 3.7, where for high k_{REC} the photocurrent values become very low (even at reverse voltages). When the applied voltage increases (both in reverse and direct polarization), the electric field increases. This makes more likely the separation of electrons and holes, generating free charges despite a high value of k_{REC}.

On the contrary, when k_{REC} is low, the photocurrent curve is not heavily altered, and it is almost flat for high electric field (in fact, the measured photocurrent is given by the separation of all the generated polarons, being the recombination rate negligible).

3.4.1 V_{BI} variation

A variation in the built-in voltage corresponds to a rigid translation of the photocurrent curve. When V_{BI} becomes lower, the curve of Figure 3.8 shifts leftward, otherwise it shifts rightward. The voltage at which photocurrent becomes zero (V_{PH0}) is very different from the voltage V_{BI}, as already observed in 3.3.2. In particular, $V_{PH0}<V_{BI}$.

3.4.2 Band bending variation

Figure 3.9 shows the photocurrent variation for different values of the total barrier Φ_B present at the electrodes. In this case, yhe parameter variation is not obtained varying the band bending extension (i.e. W_n and W_p, see Figure 3.2(c)), but only the accumulated charge densities N_n and N_p. The values of the barrier are reported in figure, and they represent only theoretical values, used in order to highlight the variations in the photocurrent.

The first curve (associated to $\Phi B_n=24meV$ and $\Phi B_p=488meV$) is associated to the biggest difference between the two barriers height, while the fourth curve is associated to an almost complete symmetry between the two barriers (Φ_{Bn}=145meV and Φ_{Bp}=136meV).

The main difference that emerges from the comparison of the simulated curves is on the inflections that appear. This is highlighted by the plot in Figure 3.10, where the derivative of the photocurrent $\frac{\partial J_{PH}}{\partial V}$ is plotted as a function of the voltage. In this plot each maximum is associated to an inflection in the photocurrent curve.

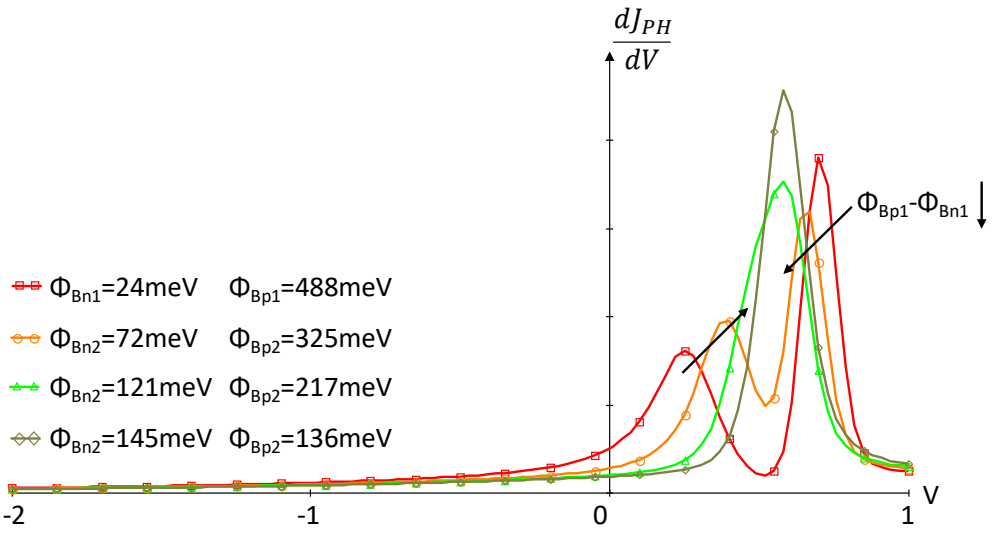

Figure 3.10 Photocurrent derivative $\frac{\partial J_{PH}}{\partial V}$ as a function of the applied voltage. The maxima are associated to the inflections in the photocurrent.

When the two barriers are similar, only one inflection is observed, and the inflection point correspond to the point of optimal symmetry in the photocurrent characteristics. On the contrary, when the difference between ΦB_n *and* ΦB_p becomes high, the inflection splits into two inflections, as in the first curve of Figure 3.9. Equivalently, the peaks in the derivative tend to split and to move away when the barriers are very different. They become a unique peak when ΦB_n is similar to ΦB_p.

This behavior can be explained using the model. Referring to Figure 3.2(c), the band bending at the cathode enhances the electron extraction due to the high electric field, but it acts as a small potential barrier against the hole extraction. Of course, the opposite occurs at the anode contact. This may lead to a strong difference in the contribution of positive and negative charges to the extracted photocurrent (which can be seen as the sum of positive and negative charges), which brings to the separation of the inflections in the photocurrent shape. When the two barriers are similar (or identical), there is no difference in the positive and negative charges contribution to the photocurrent. Thus, the photocurrent shape exhibits only one main inflections, as observed by Sokel and Hughes.

The main advantage in using this model is that is allows to assess the modifications which may occur at the interface due to cell ageing and degradation in general. In fact, the model can detect any variation of the barrier heights in proximity of the electrodes, due to degradation in general (Some examples may be oxidation and other chemical reactions between the contacts and contaminants, either process-induced or penetrated inside the encapsulation during normal operations). In other words, one can take advantage of the model and perform a reliability assessment by means of only electrical measurement.

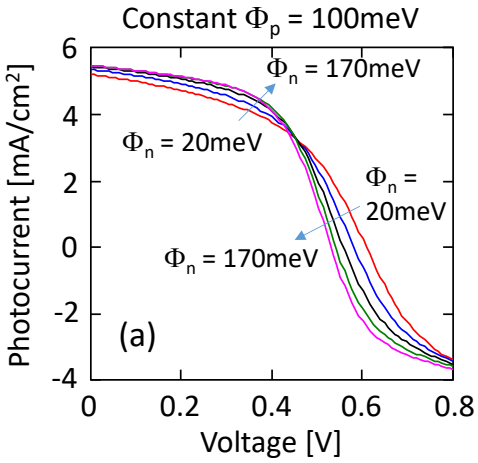

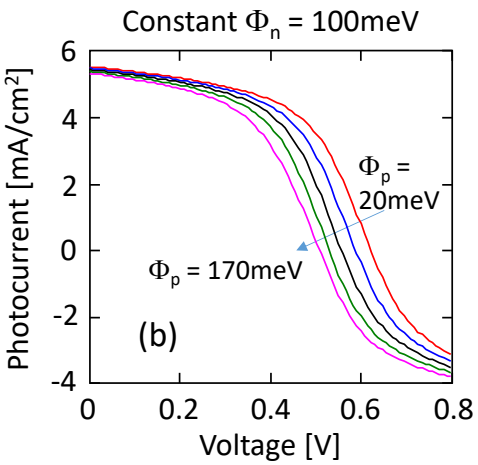

N_n(cm^{-3})	N_p(cm^{-3})	Φ_n(eV)	Φ_p(eV)
$1\cdot10^{16}$	$5\cdot10^{16}$	0.02	0.1
$3\cdot10^{16}$	$5\cdot10^{16}$	0.055	0.1
$5\cdot10^{16}$	$5\cdot10^{16}$	0.1	0.1
$7\cdot10^{16}$	$5\cdot10^{16}$	0.13	0.1
$9\cdot10^{16}$	$5\cdot10^{16}$	0.17	0.1

N_n(cm^{-3})	N_p(cm^{-3})	Φ_n(eV)	Φ_p(eV)
$5\cdot10^{16}$	$1\cdot10^{16}$	0.1	0.02
$5\cdot10^{16}$	$3\cdot10^{16}$	0.1	0.055
$5\cdot10^{16}$	$5\cdot10^{16}$	0.1	0.1
$5\cdot10^{16}$	$7\cdot10^{16}$	0.1	0.13
$5\cdot10^{16}$	$9\cdot10^{16}$	0.1	0.17

Figure 3.11 Effects of the band bending variation on the photocurrent with: a) Five different values of band bending Φn at the cathode and a constant Φp=0.1eV at the anode. b) Five different values of band bending Φp at the anode and a constant Φn=0.1eV at the cathode. The table below each plot shows the value of charge concentrations Nn, Np at the interfaces. The other fitting parameters are the same for all curves: $W_n=W_p=25nm$, $V_{BI}=0.78V$, $G_0=4.82\bullet10^{21}cm^{-3}s^{-1}$, $k_{REC}=5\bullet10^{3}s^{-1}$, $k_{SEP}=10^{4}s^{-1}$.

As an example, in Figure 3.11 two simulated photocurrents are plotted for different parameter values. In those plots it is assumed that a degradation occurred at the top interface (i.e. the illuminated side of the cell), as shown in Figure 3.11(a), and at the bottom interface (i.e. the non-illuminated side of the cell), as shown in Figure 3.11(b). Noticeably, the two shapes are very different, and this is a signature of the active layer – electrode barriers modification.

It is worth to remark that the proposed model simulates the active layer between two non-selective contacts[7], featuring an infinite extraction velocity. Clearly, a real solar cell may feature multiple interlayers between the active layers and the contacts, in order to improve the carrier extraction or to selectively block a carrier type. The presence of such interlayers may be taken into account by imposing the suitable boundary conditions, such as $J_n(0)=0$ for an ideal electron-blocking interlayer.

[7] A contact is said to be selective for electrons (hole) when it blocks electrons (holes), but allows the extraction of holes (electrons).

Constant charge distribution model

	R1	R2	R3
Charge distribution Q(x)	$-qN_n$	0	qN_p
Electric field F(x)	$-\frac{qN_n}{\varepsilon}(x-x_N)+E_0$	E_0	
Potential V(x)	$+\frac{qN_n}{2\varepsilon}(x-x_N)^2-E_0x$	$-E_0x$	$-\frac{qN_p}{2\varepsilon}(x-x_P)^2-E_0x$
Exponential charge distribution model			
Charge distribution Q(x)	$qN_pe^{\frac{x-L}{W_p}}-qN_ne^{-\frac{x}{W_n}}$		
Electric field F(x)	$E_0+\frac{qN_pW_p}{\varepsilon}e^{\frac{x-L}{W_p}}+\frac{qN_nW_n}{\varepsilon}e^{-\frac{x}{W_n}}$		
Potential V(x)	$-E_0x-\frac{qN_pW_p^2}{\varepsilon}e^{\frac{x-L}{W_p}}+\frac{qN_nW_n^2}{\varepsilon}e^{-\frac{x}{W_n}}$		

Table 5 Expression of charge, electric field and potential for constant charge model and exponential charge model.

3.5 Comparison between exponential and constant charge models

In Table 5 is shown the comparison between the equations of charge distribution, electric field and potential for each model (as functions of the position *x* inside the active layer). Of course, the sharp distinction between the three regions (as sketched in Figure 3.2) disappears, even though a negatively charged region near the cathode and a positively charged region near the anode can be still distinguished. They are separated by a quasi-neutral region in the bulk of the active layer. Unlike the case of constant charge approximation, in the case of exponential charge distribution, the equations cannot be analytically solved, but they need to be solved numerically.

Figure 3.12 shows the comparison between the band diagrams in the case of constant charge distribution, exponential charge distribution and the drift diffusion model. In order to plot the curves for the constant charge model, the same parameters used to fit the fresh curve in Figure 3.3(a) (red circles) were used. For the exponential model, the fitting parameters were tuned in order to keep constant the voltage drops and the total accumulated charge at the interfaces.

Compared to the constant charge distribution, the exponential charge distribution allows for a much better approximation of the band diagram, which has been calculated using a much more time consuming drift diffusion simulation. The good match between the exponential model

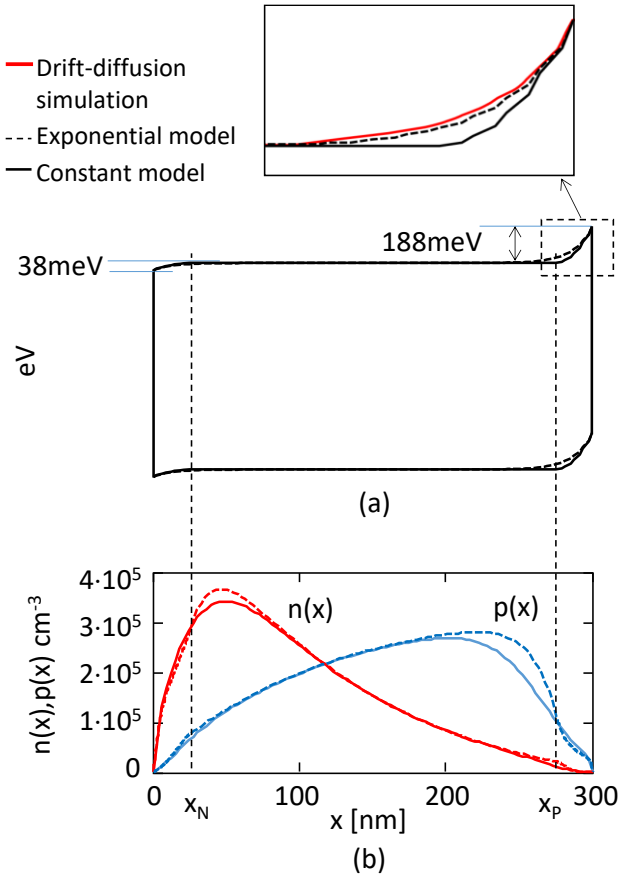

Figure 3.12 a) Comparison of the band diagram simulated with exponential (dotted line) and constant charge distribution (solid line) at the interfaces in quasi flat band condition. The figure on the top shows a zoom of the band bending at the anode and the comparison with the band shapes predicted with a drift diffusion simulation (red solid line). b) Photogenerated carrier distribution corresponding to the band diagram in Figure 3.12(a). Solid lines represent the constant charge model and dotted lines represent the exponential charge model.

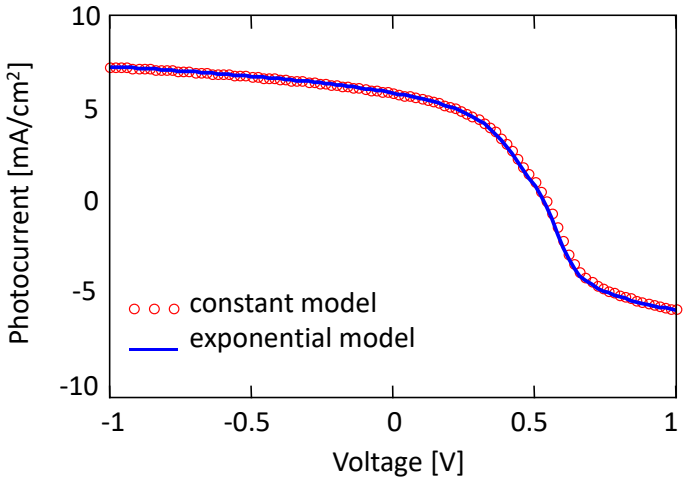

Figure 3.13 Comparison between the photocurrent simulated with the constant charge model (red circles) and exponential charge model (solid line).

and the drift-diffusion simulation has been highlighted in Figure 3.12(a) (red solid lines and black dotted line).

At this point, some considerations are worth to be drawn. Even though the constant charge distribution does not allow a perfect band diagram estimation, a very good agreement exists between the two predicted photogenerated carrier distributions, as shown in Figure 3.12(b). Moreover, the predicted photocurrents perfectly overlap each other, as shown in Figure 3.12(c). This suggests that the photocurrent does not strongly depend on the particular shape of the charge distribution, but only on the measure of the band bending and on the magnitude of the electric field. Incidentally, these two quantities represent the selectivity and the carrier extraction capability of the contacts, respectively. In fact, a large band bending at the cathode, for example, acts as a barrier for holes, preventing them to be extracted from the electrode. On the other hand, the large electric field – consequence of the large band bending – increases the electrons drift current, improving the carrier extraction. The opposite holds true at the anode.

3.6 Conclusions

In this chapter was presented a model proposed for explaining quantitatively the shape of the J_{PH}-V, the position of the zero field voltage and the built-in potential. Furthermore, it allows to quantitatively estimate the effect of the voltage drop at the electrodes and its effect on the internal electric field. Remarkably, it was also found that the shape of the bending at the contacts plays only a minor role in the J_{PH}-V shape, which mostly depends on the value of the barriers.

In addition, this model can be very helpful in calculating the electric field value inside the active layer, it can aid the interpretation of the appearance of multiple inflection points in the photocurrent and it can give indication about what interface is undergoing degradation during cell ageing. The relations identified between the photocurrent shape and the parameters variation allows to directly understand what characteristic of the solar cell is degrading.

For all these reasons, this model is an important tool for cells characterization and qualification, and it can be used also during reliability assessment, monitoring the degradation of the cells by means of electrical noninvasive measurements.

3.7 References

[Alt11] S. Altazin, R. Clerc, R. Gwoziecki, G. Pananakakis, G. Ghibaudo, C. Serbutoviez, “Analytical modeling of organic solar cells and photodiodes”, Appl. Phys., Vol. 99, p. 143301, Oct. 2011. doi: 10.1063/1.3643126

[Bra84] C. L. Braun, “Electric field assisted dissociation of charge transfer states as a mechanism of photocarrier production”, *J. Chem. Phys.*, Vol. 80, n. 9, pp. 4157–4161, 1984, doi:10.1063/1.447243

[Car13] J. E. Carlé et al., “A laboratory scale approach to polymer solar cells using one coating/printing machine, flexible substrates, no ITO, no vacuum and no spincoating,” Solar Energy Mater. Solar Cells, vol. 108, pp. 126–128, Jan. 2013.

[Ces15] A. Cester, A. Rizzo, A. Bazzega, N. Lago, J. Favaro, M. Barbato, N. Wrachien, S.A. Gevorgyan, M. Corazza, F.C. Krebs, “Effects of constant voltage and constant current stress in PCBM: P3HT solar cells”, Microelectronics Reliability, Vol. 55, n.9-10, p. 1795-1799, 2015.

[Kim06] Y. Kim, S. Cook, S. M. Tuladhar, S. A. Choulis, J. Nelson, J. R. Durrant, D. D. C. Bradley, M. Giles, I. McCulloch, C. Ha, M. Ree, “A strong regioregularity effect in self-organizing conjugated polymer films and high-efficiency polythiophene:fullerene solar cells”, Nature materials, Vol. 5, p. 197-203, March 2006.

[Lee10] W. H. Lee, S.Y. Chuang, H. L. Chen, W. F. Su, C. H. Lin, “Exploiting Optical Properties of P3HT:PCBM film for organic solar cells with semitransparent anode”, Thin Solid Films, Vol. 518, p. 7450-7454, May 2010.

[Lim10] M. Limpinsel, A. Wagenpfahl, M. Mingebach, C. Deibel, and V. Dyakonov, “Photocurrent in bulk heterojunction solar cells,” *Phys. Rev. B*, Vol. 81, n. 8, p. 085203, Feb. 2010. doi: 10.1103/PhysRevB.81.085203

[Mar08] R. A. Marsh, C. R. McNeill, A. Abrusci, A. R. Campbell, and R. H. Friend, “A unified description of current–voltage characteristics in organic and hybrid photovoltaics under low light intensity”, Nano Lett. Vol. 8, p. 1393-1398, 2008.

[Ooi08] Z. E. Ooi, T. L. Tam, A. Sellinger, and J. C. deMello, “Field-dependent carrier generation in bulk heterojunction solar cells,” Energy Environ. Sci., vol. 1, pp. 300–309, May 2008.

[Riz16a] A. Rizzo et al., “Effects of current stress and thermal storage on polymeric heterojunction P3HT:PCBM solar cell,” in Proc. IEEE Int. Rel. Phys. Symp. (IRPS), Pasadena, CA, USA, Apr. 2016, pp. 3C-2-1–3C-2-6.

[Riz16b] A. Rizzo et al., “Characterization and modeling of organic (P3HT:PCBM) solar cells as a function of bias and illumination,” Solar Energy Mater. Solar Cells, vol. 157, pp. 337–345, Dec. 2016.

[Sok82] R. Sokel and R. C. Hughes “Numerical analysis of transient photoconductivity in insulators”, *J. Appl. Phys.*, Vol. 53, n. 11, p. 7414, Nov. 1982. doi: 10.1063/1.330111

Chapter 4 The Open Circuit Voltage Decay model

4.1 Introduction

In order to improve the reliability of the organic solar cells, a thorough study of the devices under many points of view. The model described in Chapter 3 partially satisfies this need, allowing to extrapolate information about the device capability to separate polaron and about the polaron recombination rate. Anyway, there are still many information that can be extrapolated only by means of destructive measurements (for example, the energy band of the materials involved in the active layer blend of a polymeric solar cell). Being the working principle of the organic solar cell only slightly similar to that of inorganic solar cells, it would be desirable to find a measurement technique which allows to extrapolate all these information without damaging the device in use. Furthermore, it would be useful to have a tool capable of giving information about the device even during its normal operation. This would permit to have a good understanding of the degradation of the solar cells during their normal operation, monitoring their health and suggesting what to change in order to improve the devices reliability.

Of course, in order to analyze the data obtained by means of this measurement, it is also necessary to develop a model capable of extrapolating the most important information from the solar cell.

There are already models that have been developed in literature, and they are mainly based on the photocurrent produced by a photovoltaic organic device [Sok82][Ons38][Alt11][Ooi08][Lim10][Tor16]. Some efforts have also been made to model the

impedance as a function of frequency [Riz16][Rip12], obtaining important information such as the carrier lifetime estimation, the transport resistance of the active layer, etc. This one in particular is a non-destructive measurement tool, but it is difficult to implement and it requires a hard work to analyze data.

Another measurements technique, the Open Circuit Voltage Decay (OCVD), has been proposed to analyze the recombination mechanisms in dye-sensitized solar cells (DSSC) in [Zab03]. In the same work, a model has been proposed in order to describe the voltage decay in open circuit condition for DSC and to extrapolate the carrier lifetime.

This chapter aims to extend to polymeric solar cells the OCVD technique and to develop a suitable model, which accounts for the peculiar generation and recombination mechanisms of polymeric solar cells. In the beginning, a description of the OCVD measurement technique will be given. After that, a new model capable of explaining the results of the OCVD measurements performed on polymeric solar cells will be presented. This model allows to understand the different recombination mechanisms involved in solar devices. In order to validate the model, it will be applied to the experimental results obtained in a P3HT:PCBM solar cell, which will be used as reference. Then, the model will be applied in order to analyze the experimental data obtained from stressed devices and from device made of different polymers.

In Chapter 6, an advanced version of this model will be given. It requires a heavier computational effort, due to its higher complexity and due to the impossibility to give an analytical expression for its results.

4.2 Open circuit voltage decay measurement description

The Open Circuit Voltage Decay (OCVD) measurement was developed for the first time in [Zab03]. As already said in the Introduction to this chapter, it was focused on photoelectrochemical cells based on nanoscaled porous metal oxide semiconductors (dye-sensitized solar cell, or DSSCs).

The most important information provided by OCVD is the estimation of the carrier lifetime inside the solar cell. Of course, there are many other measurement techniques which allow to obtain these data, and they are based on frequency measurements and steady-state measurements. Furthermore, some measurements are very invasive (they need to destroy the solar cell in order to obtain the measurements), and some measurements require a huge amount of data and analysis to be properly used. On the contrary, OCVD is a relatively simple

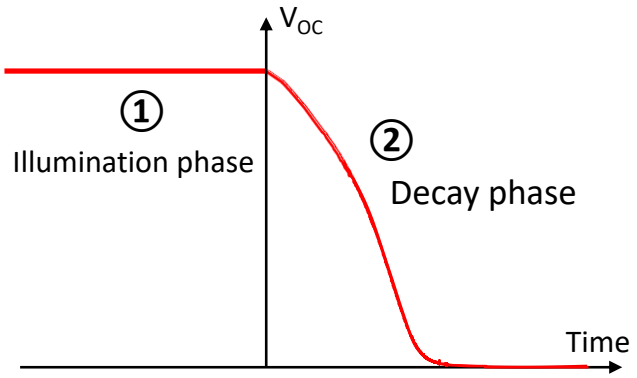

Figure 4.1 Simulation of the decay transient of the open circuit voltage generated by a solar cell. During phase 1 (illumination phase) the cell is polarized at V_{OC}, while during phase 2 (decay phase), V_{OC} decays following a similar behavior to the decay sketched in figure.

measurement techniques, both from the point of view of its implementation, and from the point of view of its data extrapolation. More important, it is not an invasive measurement, and it requires just a reading of the V_{OC} of the cell under illumination to be performed. Note that this is not a stressing measurement, because it only requires that the cell works in its operative condition. Furthermore, the simplicity of the OCVD measurement allows its implementation even during the normal functioning of the device. This might be a very important advantage, because it could give information about the health of the solar cell.

OCVD provides a continuous reading of the charge lifetime as a function of V_{OC}. This may lead to very important results about carrier recombination inside the active layer.

OCVD can be divided ideally in two phases: the illumination phase and the decay phase. During both of them, the device is held in open circuit condition, so that no charges can be extracted from the electrodes. Figure 4.1 shows an example of the V_{OC} decay. In order to help identifying the two phases, they are marked with 1 and 2. The decay shown is just a simulation obtained by means of the developed model, and does not represent data extrapolated from a real solar cell.

- Illumination phase: this phase begins when the device under test[8] is illuminated by a light source. In Figure 4.1 this phase is associated to $t<0$. The illumination time must be long enough to guarantee that an equilibrium condition (i.e. electron generation rate balances recombination rate) is reached in the active

[8] The devices used in this work are only polymeric solar cells, but the techniques can be used for any device capable of photogeneration, even inorganic solar cells. In this case, though, the measurement tool must be capable of very, very fast sampling (due to the velocity of the exciton recombination in the inorganic materials, as already explained in 2.3.2).

layer of the device. The source of light can be a solar simulator or a white LED (WLED hereafter) at a given illumination power. All the OCVD measurements shown in this work are performed by means of a WLED.

When equilibrium is reached, the solar cell is polarized at its open circuit voltage, which must be stable (unless degradation occurs; in that case it would be better to shorten the illumination time in order not to furtherly degrade the device and to guarantee a reliable measurement).

- Decay phase: during the second phase, the light source is switched off and the photovoltaic device is not illuminated anymore (dark condition). This phase starts at t=0 in Figure 4.1 and the device is still held in open circuit condition.

  Due to carrier recombination, the voltage produced by the device starts decaying in a time that depends on the cell type. In organic solar cells, the decay time might last a few milliseconds (for polymeric solar cells) or even some seconds (Perovskite-based solar cells).

As will be shown later, the model is focused on the decay phase, where many information about carrier recombination can be extrapolated.

4.3 OCVD analysis

Figure 4.1 shows a sketch representative of the voltage produced by the solar cell during the illumination phase and after the light is switched off. As already mentioned, during the illumination phase the cell is polarized in open circuit voltage V_{OC}, while during the decay phase, the voltage produced by the device decreases.

4.3.1 Recombination mechanisms during OCVD

Being the device held in open circuit condition during the decay (i.e. the electrodes are in high impedance condition), the V_{OC} decrease is ruled only by the carrier recombination inside the active layer.

Before going on, it is worth to briefly describe the mechanisms of recombination involved during the decay phase.

- The first analyzed mechanism is the **trap-assisted recombination**, which is described by the Shockley-Read-Hall (SRH) model [Kui11]. According to this theory, the recombination rate is given by this equation:

$$R_{SRH} = \frac{np - n_i^2}{\tau_n(p + n_i) + \tau_p(n + n_i)} \qquad (4.1)$$

  Where τ_n and τ_p represent, respectively, the average lifetime of electrons and holes before each carrier is captured by a recombination center. In an organic electronics this recombination mechanism is pretty common and it is related to the presence of defects in the material molecules.

  When a carrier recombines via trap-assisted recombination, it does not participate anymore to the open circuit voltage, thus going into a neutral state.

- **Bimolecular recombination**, which is described by the Langevin model, already described in 2.7.1 and initially developed in [Lan03]. According to this interpretation, the recombination rate of the photogenerated carrier is described by the following equation:

$$R_L = \gamma(np - n_i^2) \qquad (4.2)$$

  Where γ is the Langevin recombination coefficient, n and p are the concentrations of electron and holes, respectively. R_L is the recombination rate, expressed in $cm^{-3}s^{-1}$ and n_i is the intrinsic carrier concentration. It is worth to remark that, unlikely what reported in 2.7.1, the recombination rate depends on the product of the photogenerated carrier concentrations, which is given by $np - n_i^2$.

  According to the Langevin theory, in disordered solids, and in particular in organic semiconductors, bimolecular recombination between an electron and a hole happens only when an electron is attracted by the Coulomb force radius to the hole (and viceversa). When this happens, and the two carriers become very close to each other, the two carriers become a polaron. Thus, the parameter R_L expresses the velocity at which an electron-hole pair returns to its polaron state. This parameter was not taken into consideration in the models presented so far, and it was neglected both in the model developed in 0 and in the model developed by Sokel-Hughes and Braun Onsager. Remarkably, R_L differs from the recombination rate k_{REC}, which quantifies the polaron pair recombination instead.

4.3.2 Parameters describing the OCVD

It is worth to remind that, when the solar cell is illuminated, the incident photons generate excitons with a rate G_A (considered constant in all the active layer). In order to create bounded polaron pairs, the excitons must be dissociated in close proximity of the acceptor/donor interface (see 2.3.2). Besides, in order to generate free carriers, the polaron pairs must be separated, as described by the Braun-Onsager model [Bra84][Ons38].

For clarity, all the processes involved during photogeneration are sketched in Figure 4.2. This diagram is very similar to that used in Figure 2.11, even though some additions are made in order to develop a model as close to reality as possible.

The first change regards the excitons kinetics: for example, once generated, not all of them can be dissociated into polaron pairs, as supposed by the models developed so far. The excitons may decay to the ground state or they may dissociate, actually producing bounded polaron pairs. To take into account quantitatively these non-idealities, the rate of the first phenomenon is named k_{DEC} and the rate the latter is named k_{DISS}. Both are measured in s^{-1}, thus representing the number of decaying excitons per second and the number of dissociated exciton per second, respectively.

S and *X* are the volume concentration of excitons and polaron pairs, respectively (measured in cm^{-3}). Of course, *X* is related to the excitons concentration: in fact, the generation rate due only to exciton dissociation is:

$$G_X^* = k_{DISS} S \qquad (4.3)$$

As was said in 4.3.1, the polaron pairs are generated also as a consequence of the recombination of a free electron and a free hole. For this reason, the polaron pair generation rate in equation (4.3) is not named G_X, but G_X^*.

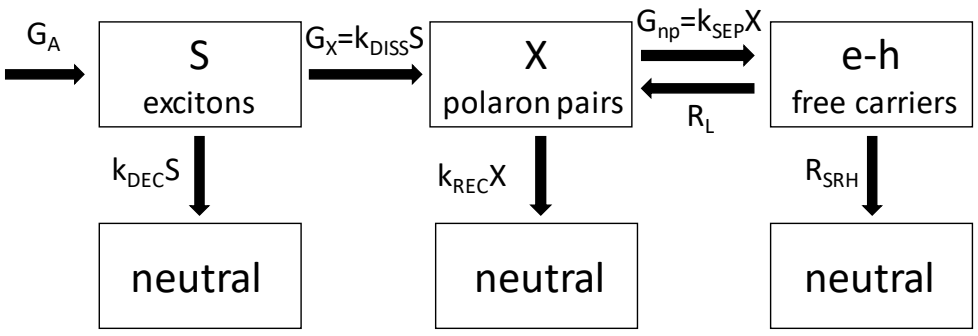

Figure 4.2 Schematic representation of the mechanisms involved in exciton, polaron pairs and free charges dynamics during the illumination phase of the OCVD. All the parameters that appear in this figure were explained in Chapter 2 and Chapter 3.

Symbol	Unit	Meaning
S	cm^{-3}	Exciton concentration
X	cm^{-3}	Polaron pairs concentration
n,p	cm^{-3}	Electron, holes concentration
G_A	$cm^{-3}s^{-1}$	Exciton generation
G_X	$cm^{-3}s^{-1}$	Polaron pairs generation
G_{np}	$cm^{-3}s^{-1}$	Electron and holes generation
k_{DEC}	s^{-1}	Exciton decay rate
k_{DISS}	s^{-1}	Exciton dissociation rate
k_{REC}	s^{-1}	Polaron pairs recombination rate
k_{SEP}	s^{-1}	Polaron pairs separation rate
k_R	s^{-1}	Ratio k_{REC}/k_{SEP}
R_L	$cm^{-3}s^{-1}$	Langevin Recombination rate
R_{SRH}	$cm^{-3}s^{-1}$	SRH recombination rate
R	$cm^{-3}s^{-1}$	Total carrier recombination rate (R_L+R_{SRH})
γ	$cm^{3}s^{-1}$	Bimolecular recombination coefficient
τ, τ_n, τ_p	s	Carrier lifetime of SRH model

Table 6 Symbols and notations used in this model. See also Figure 4.2 for more information about the rates used as fitting parameters.

Accordingly to Braun-Onsager, the polaron pair concentration may recombine to a ground state with a rate k_{REC}, or may separate with a rate k_{SEP}. Despite the polaron pairs separation dependence on the electric field inside the active layer, in the following analysis k_{SEP} will be assumed constant for simplicity. This is a reasonable assumption because, during OCVD, the device is unbiased and it works in a voltage range from V_{OC} (at the beginning of the decay, i.e. the instant when the light is switched off) to 0 (i.e. short circuit condition, at the end of the decay). In this region, the electric field is weak and it has only a moderate impact on the polaron pairs separation probability. In fact, it is verified that the separation probability weakly changes from 77% in open circuit condition to 88% in short circuit condition. Using a constant k_{SEP} value, the generation rate of free electrons and free holes can be expressed by this equation: $G_{np} = k_{SEP}X$.

The free carriers can recombine or can be extracted by the electrodes and, as described in 4.3.1, electrons and holes recombination can be of two different types. All the carriers that undergo bimolecular recombination return to a polaron pair state with a rate R_L. Remarkably, the Langevin bimolecular recombination represents an additional generation mechanism for the polaron pairs (which concentration is X). Equation (4.3) is modified and the polaron pairs generation rate becomes:

$$G_X = k_{DISS}S + R_L \qquad (4.4)$$

Conversely, if the free carriers recombine via recombination centers (trap-assisted recombination), no polaron pairs are generated and the free electrons and holes directly recombine to a neutral state with a rate R_{SRH}. This mechanism only accounts for a decrease in the polaron pair generation and for a decrease in the total number of free charges that can be extracted from the solar cell.

Table 6 summarizes all the notations used in this chapter.

4.4 OCVD modeling

In the first part of this chapter was given a description of the generation and recombination phenomena involved in the open circuit voltage decay measurement. The mathematical description of these phenomena can be used to model the voltage decay measured during the decay phase of the OCVD. In order to do this, the analysis must start from the illumination phase, which will provide many essential information useful to fully develop the model.

4.4.1 Illumination phase

The variation in time of polaron pairs concentration *X* and of the carrier concentrations *n* and *p* (see Figure 4.2) are expressed as:

$$\begin{cases} \dfrac{dX}{dt} = G_X + R_L - (k_{REC} + k_{SEP})X \\ \dfrac{dn}{dt} = \dfrac{dp}{dt} = k_{SEP}X - R_L - R_{SRH} \end{cases} \qquad (4.5)$$

These are general equations, and are always valid during all the OCVD measurement.

When the device has been illuminated for a time long enough, the active layer is in steady state, i.e. exciton recombination rate is equal to exciton generation rate. The same holds true for polaron pairs and free carriers. For these reasons, the same procedure adopted in 2.7.2 can be used. In fact, the following equations are valid:

$$G_A = (k_{DEC} + k_{DISS})S \qquad (4.6)$$

$$G_X + R_L = (k_{SEP} + k_{REC})X = \frac{X}{\tau_X} \qquad (4.7)$$

$$G_{np} = k_{SEP}X = R_L + R_{SRH} \qquad (4.8)$$

The right-side of Equation (4.7) represents the recombination rate of the polaron pairs. This term can be rewritten as X/τ_X, where τ_X represents the mean lifetime of the polaron pairs. Being equations (4.7) and (4.8) valid at the same time, (4.7) can be used in (4.8). This gives the following relation:

$$G_{np} = \frac{k_{SEP}}{k_{REC} + k_{SEP}}(G_X + R_L) = P_{SEP}(G_X + R_L) \qquad (4.9)$$

Where P_{SEP} is the separation probability of the polaron pairs. Differently from the separation probability of Equation (2.16), this term does not depend on the electric field due to the assumption made in 4.3.2 on k_{SEP}. P_{SEP} can be rewritten using $k_R = \frac{k_{SEP}}{k_{REC}}$:

$$P_{SEP} = \frac{k_{SEP}}{k_{REC} + k_{SEP}} = \frac{1}{1 + k_R} \qquad (4.10)$$

A similar expression can be obtained for exciton dissociation. Substituting (4.6) in (4.3), and neglecting the recombination rate R_L:

$$G_X^* = \frac{k_{DISS}}{k_{DISS} + k_{DEC}} G_A = P_{DISS} G_A \qquad (4.11)$$

In this equation, P_{DISS} is defined as the exciton dissociation probability.

In order to develop a general model of the voltage decay, also a potential intrinsic doping of the active layer is considered. In equilibrium conditions the electron concentration is n_0, and the hole concentration is p_0. It holds true that $n_0 \neq p_0 \neq n_i$, but $n_0 p_0 = n_i^2$.

During illumination, additional free charges are photogenerated inside the active layer. Their concentrations are expressed by two additional terms Δn and Δp, for electrons and holes, respectively. The total electron and hole concentrations are described by the following equations:

$$\begin{cases} n(t) = n_o + \Delta n(t) \\ p(t) = p_0 + \Delta p(t) \end{cases} \qquad (4.12)$$

Note that in this system of equations, n, p, Δn and Δp are expressed as functions of time. In the following, this dependence will be neglected for simplicity. These terms remain constant during the first phase of the OCVD, and it is always true that $\Delta n = \Delta p$ (In fact, the generation of an electron always corresponds to the generation of a hole).

System of equations in (4.12) can be used in (4.5), together with the expressions for R_L and R_{SRH} reported in Equations (4.1) and (4.2).

$$\begin{cases} \dfrac{dX(t)}{dt} = G_X + \gamma[(n_0+\Delta n)(p_0+\Delta p) - n_0p_0] - (k_{REC}+k_{SEP})X \\ \dfrac{dn}{dt} = \dfrac{dp}{dt} = k_{SEP}X(t) - \gamma[(n_0+\Delta n)(p_0+\Delta p) - n_0p_0] - \dfrac{[(n_0+\Delta n)(p_0+\Delta p) - n_0p_0]}{\tau_n(p_0+\Delta p+n_i)+\tau_p(n_0+\Delta n+n_i)} \end{cases}$$

The expressions can be simplified assuming that electrons and holes have the same lifetime (thus $\tau_n = \tau_p = \tau'$), and considering that in equilibrium conditions (i.e. during illumination phase) *n*, *p* and *X* do not vary. Furthermore, being $\Delta n = \Delta p$:

$$\begin{cases} G_X + \gamma[\Delta n(n_0+p_0) + \Delta n^2] = (k_{REC}+k_{SEP})X(t) \\ k_{SEP}X(t) = \gamma[\Delta n(n_0+p_0) + \Delta n^2] + \dfrac{[\Delta n(n_0+p_0) + \Delta n^2]}{\tau'(p_0+n_0+2\Delta n+2n_i)} \end{cases}$$

From the first equation of the system, an expression for the polaron pairs concentration *X* can be obtained:

$$X(t) = \frac{G_X + \gamma[\Delta n(n_0+p_0) + \Delta n^2]}{k_{REC}+k_{SEP}} \qquad (4.13)$$

Besides, the system can be solved in order to obtain the expression for Δn. Substituting (4.13) in the system of equation, it can be found a three-order equation:

$$a_3\Delta n^3 + a_2\Delta n^2 + a_1\Delta n + a_0 = 0$$

Where the coefficients depend on several of the parameters cited until now, and are written here:

$$a_1 = \gamma\tau(1-P_{SEP})AB + A - 2P_{SEP}G_X\tau$$

$$a_2 = (2A+B)\gamma\tau(1-P_{SEP}) + 1$$

$$a_3 = 2\gamma\tau(1-P_{SEP})$$

$$a_0 = -P_{SEP}G_X\tau B$$

With $A = n_0 - p_0$ and $B = n_0 + p_0 + 2n_i$.

The solution of the third grade equation gives a general expression for $\Delta n = \Delta p$. This expression is very general and, unless some approximations are made, its solution is very complicated. For this reason, the expression for Δn will not be shown here.

Remarkably, because the photogenerated carrier concentration does not change during the steady-state illumination phase, $\Delta n = \Delta n(0) = \Delta p(0)$ (i.e. at the instant when the light is switched off and the voltage decrease begins). Thus, the system solution Δn can be used in (4.13) to find the polaron pair concentration at the end of the illumination phase, *X(0)*.

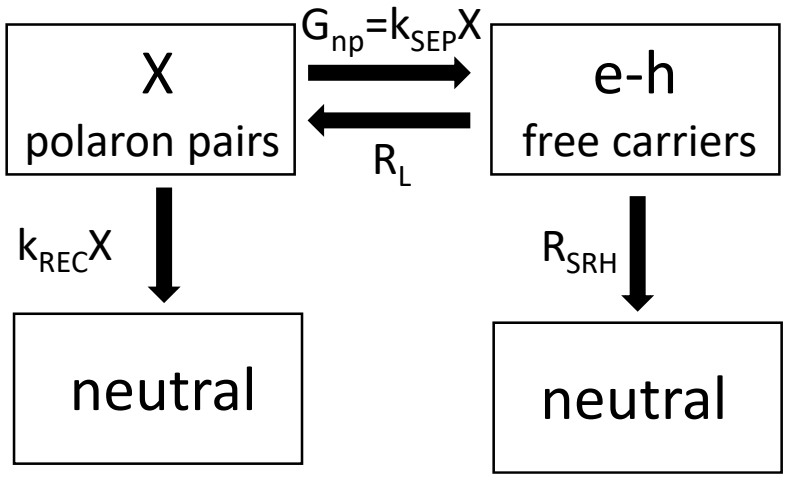

Figure 4.3 Schematic representation of the mechanisms involved in exciton, polaron pairs and free charges dynamics during the decay phase of the OCVD (after the light is turned off).

4.4.2 Decay phase

As it was done for the illumination phase, also the decay phase of the OCVD can be analyzed and described by means of differential equations. As happened in the illumination phase, also the solution of these new equations must be found numerically, due to the problem complexity. After the mathematical discussion, an example of simulated voltage decay will be shown. This will be helpful to understand how changing the parameters reflects on the variation of the voltage decay.

As previously said, during the decay phase the solar device is kept in open circuit condition under no illumination bias. For this reason, the electrodes extract no charges and the only responsible for the voltage decay is the charge recombination inside the active layer. During the decay, there are some differences in the parameters expressions, if compared to the expressions given in 4.4.1.

First of all, no exciton generation is observed when light is switched off, thus $G_A=0$ (see Table 6 and Figure 4.2 for notations). This implies that G_X vanishes in the first few nanoseconds, that is the typical exciton lifetime. In this analysis, it can be assumed that G_X becomes zero as soon as the light is switched off. In fact, the first sample of the OCVD decay is taken after a few microseconds after the light is switched off (t=0), making negligible the vanishing time of the excitons.

Conversely, there are no differences in the free carriers generation, which can be still expressed as $G_{np}(t) = k_{SEP}X(t)$. The time dependence is now made clear, because carrier

Symbol	Value
γ	$10^{-12}cm^3s^{-1}$
G_X	$10^{21}cm^{-3}s^{-1}$
$n_0=p_0=n_i$	$10^{12}cm^{-3}$
τ	$10^{-3}s$
$k_{REC}=k_{SEP}$	$[10^{-3}-10^{6}]s^{-1}$

Table 7 List of the parameters used to plot n(t)=p(t) and X(t) of Figure 4.4.

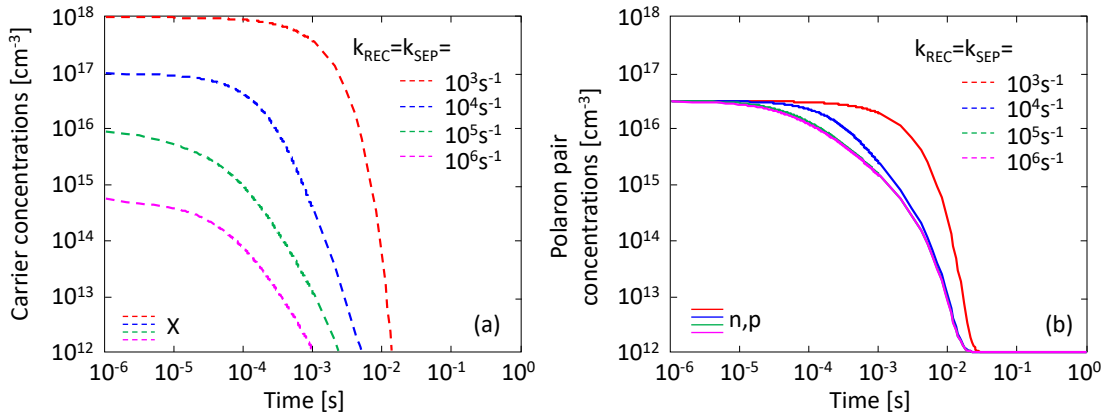

Figure 4.4 Carriers and polaron pair concentrations numerically calculated starting from the system of equation (4.14). Different values of the parameters k_{REC} and k_{SEP} has been used, while the doping has been neglected. Solid lines are the electron and hole concentrations, dashed lines are the polaron pair concentration. Different colors are associated to different parameters values.

generation rate and polaron pairs concentration change during the voltage decrease of the second part of OCVD.

The cell is not in steady state condition anymore, so (4.6), (4.7) and (4.8) cannot be considered valid. The diagram reported in Figure 4.2 modifies as reported in Figure 4.4.

The system of equations (4.12) is still valid, except that now n(t)≠n(0), p(t)≠p(0), Δn(t)≠Δn(0) and Δp(t)≠Δp(0). Conversely, being G_X=0, the system of equations (4.5) becomes:

$$\begin{cases} \dfrac{dX}{dt} = R_L - (k_{REC} + k_{SEP})X \\ \dfrac{dn}{dt} = \dfrac{dp}{dt} = k_{SEP}X - R_L - R_{SRH} \end{cases} \qquad (4.14)$$

This system of equation can be numerically solved for *X(t)*, *n(t)* and *p(t)* assuming *n(t)=p(t)* during the decay and using the initial values calculated in 4.4.1 (via numerical procedure). The solutions *n(t)* and *X(t)* of (4.14) are plotted in Figure 4.4(a) and (b) as functions of time for different values of k_{REC}, which is supposed equal to k_{SEP} just for this simulation. All the curves were

plotted using the fixed parameters listed in Table 7 and using solid lines for *n(t)* and *p(t)*, and dashed lines for *X(t)*.

When k_{REC} and k_{SEP} are small, the process of conversion from polaron pairs to free electrons and holes, as well as the polaron pair recombination to a neutral state, is very low. Thus, the polaron pair concentration is higher than the carrier concentration and the polaron pair lifetime is very long. In particular, it does not decrease before about one millisecond, as demonstrated by the red, solid line of Figure 4.4(b). This reflects also on the free carrier density, plotted as a red, dotted line in Figure 4.4(a). In fact, to a high value of *X* corresponds a high value of $G_{np} = k_{SEP}X$, which keeps the free carriers concentration generation high until *X* remains high.

Increasing k_{REC} and k_{SEP} from $10^3 s^{-1}$ to $10^4 s^{-1}$, X decreasing anticipates. *n* and *p* remain constant until *X* starts decreasing too, following the same behavior noticed before.

When k_{REC} and k_{SEP} are large ($10^5 s^{-1}$, $10^6 s^{-1}$), *X* becomes much smaller than *n* and *p* at the beginning of the decay (in fact, Equation (4.13) shows that *n* and *p* are inversely proportional to k_{SEP} and k_{REC}). Furthermore, the evolution of *n* and *p* is now different from the evolution of the polaron pair concentration, which exhibits a larger number of different slopes (see the green and purple solid lines in Figure 4.4(b)).

The same trend was observed for the voltage decay, which can be calculated starting from the carrier concentration. In order to do this, it is not enough to consider the presence of the free carriers inside the active layer, but also the polaron pairs must be taken into account. Each polaron pair, in fact, consists of one electron in the LUMO of the acceptor and one hole in the HOMO of the donor. For this reason, there is no difference between a free electron and an electron belonging to a polaron pair, because in both cases they reside in the same band and are responsible for the generation of an electric field and of the band bending. The only difference is that an electron in the polaron pair is bounded to its own hole (the same holds true for holes, that are bounded to their own electrons).

For these reasons, the total number of electrons responsible for the generation of the open circuit voltage is the sum of the free electrons and of the polaron pairs: $n + X$. Similarly, the total number of holes is $p + X$. Since the open circuit voltage depends on the total number of electrons present in the acceptor LUMO band and on the total number of holes present in the donor HOMO band, the voltage generated by the cell at a time *t* is:

$$V_{OC}(t) = V_T \ln\left[\frac{\big(n(t) + X(t)\big)\big(p(t) + X(t)\big)}{n_i^2}\right] \qquad (4.15)$$

Using the equations for the decay of the polaron pair concentration and of the free carrier concentration, it is possible to plot the voltage decay as a function of time (i.e. the voltage decay measured during OCVD). In Figure 4.5 is shown the simulated voltage decay associated to the free carrier and polaron pair decay shown in Figure 4.4.

When k_{REC} and k_{SEP} are low, $V_{OC}(t)$ in Figure 4.5 follows the evolution of $X(t)$. Instead, when k_{REC} and k_{SEP} are high, the evolution of $V_{OC}(t)$ is more similar to the free carrier concentrations evolutions. In order to help to understand this behavior, the decay of $G_{np} = k_{SEP}X$ is also plotted in Figure 4.6, together with the decay of the carrier recombination rate $R = R_L + R_{SRH}$.

It has already been observed that even k_{SEP} is small, $G_{np}=k_{SEP}X$ remains high for more than 1ms, resembling the polaron pair concentration decay. This means that, even though the light has

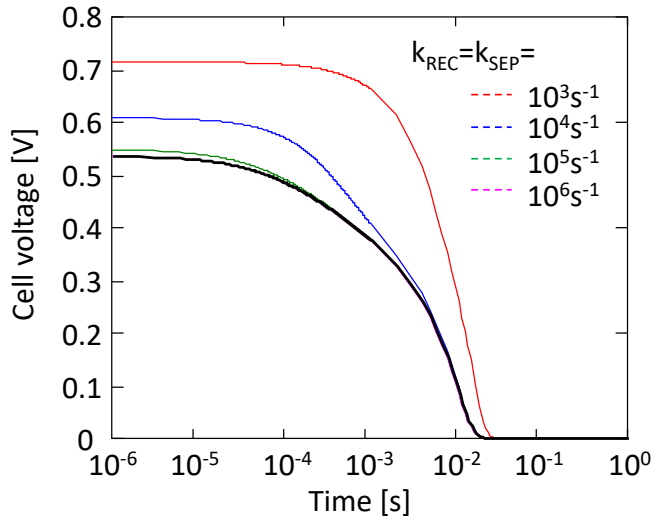

Figure 4.5 Simulated voltage decay for different values of k_{REC}, considered equal to k_{SEP}. The simulation was obtained using the n(t) and X(t) decays shown in Figure 4.4.

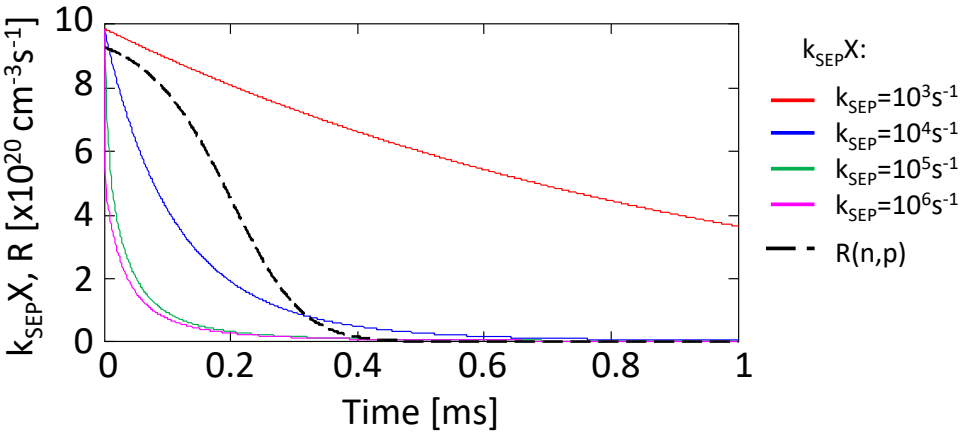

Figure 4.6 Comparison between the carrier recombination rate (black, bold, dashed line) and the carrier generation rate due to polaron pairs separation ($G_{np}=k_{SEP}X$). The plot shows the simulation for different values of k_{SEP}.

been switched off at t=0, electrons and holes are still being generated. This is further confirmed by the red curve of G_{np} in Figure 4.6. This is due to the low level of k_{SEP}, which ensures a slow conversion of the polaron pairs into free carriers. This is also the reason why $V_{OC}(t)$ remains high for more than 1ms when k_{REC}(=k_{SEP}) is low.

Conversely, when k_{SEP} increases over $10^5 s^{-1}$, G_{np} vanishes in a few tens of microseconds. Differently from what happens in the case of low k_{SEP}, all the polaron pairs are now fast converted into free carriers, determining a more abrupt decrease in G_{np} if compared to the previous case.

4.4.3 Analytical solution for carrier concentration during the decay phase

As already said before, in order to obtain an analytical expression for the electrons and holes distributions inside the active layer, it is necessary to introduce some approximations in the model. Although a numerical solution is very good to understand how the solar device works, an analytical solution to gives an immediate comprehension of the parameters incidence on the device working mechanisms. Furthermore, it allows an easier and faster implementation and simulation of the voltage decay.

The aim of this section is to develop an analytical model to fit the OCVD measurements. In order to do this, some approximations to the analysis made in 4.4.1 and 4.4.2 are needed and will be introduced. They are applicable to the devices studied in this work, as will be shown later. In the following, the analysis will be supported by several simulation examples made for different combinations of the solar cell parameters.

Figure 4.6 shows the evolution of G_{np} for different values of k_{SEP}. Noticeably, G_{np} decreases very fast (in fact, in less than 100μs the transient is almost over), determining a fast decrease of $X(t)$. It is reasonable to assume that G_{np} quickly vanishes as soon as the light is switched off: $G_{np}(t)$ = 0 for t>0, assuming that t=0 is the instant at which the light is switched off.

This simple assumption permits to analytically solve the system of equation (4.14), giving

$$\Delta n = n' \left[\coth\left(n'\gamma' t + acoth\left(\sqrt{1 + \frac{G_{np0}}{n'^2 \gamma'}} \right) \right) - 1 \right] \qquad (4.16)$$

Where:

$$\gamma' = \gamma(1 - P_{SEP})$$

$$n' = \frac{n_i^2 + N_{DOP}^2}{2N_{DOP}}$$

In this equation, $G_{np0}=P_{SEP}G_X$ represents the steady state carrier generation rate during the illumination phase (i.e. the carrier generation rate an instant before the light is switched off). Besides, the contribution of a potential doping has been included by means of the parameter N_{DOP}, which is expressed in cm^{-3}.

Introducing the approximation $G_{np}(t) = 0$ for $t>0$ is equivalent to assume that the voltage decay is independent from the presence of excitons inside the active layer.

Furthermore, the voltage decay in OSCs are not affected by the presence of doping. For this reason, the model can be simplified assuming that no doping is present inside the active layer and $N_{DOP}=0$ and $n_0=p_0=n_i$. This implies that, being $\Delta n = \Delta p$, the concentrations of electrons and holes are the same ($n=p$).

In these conditions, the equation describing the decay of the carrier concentration (second equation of the system (4.14)) becomes very simple:

$$\frac{dn}{dt} = \frac{dp}{dt} = G_{np0} - \gamma\left(n^2 - n_i^2\right) - \frac{n - n_i}{2\tau} \qquad (4.17)$$

In this case, τ does not represent the lifetime of a single carrier species (n or p), but the mean value of the electron and hole carrier lifetime ($\tau = \frac{\tau_n+\tau_p}{2}$). From (4.17) it is possible to extrapolate an expression for the initial condition of the carrier concentration, $n(0)$. In fact, during the illumination phase, the device is in steady state condition: for this reason, the derivative with respect to time must be zero. Equation (4.17) can be analytically solved as:

$$n(0) = -\frac{1}{4\gamma\tau} \pm \frac{1}{2\gamma}\sqrt{\frac{1}{(2\gamma)^2} + 4\gamma\left(G_{np0} + 4\gamma\left(G_{np0} + \gamma n_i^2 + \frac{n_i}{2\tau}\right)\right)} \qquad (4.18)$$

4.4.4 The two phases in the voltage decay

During the decay phase two different regions can be distinguished, depending on the carrier concentrations. This is a crucial point in the analysis of the open circuit voltage decay, and it is the key-point that allows to extrapolate the majority of information about carrier recombination in a solar cell.

1. During the first part of the decay, the carrier concentration is high and almost constant (see the simulations in Figure 4.4). In particular $n>>n_i$ and the dominant recombination mechanism is bimolecular. The trap assisted recombination is negligible ($R_L>>R_{SRH}$). In fact, being:

$$R_L = \gamma(n^2 - n_i^2)$$

$$R_{SRH} = \frac{n^2 - n_i^2}{2\tau(n + n_i)}$$

For $n>>n_i$, $R_L \cong \gamma n^2$ and $R_{SRH} \cong \frac{n}{2\tau}$. Thus, $R_L>>R_{SRH}$ for t>0 (i.e. during the decay) and (4.17) becomes[9]:

$$\frac{dn}{dt} = R_L = -\gamma(n^2 - n_i^2) \qquad (4.19)$$

The solution of this differential equation gives the carrier concentration during the first phase of the voltage decay as a function of time:

$$n(t) = n_i \, coth\left(\gamma n_i t + acoth\sqrt{1 + \left(\frac{G_{np0}}{\gamma n_i^2}\right)}\right) \qquad (4.20)$$

The same result could be achieved starting from (4.16) and assuming that $n_0=n_i$ and $n'=ni$ (with N_{DOP} = 0).

2. The second phase begins when the carrier concentration (and, consequently, the open circuit voltage) starts decreasing. When the carrier concentration decreases significantly, the bimolecular recombination becomes weak if compared to the trap-assisted recombination, which is now the main recombination mechanism.

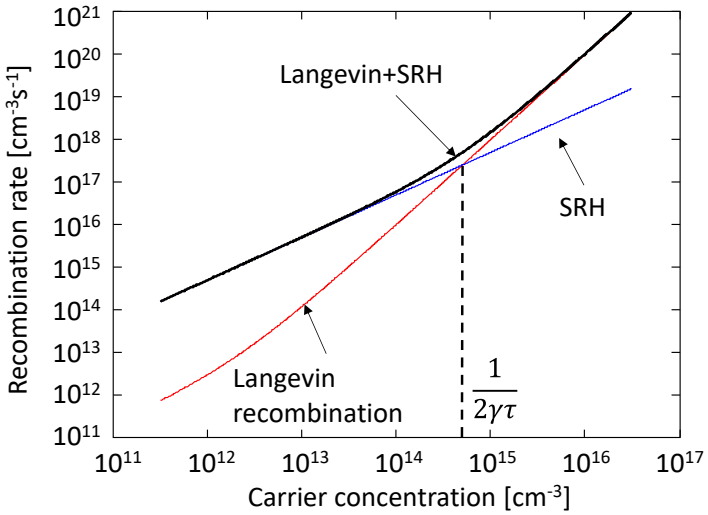

Figure 4.7 Recombination rates R_{SRH} and R_L as functions of the carrier concentration. In the plot are shown the evolutions of both Langevin (bimolecular) and SRH (trap-assisted) recombination. The critical value of carrier concentration which defines the transition between the Langevin recombination regime and the SRH recombination regime is the intersection point between R_{SRH} (blue curve) and R_L (red curve).

[9] In these expression the dependence on time has been neglected for simplicity. The carrier concentrations still depend on time and thus also R_L and R_{SRH} are time-dependent. Conversely, γ, τ and n_i are constant during the voltage decrease.

Looking at the expressions for R_L and R_{SRH} it is clear that if $n \cong n_i$, then $R_L(t)<R_{SRH}(t)$.

In order to make clear the difference in the recombination rates during the decay, Figure 4.7 shows the values of R_L and R_{SRH} as functions of the carrier concentration, calculated using the expressions written before. In figure, the red line represents the bimolecular recombination, the blue line is the trap-assisted recombination, while the black line is the recombination value due to both R_L and R_{SRH}. As already observed, at the beginning of the decay the carrier concentration is high. In this condition, the bimolecular recombination dominates over the trap-assisted recombination by several orders of magnitude ($R_L >> R_{SRH}$). Clearly, this situation corresponds to the first phase in the voltage decay. Conversely, towards the end of the decay (i.e., when the carrier concentration is small), the trap-assisted recombination dominates over the bimolecular recombination ($R_{SRH} >> R_L$), marking the second phase described above. By imposing $R_L=R_{SRH}$, it is possible to calculate the concentration value that marks the transition point between the two regions. This critical concentration is $n = \frac{1}{2\gamma\tau}$.

Depending on which of these two regions is considered, Equation (4.17) assumes two different forms. In particular, when the Langevin recombination is negligible with respect to the trap assisted one (final part of the decay phase), (4.17) becomes:

$$\frac{dn}{dt} = \frac{dp}{dt} = -\frac{n - n_i}{2\tau} \qquad (4.21)$$

The solution of this equation permits to calculate *n* during the last part of the OCVD decay phase:

$$n(t) = p(t) = \frac{1}{2\gamma\tau} e^{-\frac{t}{2\tau}} + n_i \qquad (4.22)$$

Equations (4.20) and (4.22) are two very important results. In fact, they allow to simulate the concentration decay in both phases of the voltage decay. From these equations it is also possible to simulate the voltage decay itself using (4.15).

Figure 4.8 summarizes the evolution of the voltage decay when the polaron pair concentration decay is neglected ($X(t)=0$ when t>0, i.e. the approximation made in 4.4.3). The red and blue lines simulate the V_{OC} decay in two limit cases:

- The red line is the voltage when only bimolecular recombination is considered, and it is plotted using (4.20) applied to (4.15).

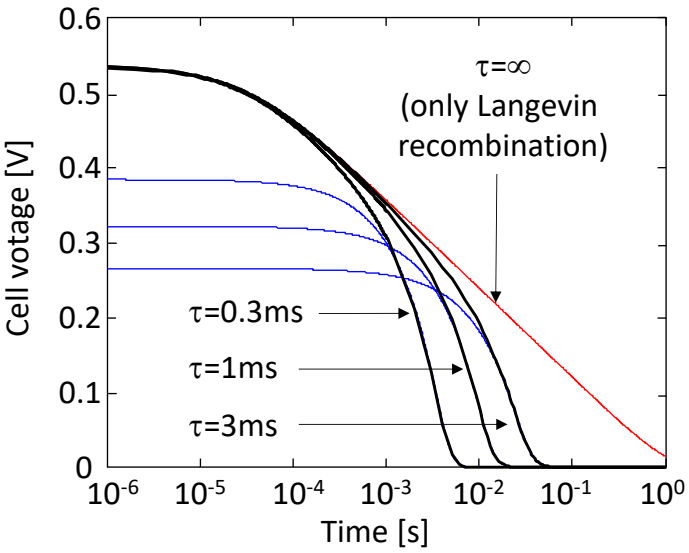

Figure 4.8 Simulation of the V_{OC} decay for three different values of τ. The red line is the voltage decay when the Langevin recombination is the dominant mechanism. The blue lines are the analytical approximation of the voltage decay when SRH is the dominant recombination mechanism.

- The blue lines are three simulations accounting only for trap assisted recombination, with τ=0.3ms, 1ms, 3ms. Equations (4.22) and (4.15) are used to plot this evolution.

Of course, the two evolutions are valid only in the regions where the respective approximation hold true (for the red lines the evolution is correct only in the initial part of the decay, while for the blue lines the evolution is correct only in the final part of the decay). This is confirmed by the black lines, which represent the voltage decay accounting for both bimolecular and trap assisted recombination.

Noticeably, during the first part of the decay, all the black curves tend to overlap each other because the voltage decay is dominated by the bimolecular recombination, as expected. Instead, during the second part of the decay, the black curves shift rightward with increasing τ, following the blue lines. This is also in agreement with what reported above: when the photogenerated carrier concentration becomes small enough (towards the end of the decay), the voltage decay is mostly influenced by the trap assisted recombination.

4.4.5 Parameters fitting

Fitting the experimental data with the model allows to obtain a good evaluation of the parameters that characterize the solar cell, as was done in 0. The fitting parameters of the model are those already described in this chapter: γ, n_i, τ, k_{REC}, k_{SEP}, G_{np0}. In order to extrapolate them, it is necessary to extrapolate some information from the J_{PH}-V measurements by means of the

photocurrent model. In the following, the procedure for the parameters extrapolation is described:

1. Fitting the J_{PH}-V measurement by means of the model developed in 0 it is possible to extrapolate G_X and P_{SEP}.
2. From G_X and P_{SEP} it is possible to calculate $G_{np0}=P_{SEP}G_X$, i.e. the carrier generation rate at the beginning of the voltage decay.
3. Once known G_{np0}, Equation (4.20) can be used in order to obtain n_i and γ, from the first region of the voltage decay (where Langevin recombination predominates). In fact, inverting (4.20):

$$\frac{n(t)}{n_i} = \operatorname{acoth}\left(\gamma n_i t + acoth\sqrt{\frac{G_{np0}}{\gamma n_i^2}+1}\right)$$

Inverting (4.15) with n(t)=p(t) and X(t)=0 as already supposed,

$$\frac{n(t)}{n_i} = \exp\left(\frac{V_{OC}(t)}{2V_T}\right) = \operatorname{acoth}\left(\gamma n_i t + acoth\sqrt{\frac{G_{np0}}{\gamma n_i^2}+1}\right) \qquad (4.23)$$

Thus,

$$\gamma n_i t + acoth\sqrt{\frac{G_{np0}}{\gamma n_i^2}+1} = \coth\left(exp\left(\frac{V_{OC}(t)}{2V_T}\right)\right)$$

The right hand can be easily calculated and plotted as function of time. The resulting curve can be fitted by means of a time-dependent straight line whose equation is described by the left term in the last equation. Clearly, its slope is equal γn_i, while the intercept is equal to $acoth\sqrt{\frac{G_{np0}}{\gamma n_i^2}+1} \cong acoth\sqrt{\frac{G_{np0}}{\gamma n_i^2}}$. From the knowledge of these two terms, it is possible to extrapolate γ and n_i.

4. Using the Braun-Onsager model, k_{SEP} can be extrapolated from γ (see 2.7.1) and, in turn, k_{REC} from k_{SEP} and P_{SEP} (see (4.10)).
5. Finally, τ is calculated from the transition point (1/2γτ) between the two parts of the voltage decay, i.e., where the decay slope changes (see 4.4.3).

For each step, the best fitting values can be calculated using a suitable numerical fitting procedure, for example the least squares regression.

4.4.6 Role of the geometric capacitance on the V_{OC} decay

One final note on the model is needed. One may think that the V_{OC} voltage decay may be due to the role of the geometric capacitance of the device (in fact, as said in the introduction, the

polymeric solar cell can also be seen as a Metal-Insulator-Metal system). If this were true, the voltage decay of the solar cell should decrease following the discharge of an RC circuit, where R is the resistance value associated to the active layer of the solar cell and C is the geometric capacitance. In order to prove that this is not true (at least for the devices analyzed in this work), in the following both the geometric capacitance and the resistance will be calculated.

In the device used, the active layer area is A=0.49cm^2, the dielectric constant is $\varepsilon = \varepsilon_0\varepsilon_r$ (ε_r=3) and the active layer thickness is d=275nm. Assuming the geometric capacitance as a parallel plate capacitor, its value should be $C=A\epsilon/d=4.8nF$.

From I-V measurements performed on the cells, it is possible to calculate the resistance value of the solar cell. These estimations give an RC constant of 2µs, which is a much smaller value than the value that characterize the decay time of the V_{OC}.

This simple analysis suggests that the interpretation given to the open circuit voltage decay in this Chapter is correct, and it is not strongly influenced by the presence of the geometric capacitance.

4.5 Model applications

The model presented so far can be used to fit the measured voltage decrease during OCVD. In order to explain which parameters of the solar cells can be extracted from the experimental data and to explain how these results can be used to gain information on the devices measured, OCVD was performed on a reference polymeric solar cell made of P3HT:PCBM. The OCVD model explained is applied to these measurements and, later in this Paragraph, some discussions will be done about the results obtained. In the next Chapter, the model will be analyzed to extrapolate parameters from many other devices (also fabricated of different polymers) and from stressed devices.

The structure of the cells used to obtain the results shown in this chapter is: glass/ITO/PEDOT:PSS/active layer/LiF/Al, and it is sketched in Figure 4.9). A standard P3HT:PC_{61}BM was used in the devices as active layer. The device will be referred to simply as P3HT.

4.5.1 Description of the device used

This part is focused on the analysis of a P3HT:PCBM solar cell. Before the analysis of the OCVD measurement on this device, some details about the fabrication will be given.

To build the solar cells, patterned ITO-coated glasses (10 Ohm/square resistance) were cleaned in sequential sonicating baths in deionized water, acetone, and isopropanol. After the

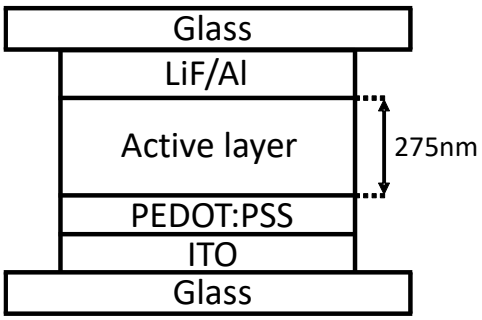

Figure 4.9 Cross section of the cells used in this work.

final sonication step, substrates were dried and then placed in an oxygen plasma chamber for 5 min. Next, a thin layer (50 nm) of PEDOT:PSS was deposited on the ITO surface (by blade-coating in air) and subsequently annealed at 150°C for 15 minutes. The active layer were prepared from solutions of P3HT:$PC_{61}BM$ dissolved in orthodichlorobenzene (ODCB) with a total concentration of 40 mg/mL and 30 mg/ml respectively. The active solutions were deposited by blade-coating under ambient conditions.

The processing conditions of the active layer was optimized in terms of Donor:Acceptor ratio, thickness, deposition temperature and speed, annealing, etc. The films were then transferred inside a metal evaporator for the deposition of the top electrode: LiF (0.6 nm) and Al (100nm). Finally, all devices were encapsulated, before characterization, inside the glove box in oxygen and moisture free environment.

4.5.2 OCVD model and experimental data from some stressed cells

Figure 4.10(a) and (b) show several voltage decreases during OCVD measurements (symbols) on the cell previously described. The two figures plot the same data, but the first highlights the presence of two different slopes, the second shows the quality of the fit (black solid lines). Each curve represents a measurement made during a procedure of electrical stress performed at -9V. For each curve, the measurement was done after the period of time indicated in figure. Noticeably, the curves are very similar to those simulated and shown in this chapter: for the fresh cell, the decay start at a voltage V_{OC}=*0.52V* and it is over after 0.01s. Two different slopes associated to bimolecular recombination and to trap assisted recombination can be observed, as highlighted in Figure 4.10(a). On the contrary, in Figure 4.10(b), superimposed to the symbols there are solid lines that represent the simulation obtained by means of the model presented in this Chapter.

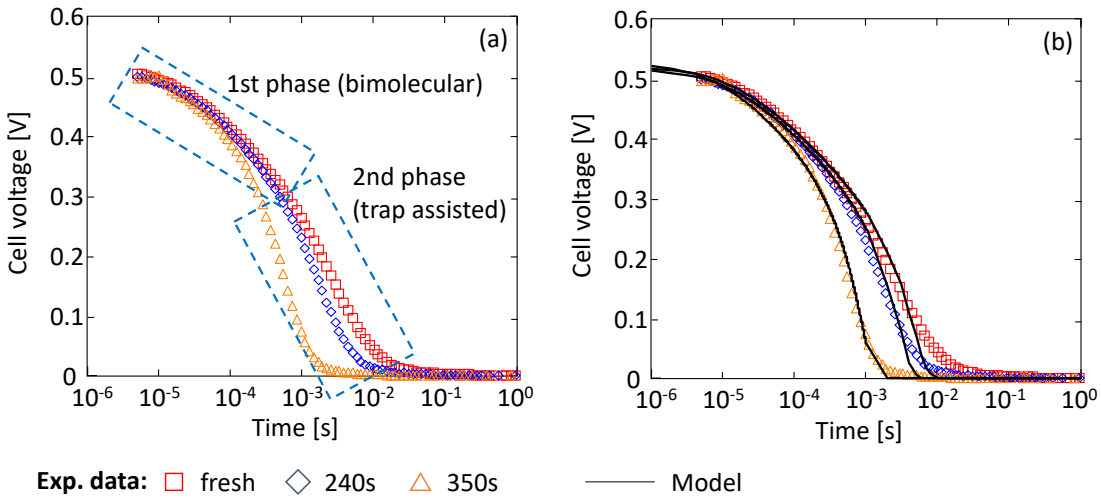

Figure 4.10 OCVD measurement results obtained in a P3HT cell. The measurements were made during an electrical stress performed at -9V. Both figures plot the same data, but (a) highlights the two slopes that characterize the voltage decay in semi-log scale axes. In (b) symbols are the experimental data and the lines are the model.

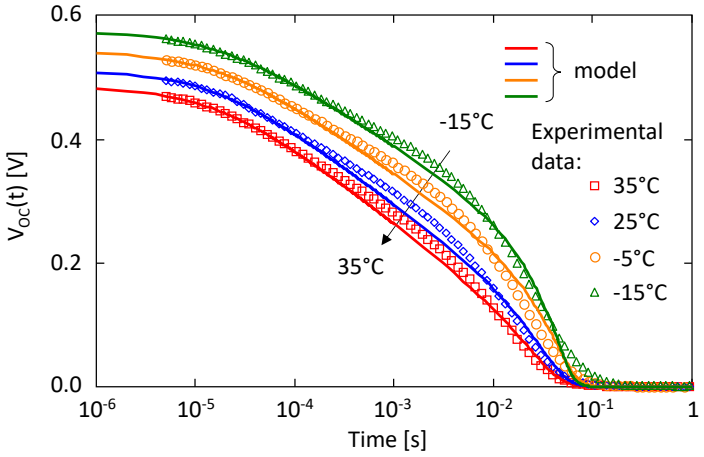

Figure 4.11 OCVD measurements obtained from P3HT:PCBM solar cell under different temperature conditions.

The data are excellently fitted for the most part of every curve, highlighting the important role of the recombination mechanisms that undergo inside the solar cell. Remarkably, the fit during the second phase of the OCVD was obtained neglecting the presence of excitons and assuming that the polaron pairs concentration *X* vanishes during the initial part of the decay. Besides, it is assumed that no doping is present inside the active layer to fit the curves.

The two slopes in the voltage decay are clearly visible, and they become even more evident during the stress procedure. From the analysis of the curves during electrical stress it can be inferred that the electrical stress has the effect to accelerate the recombination process of the charges inside the active layer. This is confirmed by the fact that the decays become faster during the stress procedure. Remarkably, after 350s of -9V electrical stress, the voltage decay has become 1000 times faster. By extrapolating the parameters that characterize the solar cell, more

information can be obtained regarding the internal condition of the device. This topic will be the main argument of the next chapter.

Figure 4.11 shows several voltage decays obtained in a P3HT:PCBM solar cell. Each curve corresponds to a measurement performed under different temperature conditions (from -15°C to 35°C). From the curves, the effect of temperature on the voltage decay can be observed. In fact, a low temperature reflects on a downward shift of the curve, which shows a lower voltage and a lower initial open circuit voltage.

Applying the procedure described in 4.4.5 on the experimental data shown in Figure 4.11, the intrinsic carrier concentrations n_i can be extracted. The values of n_i for two representative devices are shown in the Arrhenius plot of Figure 4.12. From this plot it is possible to extrapolate the Energy Gap that characterizes the active layer of the solar cell. The extrapolated data reported in Figure 4.12 can be fitted by a straight line, which corresponds to the logarithm of the following equation:

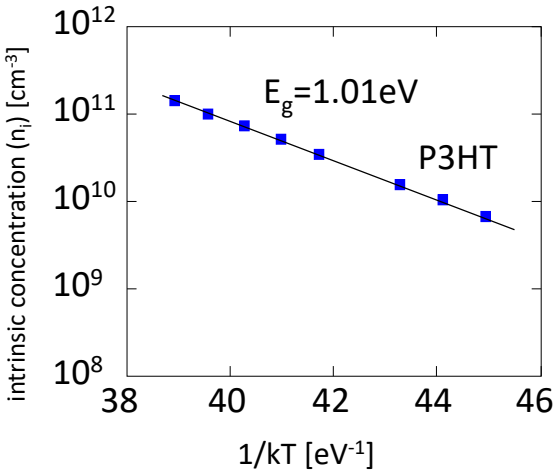

Figure 4.12 Arrhenius plot of the intrinsic carrier concentrations for P3HT fresh cell.

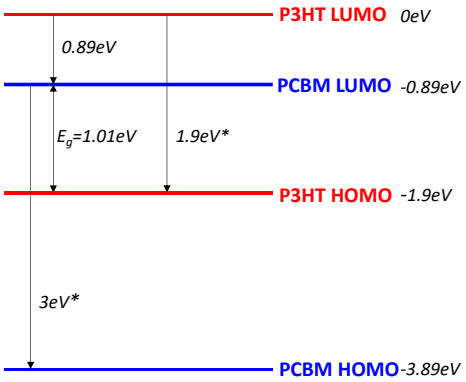

Figure 4.13 Band alignment of P3HT:PCBM blend calculated by means of the model and the Energy Gaps reported in [Ism15]. The energy values on the right are referred to the P3HT LUMO.

$$n_i = N_C \exp\left(-\frac{E_g}{2V_t}\right) \qquad (4.24)$$

Thus, from the slope of the straight line, it is possible to extrapolate the value of the Energy Gap. The P3HT cell has an Energy Gap of 1.01eV.

Figure 4.13 shows the band alignment of the P3HT:PCBM blend. The Energy Gap values are taken from the data reported in [Ism15].

4.6 Conclusions

In this Chapter a new model capable of fitting the open circuit voltage decay in polymeric solar cells was developed. This model takes into account the effects of two recombination mechanisms to fit the voltage decay exhibited by the solar cell: the bimolecular Langevin recombination and the trap assisted recombination. In addition, it includes the effects of the polaron pairs recombination and separation at the acceptor/donor interface. The model allows to extrapolate information about the bimolecular recombination coefficient, the carrier lifetime and the intrinsic carrier concentration. Moreover, it is possible to extract the value of the energy gap of the blend from pure electrical, non-invasive measurement. The model was validated on a solar cell with an active layer made of P3HT:$PC_{61}BM$.

In the next Chapter, the model will be used on a higher number of solar cells. The cells will be made of active layer materials different from the standard P3HT:PCBM. Furthermore, the effects of the electrical and thermal stresses on OCVD will be further analyzed.

4.7 References

[Alt11] S. Altazin, R. Clerc, R. Gwoziecki, G. Pananakakis, G. Ghibaudo, C. Serbutoviez, “Analytical modeling of organic solar cells and photodiodes”, Appl. Phys., Vol. 99, p. 143301, Oct. 2011.

[Bet06] R. De Bettignies, J. Leroy, M. Firon, C. Sentein, “Accelerated lifetime measurements of P3HT:PCBM solar cells”, Synth. Met., Vol. 156, p. 510–513, 2006.

[Bra84] C. L. Braun, “Electric field assisted dissociation of charge transfer states as a mechanism of photocarrier production”, J. Chem. Phys., Vol. 80, n. 9, pp. 4157–4161, 1984.

[Ces15] A. Cester, A. Rizzo, A. Bazzega, N. Lago, J. Favaro, M. Barbato, N. Wrachien, S.A. Gevorgyan, M. Corazza, F.C. Krebs, “Effects of constant voltage and constant current stress in PCBM: P3HT solar cells". Microelectronics Reliability, Vol. 55, n. 9-10, p. 1795-1799, 2015.

[Dam12] H. F. Dam and F. C. Krebs, “Simple roll coater with variable coating and temperature control for printed polymer solar cells” Sol. Energy Mater. Sol. Cells, vol. 97, p. 191–196, 2012.

[Hau08] J.A. Hauch, P. Schilinsky, S.A. Choulis, R. Childers, M. Biele, C.J. Brabec, “Flexible organic P3HT:PCBM bulk-heterojunction modules with more than 1 year outdoor lifetime”, Sol. Energy Mater. Sol. Cells, Vol. 92, p. 727–731, 2008.

[Ism15] Y. A. M. Ismail, T. Soga, and T. Jimbo, “Effect of Composition on Conjugation Structure and Energy Gap of P3HT:PCBM Organic Solar Cell”, Int. J. New. Hor. Phys., Vol. 2, p. 87-93, 2015.

[Jor08] M. Jorgensen, K. Norrman, and F.C. Krebs, “Stability/degradation of polymer solar cells”, Sol. Energy Mater. Sol. Cells, Vol. 92, pp. 686-714, 2008.

[Kui11] M. Kuik, L. J. A. Koster, G. A. H. Wetzelaer, and P. W. M. Blom, “Trap-Assisted Recombination in Disordered Organic Semiconductors”, Phys. Rev. Lett., Vol. 107, p. 256805, 2011.

[Llan03] P. Langevin, Ann. “Recombination and ion mobility in gases”, Chim. Phys., Vol. 28, p. 433, 1903.

[Mad14] M. V. Madsen, S. A. Gevorgyan, R. Pacios, J. Ajuria, I. Etxebarria, J. Kettle, N. D. Bristow, M. Neophytou, S. A. Choulis, L. S. Roman, T.Yohannes, A. Cester, et al., "Worldwide outdoor round robin study of organic photovoltaic devices and modules", Sol. Energy Mater. Sol. Cells, Vol. 130, p. 281-290, 2014.

[Ons38] L. Onsager, “Initial recombination of ions,” Phys. Rev., vol. 54, n. 8, pp. 554–557, Oct. 1938.

[Ooi08] Z. E. Ooi, T. L. Tam, A. sellinger and J. C. deMello, “Field-dependent carrier generation in bulk heterojunction solar cells”, Energy & Environ. Sci., Vol. 1, p. 300-309, May 2008.

[Rip12] T. Ripolles-Sanchis, A. Guerrero, J. Bisquert, G. Garcia-Belmonte, “Diffusion-recombination determines collected current and voltage in polymer:fullerene solar cells”, J. Phys. Chem. C, Vol. 116, p. 16925–16933, 2012.

[Riz16] A. Rizzo, A. Cester, N. Wrachien, N. Lago, L. Torto, M. Barbato, J. Favaro, S. A. Gevorgyan, M. Corazza, F. C. Krebs “Characterization and modeling of organic (P3HT:PCBM) solar cells as a function of bias and illumination”, Sol. Energy Mater. Sol. Cells, Vol. 157, p. 337-345, 2016.

[Sok82] R. Sokel and Hughes “Numerical analysis of transient photoconductivity in insulators”, J. Appl. Phys., Vol. 53, n. 11, p. 7414, Nov. 1982.

[Spa04] H. Spanggaard, F. C. Krebs, “A brief history of the development of organic and polymeric photovoltaics”, Sol. Energy Mater. Sol. Cells, vol. 83, p. 125-146, June 2004

[Tor16] L. Torto, A. Cester, A. Rizzo, N. Wrachien, S. A. Gevorgyan, M. Corazza, and F. C. Krebs, “Model of organic solar cell photocurrent including the effect of charge accumulation at interfaces and non-uniform carrier generation”, IEEE Journal of the Electron Devices Society, Vol. 4 p. 387-395, 2016.

[Vor11] E. Voroshazi, B. Verreet, T. Aernouts, P. Heremans, “Long-term operational lifetime and degradation analysis of P3HT:PCBM photovoltaic cells”, Sol. Energy Mater. Sol. Cells, Vol. 95, p. 1303–1307, 2011.

[Zab03] A. Zaban, M. Greenshtein, and J. Bisquert, “Determination of the Electron Lifetime in Nanocrystalline Dye Solar Cells by Open-Circuit Voltage Decay Measurements”, Chem. Phys. Chem., Vol. 4, p. 859–864, August 18, 2003.

Chapter 5 Experimental applications of the OCVD model

5.1 Introduction

The Open Circuit Voltage Decay model described in Chapter 4 has already been applied to some experimental results obtained from a reference device in order to highlight some potentiality of the model. This is only a glimpse of the results that can be achieved, and in this chapter the experimental data will be further analyzed, extrapolating more parameters and discussing them. In some cases, the analysis of the solar cells will be supported by the photocurrent model described in Chapter 3. This will allow to extrapolate more information about the working principle of the solar cells, and to understand which characteristics majorly affects their functionalities.

Two main groups of solar devices will be analyzed separately.

The analyzed cells of the first group are made of four different polymers, and each of them shows peculiar characteristics (be them the different V_{OC} voltage, or the different reaction to stress solicitations). Their structure is identical to the structure of the reference cell described in 4.5.1 (apart, of course, the material of the blend). The analysis will be performed using OCVD measurements and the photocurrent model, both on fresh cells and on degraded cells, and both at room temperature and imposed temperature.

Also the second group has been analyzed using both the photocurrent model presented in Chapter 3 and the OCVD model. The active layer of these devices is always made of P3HT:PCBM, and the structure is slightly different from the previous set. The analysis will be focused on the

results obtained after some stress procedures, and they will be measured at different temperatures.

The information extracted using the model will be correlated with the conventional figures of merit that are usually considered to describe the performances of a solar cell (Fill Factor, Efficiency, etc.).

The J-V and OCVD measurements are performed by means of a custom acquisition board, which permits to control simultaneously the LED switching and the voltage sampling. Furthermore, in contrast to the common oscilloscopes, the board permits to use a logarithmic sampling time spacing, in order to combine: i) a fast sampling at the beginning of the transient (i.e. when the voltage decay is fast); ii) a larger sampling time during the final part of the transient (i.e. when the voltage decay is slower). In this way, a long transient can be monitored limiting the number of samples without loss of data in the first part of the decay.

Light is generated using a White LED illuminator. To take into account the different spectrum of the white LED with respect to the solar spectrum, the LED intensity is calibrated in order to achieve the same short circuit current calculated from the EQE measurements under 1 Sun illumination.

5.2 Device description

The first group of devices used are conventional bulk heterojunction OSCs, with the same structure reported in 4.5.1. The only difference is that the active layer is not always P3HT:PCBM anymore, but it is made of more different donor polymers. For this reason, the devices will be divided into four groups, one for each donor polymer that is used in the active layer. Three of these are innovative materials, featuring a band gap wider than 1.7eV, and they are called PFQBDT-TR_1, P(1)-PFQ2T-BDT and DA147. For simplicity, they will be referenced here as P1, P2 and P3, respectively. Of course, the fourth donor material is the standard P3HT, which is used as reference (as done in the previous chapter). Each polymer was opportunely blended with the acceptor material ($PC_{61}BM$) to form the active layer of the solar cells. From now one, each cell will be identified with the name of its donor polymer. For example, the cell made with a P1:PCBM active layer will be named simply P1.

These organic solar cells that were fabricated at the Consiglio Nazionale Ricerche (CNR) in Bologna (Italy).

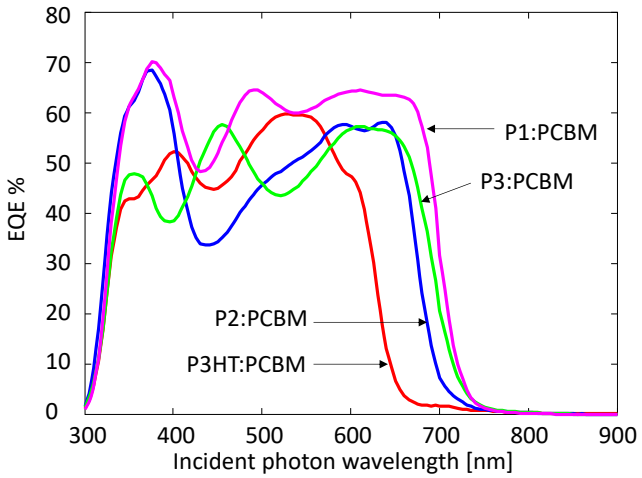

Figure 5.1 External Quantum Efficiency characteristics measured in four representative solar cells featuring $PC_{61}BM$ as acceptor and four different polymers as donor materials.

Cell	η [%]	FF [%]	V_{OC} [V]	J_{SC} [mA/cm^2]
P3HT	3.4	70.8	0.6	8
P1	4.9	61.5	0.846	10.4
P2	5.1	67.4	0.868	9.5
P3	4.1	54.9	0.889	9.5

Table 8 Figures of merit (the values are the mean of the values extrapolated from several solar cells)

5.3 Characterization of four different polymers

5.3.1 Generic parameters of the solar cells

To give a general presentation of the organic solar cells used, Table 8 summarizes the figures of merit of the cells used, calculated as described in 2.4.3. Each value is a mean of the values extrapolated from conventional J-V measurements.

J_{SC} and V_{OC} are both larger in P1, P2 and P3 with respect to P3HT. The efficiencies η in P1, P2 and P3 are than P3HT, and this is mostly related to the smaller V_{OC} of P3HT. On the contrary, P3HT features the best fill factor (*FF=70.8%*).

Figure 5.1 shows the external quantum efficiency (EQE) for each device as a function of the incident photon wavelength. P1, P2 and P3 feature the widest absorption spectra, which range from 300nm to approximately 720nm, with only marginal variations among the three polymers. In turn, P3HT has a narrower absorption interval, which ranges from 300nm to 660nm, explaining its smaller short circuit current.

Figure 5.2 shows the photocurrent densities J_{PH} of the four devices. Under strong reverse bias (i.e. for voltages lower than -1V), P3 shows the highest photocurrent among the four devices. Conversely P3HT, at the same conditions, generates the lowest current.

Figure 5.2 shows that P3 has a stronger dependence on the electric field with respect to P1, P2 and P3HT, indicating the smaller separation probability of P3, as suggested by the Sokel model. In fact, the photocurrent under strong reverse bias depends on the carrier generation rate and on P_{SEP}: if P_{SEP} were 100%, according to the ideal Sokel model [Sok82] the photocurrent should be almost constant in reverse bias conditions.

From the photocurrent in the reverse bias condition, the generation G_{np} and the separation probability P_{SEP} were calculated, as reported in [Riz16a]. In Figure 5.3(a) is shown a comparison between the polaron pairs separation probability of the four samples. Each P_{SEP} was calculated at 25°C and $V=V_{OC}$. Moreover, in the histogram of Figure 5.3(b), the values of G and the

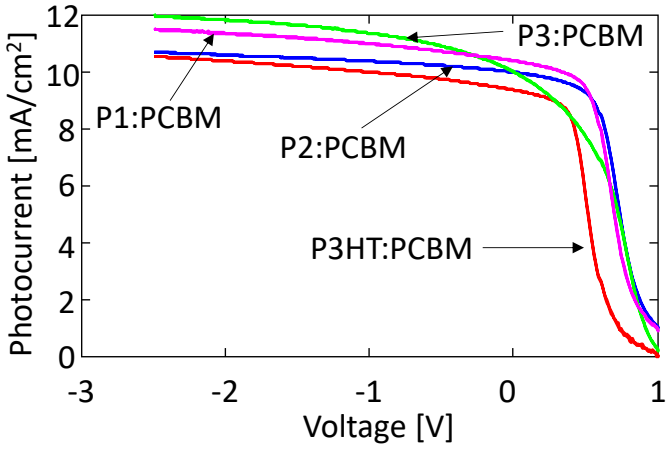

Figure 5.2 Photocurrent density vs. voltage characteristics taken in four OSCs featuring $PC_{61}BM$ as acceptor and four different polymers as donor materials.

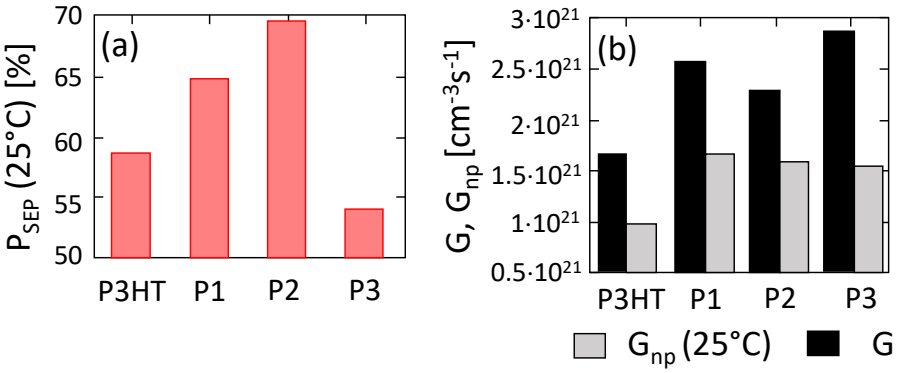

Figure 5.3 a) Separation probability at 25°C and $V=V_{OC}$ for the four different polymers used in this work. For each polymer is shown the average value over 6 nominally identical samples. b) Polaron pairs generation (G) and free carrier generation ($G_{np} = P_{SEP}$ G) for the same samples of Fig. a.

product G_{np}, was calculated for each device at 25°C. The highest values of the carrier generation G_{np} are associated to P1, P2 and P3 and they are very close to each other. In fact, for P1, P2, and P3, $G_{np} = 1.5 \cdot 10^{21} cm^{-3} s^{-1}$, while for P3HT, $G_{np} = 10^{21} cm^{-3} s^{-1}$. The low separation probability that characterizes P3 is well compensated by the large polaron pair generation G, which is the highest among all the devices.

This difference in the polaron pairs and carriers generation rate (G and G_{np}, respectively) of the P3HT cell is partially correlated to its narrower absorption spectrum. In fact, having a small exciton generation rate, the solar cell can produce fewer polaron pairs and thus fewer free carriers. Remarkably, despite G_{np} is almost the same for P1, P2 and P3, P3 has a lower efficiency (4.1%) than P1 and P2 (4.9% and 5.1%, respectively, see Table 8). This is related to the non-ideal photocurrent shape, which reduces its FF.

An important observation (that will lead to some considerations later) can be made observing the photocurrent plot. In P1 and P2 cells, the photocurrent does not become negative, but it tends to zero at relatively low forward voltages (i.e. up to 1V, which is a reasonable region to prevent voltage-induced damage). The same behavior is observed in all the devices with a P1 or P2 active layer analyzed for this work. This cannot be said for the P3HT cells, which tend to reach a negative photocurrent value even before reaching 1V bias. This will be further discussed in 5.3.2.

5.3.2 Considerations regarding photocurrent

As already noticed, in the photocurrents plotted in Figure 5.2 there are two main differences between the cell types.

The first difference regards the photocurrents behaviors, which never become negative for the cells P1, P2 and P3, at least for the voltage ranges used. Conversely, the photocurrent produced by P3HT cell becomes negative when it reaches 1V.

This suggests that P1, P2 and P3 cells feature one blocking contact. In fact, because the cathode is metallic, the interfaces with PEDOT:PSS should block the electrons due to the differences in the respective LUMO values. Thus, the LUMO of the PEDOT:PSS could act as an electron barrier.

To confirm this idea, the photocurrent model proposed by Sokel [Sok82] can be modified in order to take into account also of the blocking contact.

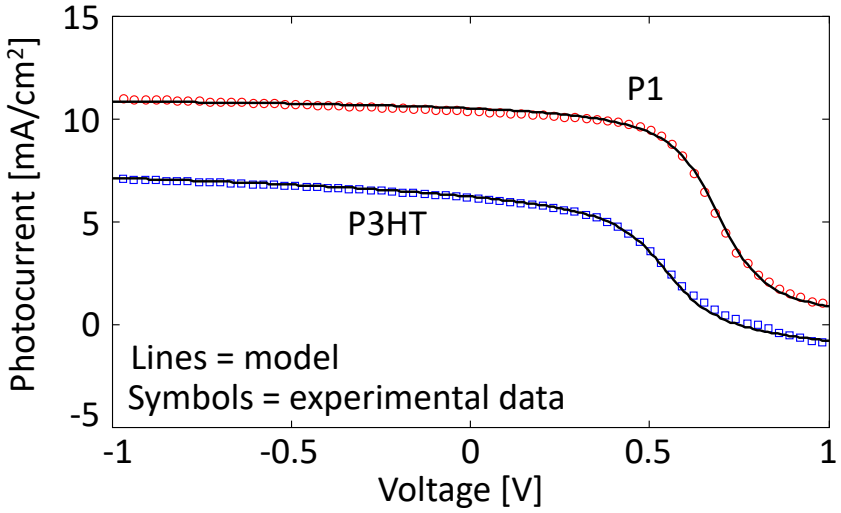

Figure 5.4 Photocurrent plot for a P3HT cell and a P1 cell. Symbols are the experimental data, solid lines are the model.

In fact, the original Sokel approach solves the carrier continuity equation assuming that recombination is negligible, that the contacts are metallic and that they can extract all the carriers (see Chapter 3). As a consequence, the concentrations of free carriers at the cell boundaries are zero, which is the assumption that is in contrast with the results of the OCVD model. In order to include also this effect, the continuity equation for the carrier density was solved assuming the cathode a metallic contact, and the anode an ideal electron blocking contact (i.e. the same situation of the devices analyzed). With these assumptions, the electron concentration is zero at the cathode and the electron current is zero at the anode. The equation for the photocurrent obtained using this version of the model is:

$$J_{PH} = \left(\frac{qG_X L}{2} + \frac{qG_X L}{2}\left[\coth\left(\frac{V_{BI}-V}{2V_T}\right) - \frac{2V_T}{V_{BI}-V}\right]\right)\cdot P_{SEP} \qquad (5.1)$$

Equation (5.1) is composed of two main terms: the first accounts for the current due to the electrons, the second is related to the hole contribution on the photocurrent. This term is not constant and it is similar to the photocurrent expression given in Chapter 3.

In order to better highlight the differences in the degradation of one of the materials considered in this work and the reference device, In Figure 5.4 two photocurrent plots are reported for both P1 and P3HT. The blocking contact photocurrent model excellently fits P1 experimental data (solid lines), confirming the presence of a selective contact at the anode. Conversely, P3HT cells do not feature a perfect selective contact, and the model presented in 0 was used to fit the data of Figure 5.4 to extrapolate information about P3HT active layer.

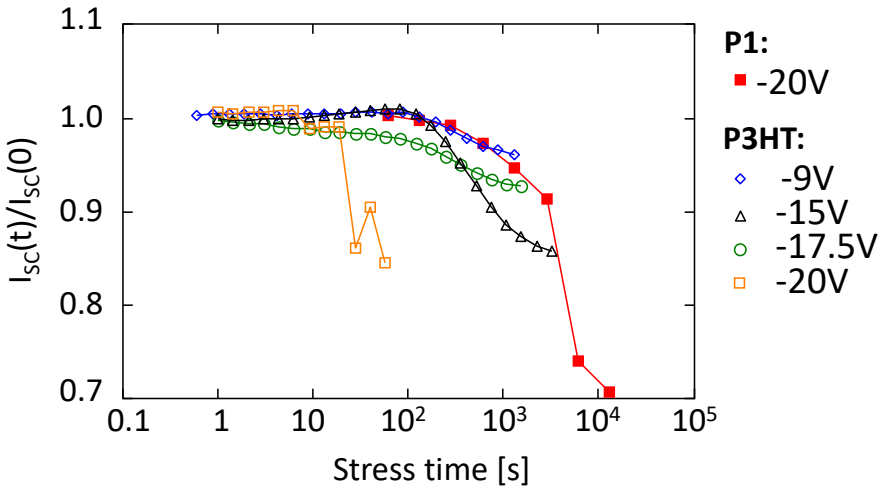

Figure 5.5 I_{SC} degradation kinetics during different electrical stress performed at various stress voltages.

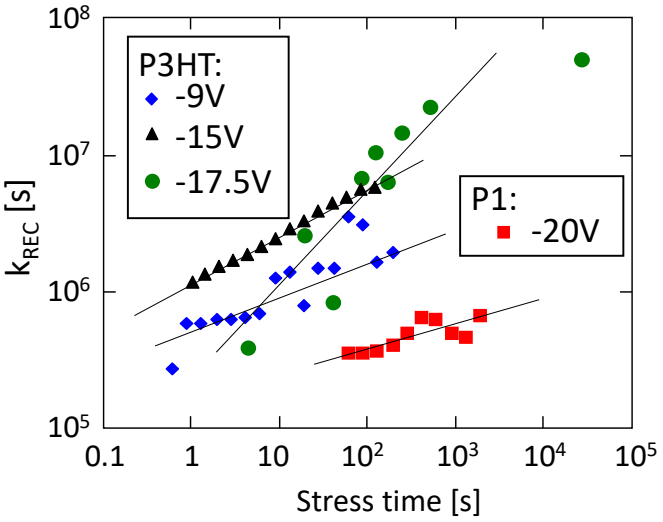

Figure 5.6 Recombination rate k_{REC} during electrical stress for P1 cells and P3HT cells. The voltage applied to the devices during stresses are reported in the legends.

Figure 5.5 shows the variation of the short circuit current density (I_{SC}) during a constant reverse voltage stress for both P1 and P3HT solar cells. The stress was performed at four different voltages for P3HT, and at -20V for P1. P1 does not show heavy degradation in I_{SC} until about 10^4s, and a similar behavior is associated to the P3HT cells stressed at a -9V, -15V and -17.5V, which show the same I_{SC} variation. Instead, the P3HT cells stressed at -20V present an I_{SC} kinetics which degrades much faster. In particular, the cells undergo a sudden breakdown after 20s. This highlights the better stability of P1 if compared to P3HT, which degrades faster.

Figure 5.6 shows the value of k_{REC}, calculated by means of the photocurrent model (for both P3HT cell and P1 cell). This is in agreement with what observed in Figure 5.5, where the short circuit current decreases during stress is shown.

P3HT - Various temperatures

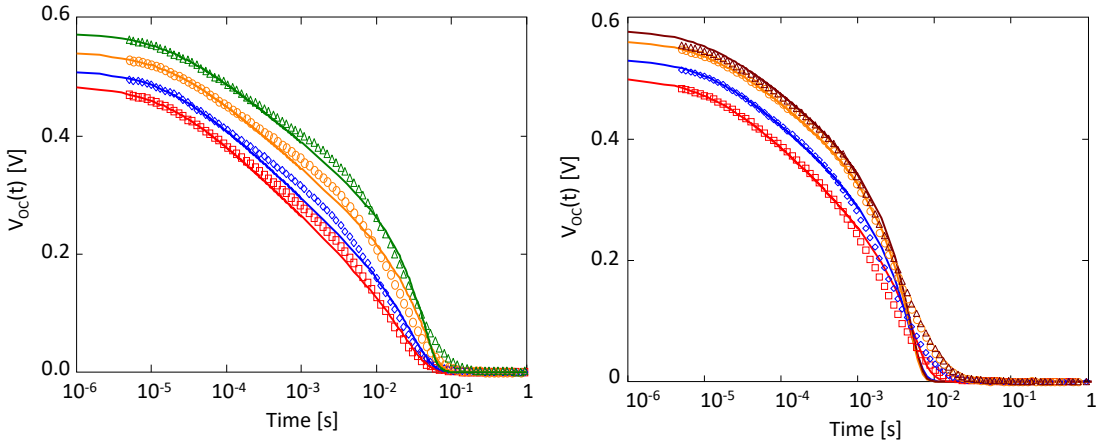

P1 - Various temperatures

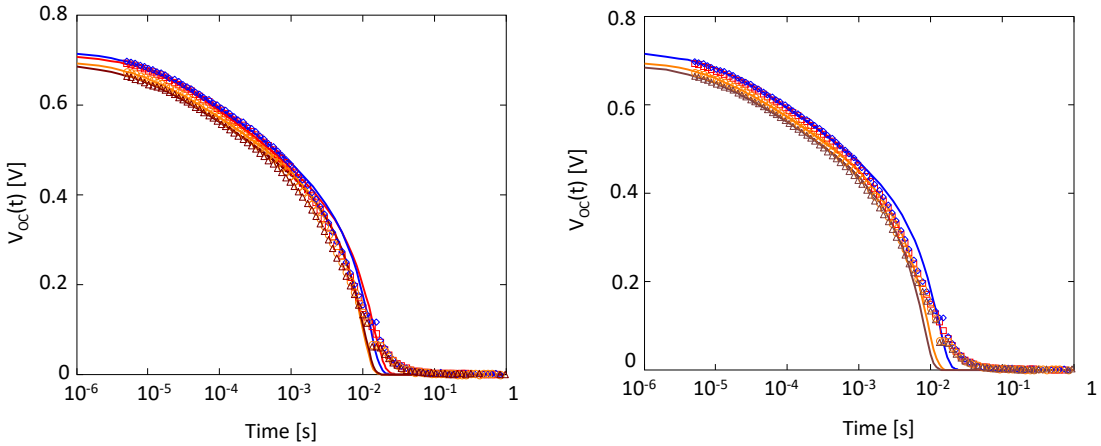

P2 - Various temperatures

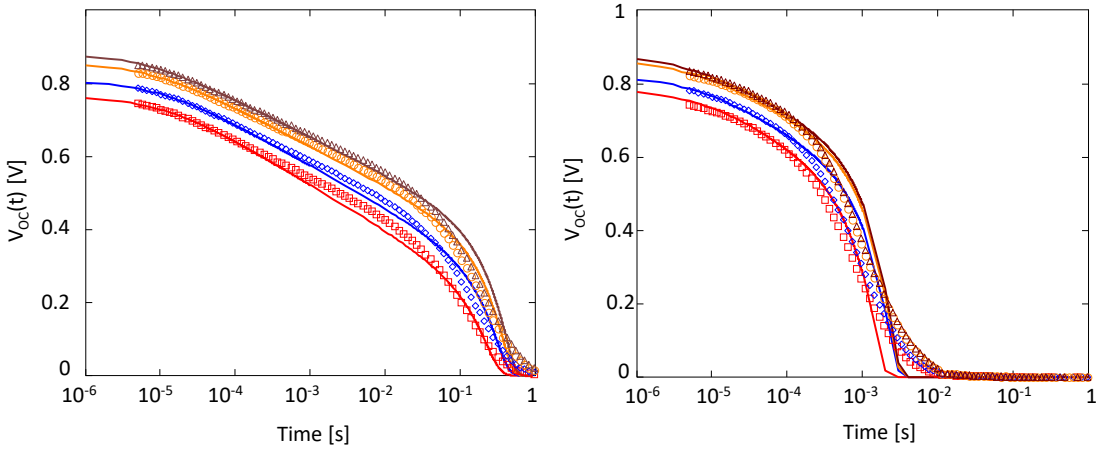

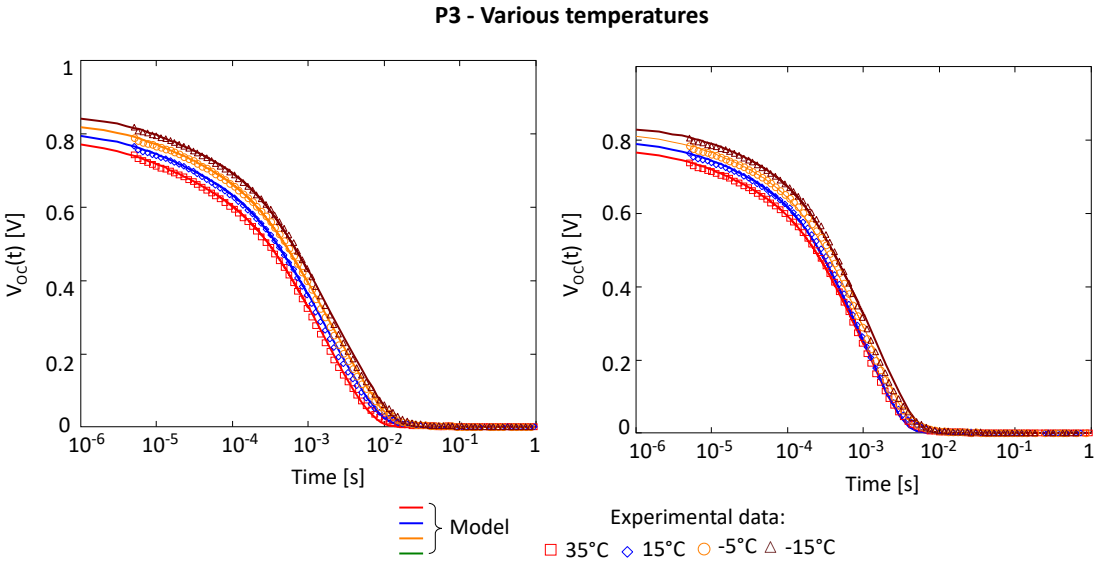

Figure 5.7 Several OCVD measurements made in different solar cells, as indicated above each figure. Each curve corresponds to a temperature value (as indicated in the legend). Temperatures vary from -15°C to 35°C. Symbols are the experimental data and the lines are the model described in Chapter 4.

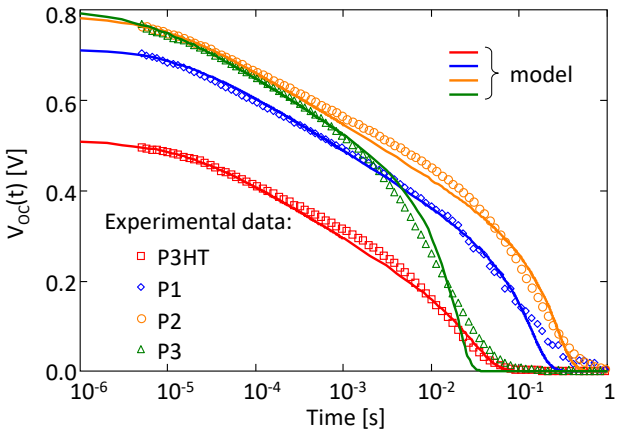

Figure 5.8 OCVD measured obtained from P3HT, P1, P2 and P3 devices at 25°C. Symbols are the experimental data and the lines are the model described in Chapter 4.

The second important difference in the photocurrent plots of Figure 5.4 is the higher current produced by P1 cells, suggesting a better initial performances of these devices with respect to the P3HT cells. Besides, the degradation of the P3HT cells is much faster and it occurs in much shorter time. This is made clear in Figure 5.6: clearly, the I_{SC} of the P3HT cells stressed at -9V overlaps the P1 I_{SC} degradation kinetics during stress at -20V. Conversely, if the P3HT cells are stressed at -20V, a sudden breakdown occurs after 20s, i.e., one hundred times faster than in P1. In summary, not only the P1 cells have an initial I_{SC} larger than that of P3HT, but the P1 cell degradation is much slower. This suggests a better stability of the P1 cells, and also a better generation capability. This trend can also be observed in the transient measurements Figure 5.7.

Cell	γ [cm^3s^{-1}]	E_g [eV]	Donor polymer E_g [eV]
P3HT	$4.7 \cdot 10^{-12}$	1.13	1.91
P1	$7.5 \cdot 10^{-12}$	1.405	1.728
P2	$8.5 \cdot 10^{-12}$	1.41	1.78
P3	$38 \cdot 10^{-12}$	1.49	1.727

Table 9 Model parameters

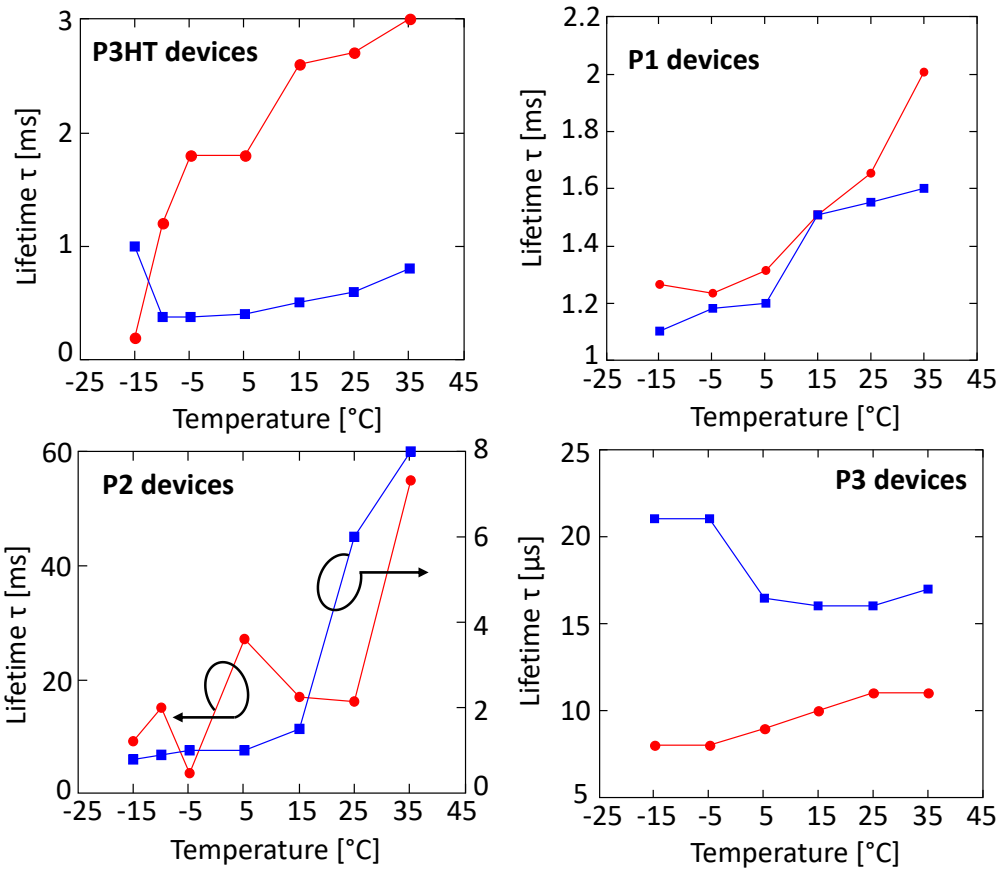

Figure 5.9 Lifetime values during the second part of the voltage decay. Each plot shows the variations of the lifetime extrapolated from the voltage decays reported in Figure 5.7. The values for P2 has two different scales, while the values reported for P3 are expressed in µs (not in ms like in the other plots).

5.3.3 Voltage decay analysis

By using only these parameters, it would not be possible to determine the cause behind the different performance of the four devices, in particular among P1, P2 and P3. In order to do this, it is necessary to consider the OCVD measurements and the results of the model applied to OCVDs. In fact, as described in Chapter 4, the proposed model is able to provide information about the recombination mechanisms inside the active layer. As it will be discussed in the following, this permits to understand the reasons of the reduced performance of P3 compared to P1 and P2.

In order to further analyze the polymeric cells, some OCVD measurements will be shown for different solar cells in Figure 5.4. In particular, the voltage decay of two sample devices for each type of active layer will be shown. Each measurement was made keeping the sample at a precise temperature, as indicated in the legend of the figure (each color and symbol corresponds to a different temperature). Superimposed to the symbols (which represent the experimental data) there are solid lines, that show the fit obtained by means of the model.

All the voltage decays are similar to each another. In particular, the two slopes associated to the different recombination regimes can be observed in every case. Some differences arise on the voltage decays shown by the two samples of the P2 cells. The main difference is on the duration of the decay, in one case very long and in one case very short. This is ascribed to a different lifetime values of the carriers inside the active layers, which recombine at a lower rate in the first case. Temperature acts differently on the vertical shift of the curves: P3HT is the cell that is most affected by the change in temperature, while P1 is almost unchanged in the whole temperature range.

The quality of the fit is good for all the solar devices, especially for the fit made on P3 cells. Noticeably, the fit is not accurate during the second part of the decay, even if the shape of the solid lines representing the fit follows the experimental data with an acceptable approximation. This fit is good when it is needed a fast estimation of the parameters involved in cell. In order to improve the quality of the fit, though, it is necessary to introduce some changes in the initial hypotheses of the model. These changes will be taken into consideration in Chapter 6, considering the non-constant distribution of charges inside the active layer during the decay.

Figure 5.8 compares the OCVDs obtained from P1, P2, P3 and P3HT cells, each performed at 25°C. The comparison confirms what discussed above, and it highlights that the decays start at different voltages that characterize the solar cell (the initial V_{OC} values are similar to those reported in Table 8).

Thanks to the fit made on several solar cells, the characterizing parameters of the solar cells were extracted. This was done by means of an automatic fit procedure that uses the least squares regression. The procedure extrapolates:

- The Langevin recombination constant γ and the intrinsic carrier concentration n_i from the first part of the OCVD;
- The carrier lifetime τ from the second part of the OCVD.

The typical values of the extracted parameters are listed for each polymer in Table 9. The extrapolated lifetimes τ from the OCVD shown above are reported in Figure 5.9 as functions of temperature.

As already observed in Chapter 4, γ heaviest impacts on the device behavior when the concentration of the photogenerated charges is high. On the contrary, τ is related to the V_{OC} decay when the concentration becomes low (i.e. when the V_{OC} transient is almost over), thus a low value of τ causes a faster decrease in the final part of the OCVD, as also noticed before.

In an organic semiconductor, this may be related to the high number of trapped carriers which may act as trapping centers for the opposite carriers. Both model and experimental data are in agreement with this prediction. In fact, the plots in Figure 5.9 indicate that, if the temperature decreases, τ also decreases. Correspondingly, V_{OC} decay becomes faster during the second part of the decay. Because in an organic semiconductor most of the carriers reside in tail state or in deep gap states, this behavior might be explained assuming that with increasing temperature, part of the carriers are freed from their traps. This translates into a reduction of the trapped carriers and, in turn, to an increase in the number of free trapping centers for the opposite carriers.

Comparing the three similar polymers P1, P2, and P3, the smaller efficiency and FF of P3 can be related to the larger recombination rate. P3 is indeed characterized by the highest γ of all the devices, leading to a higher recombination rate of the generated charges and to a subsequent reduction of the efficiency.

The values reported in Table 9 show that P3 has an efficiency smaller than P1 and P2. This device is also characterized by the lowest carrier lifetime ($\tau < 1ms$). Lifetime is indeed the main responsible for the fastest OCVD decay among the measured devices (as can be observed in Figure 5.8, where the V_{OC} decay is faster than the V_{OC} decay of the other cells). Incidentally, P3 is also the device with the lowest separation probability (as observed describing Figure 5.2). These facts may are in close relation. In fact, the presence of many defects (short lifetime τ) could enhance the polaron pair recombination, leading to a more difficult separation: thus it is reasonable to think that, if τ decreases, P_{SEP} also decreases. A low P_{SEP} has the effect of further reducing the fill factor, modifying the shape of the photocurrent near V_{OC} (see 0 and [Tor16]).

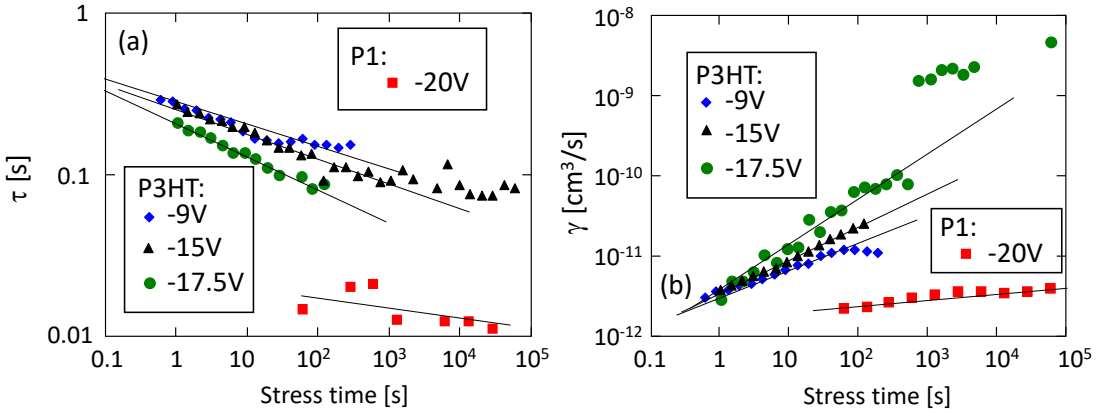

Figure 5.10 (a) Lifetime τ during electrical stress for P1 cells and P3HT cells. (b) Bimolecular recombination coefficient γ during electrical stress for P1 cells and P3HT cells.

τ and k_{REC} are useful also to monitor the degradation of a solar cell. Taking into consideration the stresses made on the P1 and P3HT polymeric solar cells discussed in 5.3.2, some observations can be made.

Figure 5.10(a) shows the variations of the lifetime τ for different devices during each stress step (each colors identify a different stress voltage). τ is extrapolated using the OCVD model, and a decreasing behavior can be observed in all the measurements made. Noticeably, τ in the P1 cells is smaller than τ in the P3HT cells, suggesting the presence of more defects in the P1 cells with respect to those present in the P3HT cells. However, τ in P1 cells slowly decreases during the stress at -20V. On the contrary, τ in P3HT cells undergoes a significant change: the stress performed at -17.5V is responsible for the highest degradation of τ if compared to the stresses performed at -15V and -9V. This is due to a faster formation of defects at higher stress voltages. Once again, this is agreement with the degradation behavior exhibited by the photocurrent. In fact, despite the P3HT is stressed at lower voltages than P1, the degradation of τ is much faster.

Thanks to the OCVD model, it is also possible to calculate γ during each stress step. In Figure 5.10(b) is reported its variation as a function of the stress time. The P1 cells are affected by a slight increase in γ during stress, meaning that the stress has a minor impact in the bimolecular recombination in the P1:$PC_{61}BM$ layer. Conversely, the P3HT cells are affected by a large increase in γ: during stress, the Langevin recombination limits more and more the lifetime of the free carriers. This reflects in a smaller number of free carriers and, in turn, on a lower photocurrent produced by the cell.

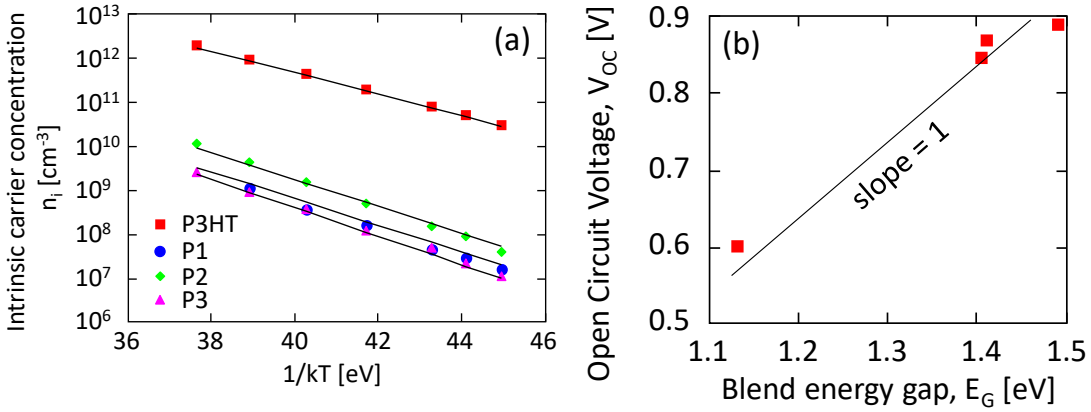

Figure 5.11 (a) Arrhenius plot of the intrinsic carrier concentrations for P3HT, P1, P2, and P3 devices. The slope of the straight lines identifies the energy gap of the blend (difference between the acceptor LUMO and donor HOMO). (b) Correlation plot of the equivalent energy gap of the blend and the open circuit voltage. The straight line represents the equation $V_{OC} = \frac{E_g}{q} - 0.55V$

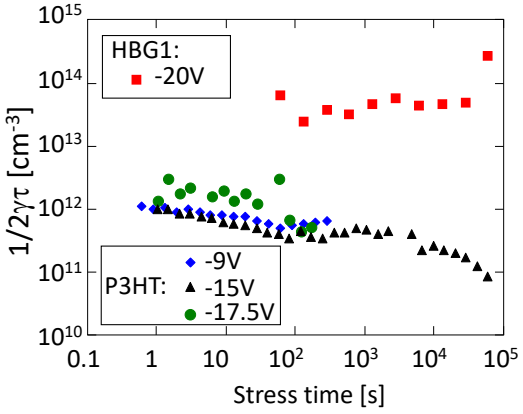

Figure 5.12 Transition point between SRH and Langevin regime during the voltage decay, during electrical stress for HBG1 cells and P3HT cells.

Figure 5.12 shows the variation during stress of the term *1/2γτ*, which conventionally denotes the transition point between the Langevin recombination phase and the trap assisted recombination phase, as already discussed in 4.4.4. As for the previous figures, the extrapolated data are plotted here both for P1 cells and for P3HT cells. No appreciable changes are observed in the P1 cells, while in the P3HT cells the term reduces up to one order of magnitude. In the P3HT cells, this reflects on the faster decay in V_{OC} with increasing stress time, denoting the anticipation in the transition between the two phases of the OCVD.

k_{REC} increases with stress time in all the degraded devices (see Figure 5.6). The larger increase is once again observed in the cell that underwent the stress performed at the highest voltage. Conversely, no significant variations are observed in the P1 cells, even though they were stressed at -20V. This confirms once again the higher stability of P1 with respect to P3HT.

5.3.4 Intrinsic concentrations and energy gap

From the OCVD measurements at different temperatures, the values of the intrinsic carrier concentration n_i, represented in the Arrhenius plot of Figure 5.11(a), can be obtained. For each of the analyzed polymers the intrinsic carrier concentration exponentially decrease at increasing temperature. According to Equation (4.15), this explains the decrease in V_{OC} observed for increasing temperature (Figure 5.7).

Following the procedure described in 4.5.2, the equivalent energy gap of the blend (E_g) was calculated starting from n_i at various temperatures. Some of the energy gap values extrapolated are shown in Table 9.

Figure 5.11(b) shows the correlation plot between E_g and V_{OC}. Assuming an ohmic contact between the organic layer and both the electrodes, the Fermi level of the cathode should be very close to the LUMO level of the acceptor material of the blend. Conversely, the Fermi level of the anode should be very close the HOMO level of the donor. Thus, there should be a linear dependence of V_{OC} from E_g.

This means that the experimental data in Figure 5.11(b) should be fitted by a straight line, as supposed in the description of the procedure to extrapolate the energy gap. The straight line in Figure 5.11(b) has slope 1, and it almost approximates the experimental data:

$$V_{OC} = \frac{E_g}{q} - 0.55V \qquad (5.2)$$

Following this interpretation, the intercept should represent the sum of the barrier heights between the electrode and blend. Assuming a symmetrical band alignment, this gives 0.275eV barrier between each electrode and the organic material, which is reasonable for an ohmic contact [Riz16a].

Once again, it can be observed that P1, P2 and P3 have similar characteristics, while P3HT behaves quite differently. In particular, E_g is similar for P1, P2 and P3 (≈1.45eV), while E_g for P3HT is smaller (≈1.1eV). As expected, this is in line with the large intrinsic carrier concentration of P3HT (Figure 5.11(a)).

It is worth to underline that these values of energy gap do not correspond to the wavelength absorption range shown in Figure 5.1. In fact, the EQE is related to the wavelength absorption of the two materials constituting the blend, and not directly to the energy gap that characterizes the blend itself. This because the excitons are generated inside either donor or

acceptor, and only information regarding the two distinct materials can be obtained. Looking at Figure 5.1 it is possible to observe that, for low wavelengths, all the EQEs exhibit a common and abrupt cut-off. This behavior is associated to the absorption properties of $PC_{61}BM$, which is the

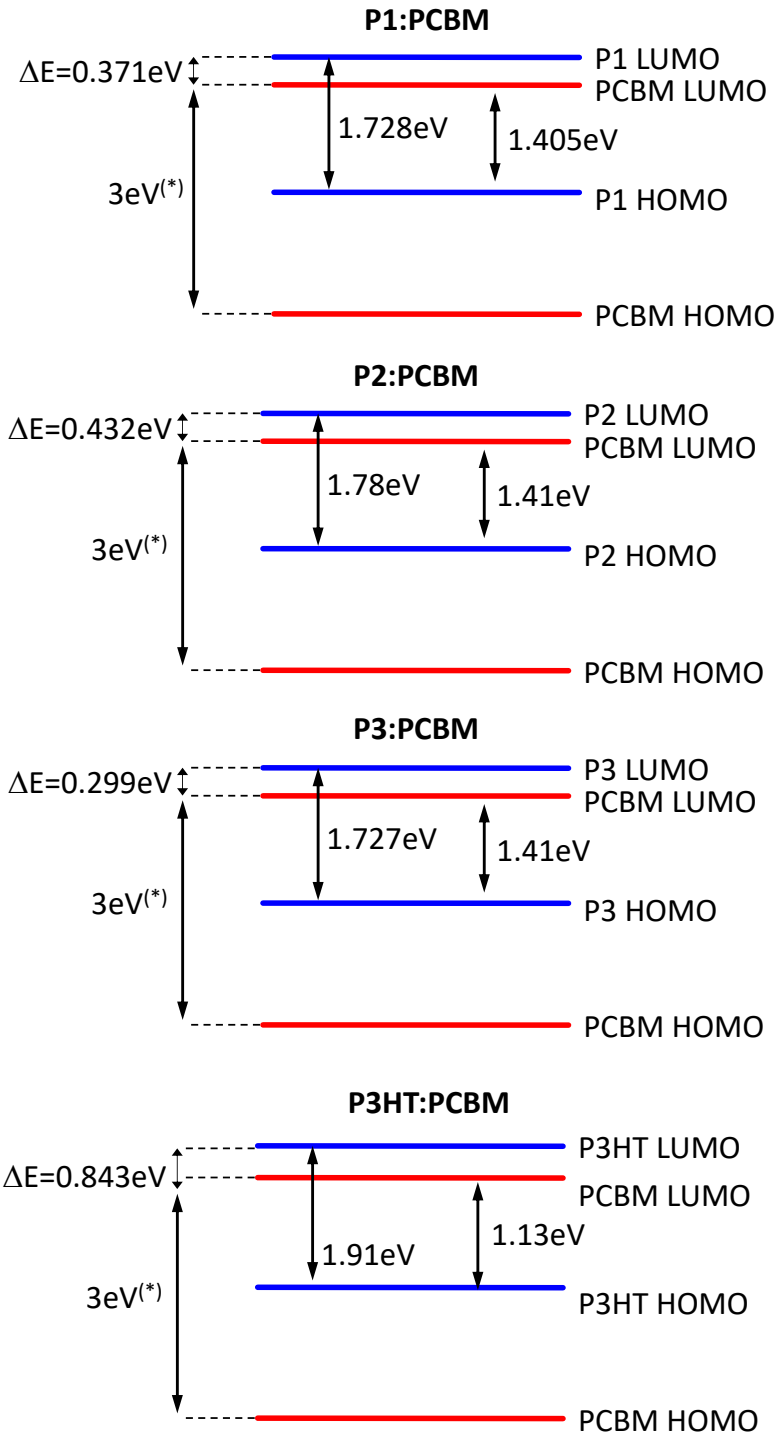

Figure 5.13 Band alignment of the active layer of the four devices. The value of the energy gap of the blend was calculated from the intrinsic carrier concentrations reported in Fig. 8. The donor energy gaps were estimated from the cut-off wavelength of the EQE. (*) $PC_{61}BM$ gap was calculated from ref. [Zab03].

common polymer in all the measured devices. Conversely, at high wavelength, the different cut-off is associated to the donor polymer.

These fact is useful to calculate the energy gap of the donor materials, which are listed in Table 9. Assuming that $PC_{61}BM$ is characterized by an energy gap of 3eV (see Ref [Zab03]), the band diagram of the entire blend of each device can be drawn. The band diagrams of some measured cells are depicted in Figure 5.13. Once again, the similarity between the cells P1, P2 and P3 are evident: the energy gap of the pristine donor polymers is similar for P1, P2 and P3 (around 1.73eV), while for P3HT it is wider (1.91eV). This is in agreement with the lower generation capability of P3HT compared to the other materials (i.e. less extended EQE absorption spectrum).

A last consideration about the band alignment in P1, P2 and P3 is worth to be done. In fact, the difference between LUMO levels (ΔE, Figure 5.13) of P3 and $PC_{61}BM$ might contribute to explain the low separation capability of the device. In fact, among P1, P2, and P3, that are similar, P3 has the lowest ΔE. In fact it is lower than 0.3eV, which is the range of the typical barrier value for an ohmic contact [Riz16a]. Ideally, when a polaron pair is generated, the electron in the acceptor material should be blocked by the presence of a high barrier ΔE in the interface between the donor phase and the respective electrode. In P3, this barrier is smaller and some electrons may jump back into the donor material. This might lead to the conversion of the polaron pairs into excitons, reducing the effective separation probability and the efficiency. Even though the Langevin recombination coefficient and the blend morphology are the factors that mostly influence the Fill Factor of the corresponding devices, ΔE may also play a minor role in reducing P_{SEP}.

5.4 Device and stress description

In this part, the attention is focused only on standard the devices fabricated with a blend of P3HT and $PC_{61}BM$. The active layer is sandwiched between two electrodes. The anode, consists of a silver grid and a hole transport layer (the PEDOT:PSS). The cathode consists of another small silver grid in contact with an additional layer of PEDOT:PSS, and a layer of Flextrode (i.e. a ZnO in contact with the active layer). The active area is $1cm^2$. These organic solar cells that were fabricated at the Energy department in DTU (Roskilde, DK).

In this section, the goal was to investigate the reliability of organic solar cells, separating the effects of different contributions, such as temperature, illumination and bias. In order to do

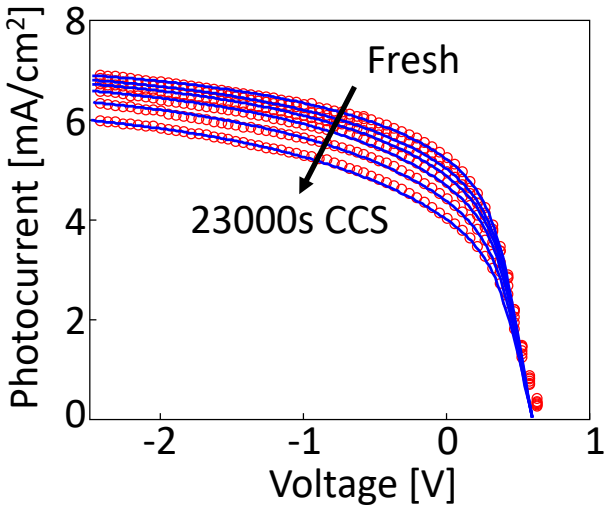

Figure 5.14 Photocurrent during CCS at 70mA/cm². Red circles represent experimental data, solid lines are the model. Each curve is associated to a measurement made after a period of stress.

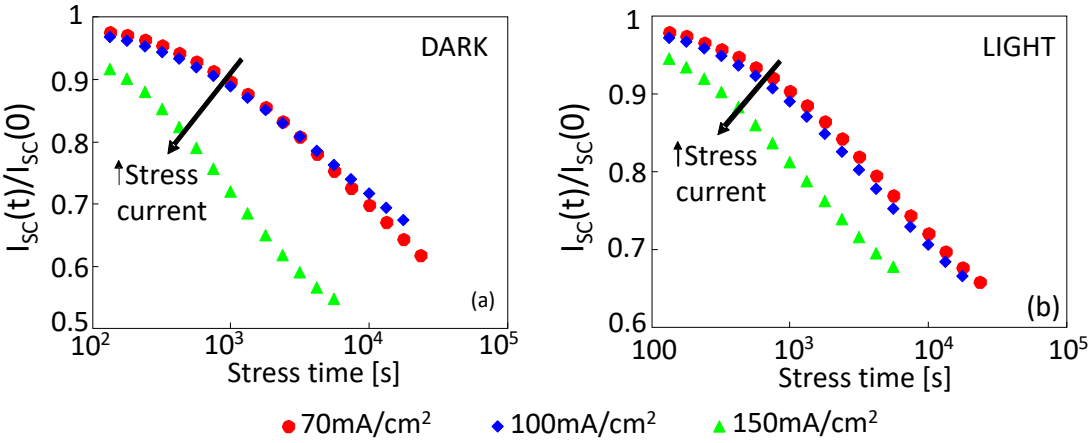

Figure 5.15 Short circuit current during CCS performed in dark (a) and light (b). Each value ($I_{SC}(t)$) is normalized to the fresh value ($I_{SC}(0)$).

so, the cells underwent several stress procedures. In order to study the solar cell reliability in a condition as close as possible to the operative conditions, two type of stresses were used, including illumination stress, temperature stress and bias (electrical) stress. In particular:

- A set of device was subjected to thermal storage at three different temperatures (40°C, 60°C, 80°C) under 1Sun equivalent illumination (i.e. by means of a white LED illuminator - WLED);
- A second set of devices was subjected to an applied bias of -13V. During this electrical stress, the same temperature and illumination levels were maintained. Any possible effect of the reverse polarization is studied to simulate the condition in which a solar panel could undergo in case of partial shading.

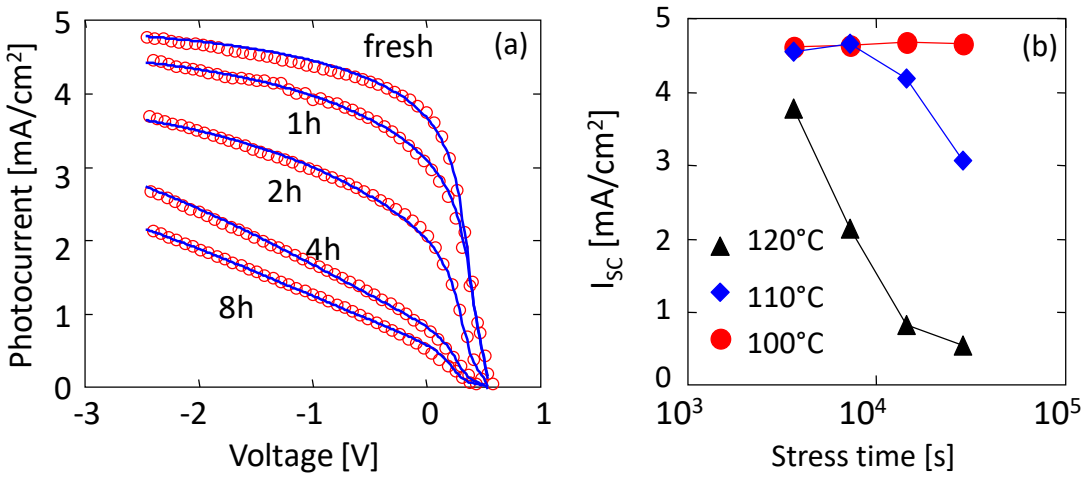

Figure 5.16 (a) Photocurrent during thermal stress at 120°C. Red circles represent experimental data, lines are the model. (b) Short circuit current during thermal stresses. Each symbol and color represents a different stress temperature (from 100°C to 120°C).

Each stress was periodically stopped in order to monitor the device using I-V measurements, impedance spectroscopy and open circuit voltage decay. In the OCVD measurements, the illumination phase lasts 5s, while the voltage of the second phase is monitored for 10s. All characterizations were performed at different temperatures from -25°C to 25°C, with a 10-°C step. From the experimental data, several parameters were extracted by means of the photocurrent and OCVD models, which have been exhaustively described in the previous chapters.

To extend the analysis and to better understand the degradation mechanisms, also the data published in [Riz16a][Riz16b] were taken into considerations, applying to them the photocurrent and impedance models. Those data feature two types of stress made on the same type of solar cells described above. In detail, the stresses performed are:

1) A constant current stress (CCS) made under three different forward current bias: 70mA/cm^2, 100mA/cm^2 and 150mA/cm^2. Each stress was performed in dark and in light at 1Sun equivalent illumination by means of a WLED. The final goal is to emulate the condition of a solar panel where some cells are (partially) shaded.

2) A thermal stress performed at 100°C, 110°C and 120°C under no illumination condition. The device is kept unbiased in order to study the effects of only the high temperature.

5.4.1 Photocurrent measurements

Figure 5.14 shows the photocurrent density J_{PH} variation during a 70mA/cm^2 constant current stress (see 5.4). The solid lines represent the fit made with the model described in Chapter 3, while symbols represent experimental data. From the photocurrent plot under reverse voltages or moderate forward voltages, it is clear that photocurrent produced reduces during stress. On the contrary, no significant variations are observed in the voltage range at which J_{PH} is close to zero (i.e. in the operative region).

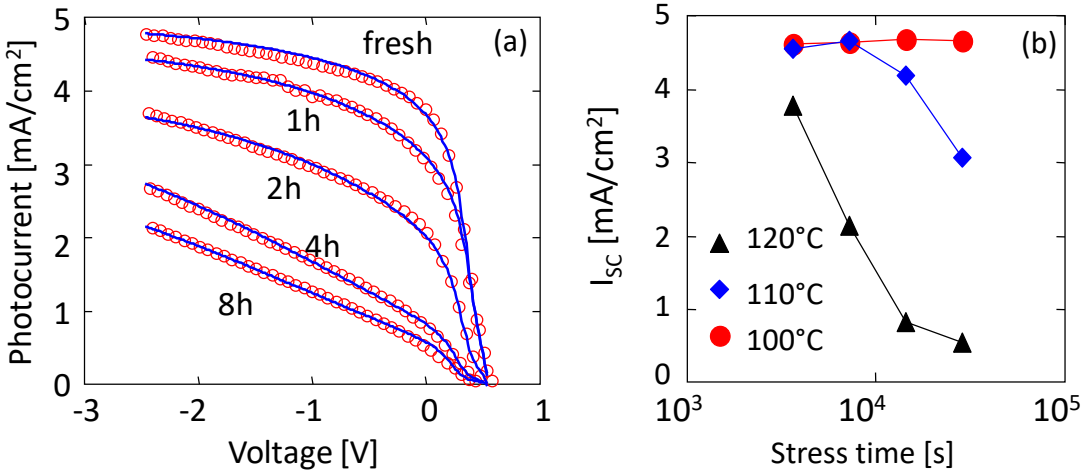

Figure 5.17 (a) Photocurrent degradation during thermal stress at 120°C. Red circles represent experimental data, lines are the model. (b) Short circuit current during thermal stresses. Each symbol and color represents a different stress temperature (from 100°C to 120°C).

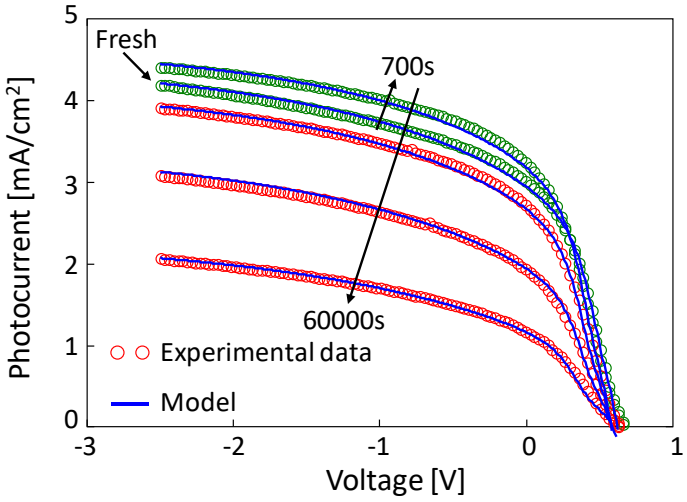

Figure 5.18 Photocurrent during reverse bias stress at -13V under illumination and at 80°C. Red circles represent experimental data, solid lines represent the model.

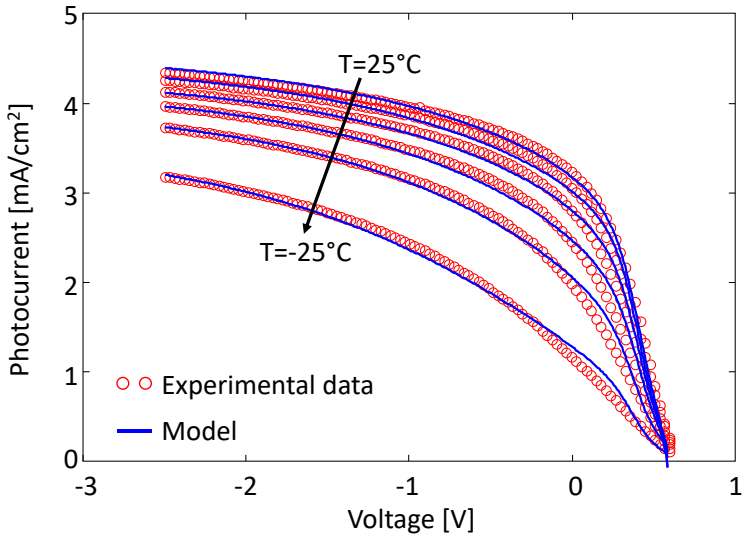

Figure 5.19 Photocurrent during -13V reverse bias stress at 80°C measured at temperatures -25°c, -15°C, -5°C, 15°C, 25°C. Red circles are experimental data, lines are the model.

A similar behavior can be observed at different CCS current levels and illumination conditions. This is shown in Figure 5.15, where a comparison between the evolutions of the I_{SC} produced by the cells at three CCS levels is illustrated, both for cells stressed in dark (a) and in light (b) conditions. The values reported are normalized with respect to the value obtained in the fresh device ($I_{SC}(0)$). Noticeably, the higher the stress current, the faster the degradation kinetics. This is true both for CCS performed in dark condition and for CCS performed in light condition.

Figure 5.17(a) shows the photocurrent generated during a 8 hours - 120°C thermal stress. The solid lines represent the fit obtained by means of the photocurrent model illustrated in Chapter 3. Noticeably, unlike CCS, not only the photocurrent reduces in magnitude, but the shape of the curve also changes. In particular, during the last stress steps, the J_{PH} shape in the reverse bias region almost linearly depends on the voltage and, in turn, on the electric field across the active layer (see 2.7). This behavior is very different from what can be observed during the initial steps of the stress procedure, where the photocurrent (and the charge separation probability) is almost independent on the applied electric field. Furthermore, in the operative region an inflection appears. This is due to a strong degradation in the interfacial region, as will be discussed later. Figure 5.17(b) shows I_{SC} during thermal stresses performed at 100°C, 110°C and 120°C. It is clear that for higher stress temperature, the I_{SC} degradation becomes faster too.

The photocurrent J_{PH} is also shown for a cell stressed at 80°C, biased at -13V under illumination (Figure 5.20). During the first 700s, the photocurrent shows an initial increase,

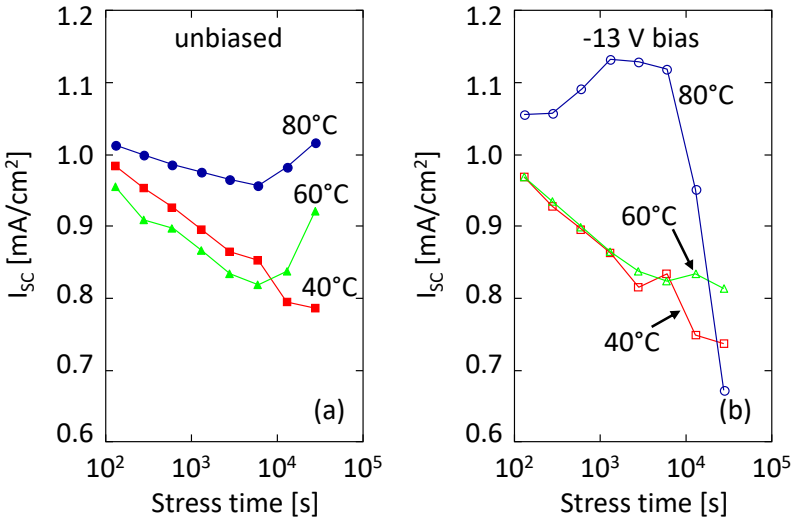

Figure 5.20 Photocurrent taken at 0V during illumination stress for unbiased devices (a) and device stressed under -13V reverse bias (b).

ascribed to a partial annealing of the device. After 1000s, though, the annealing process stops and the photocurrent starts decreasing. This can be appreciated better in Figure 5.20, where the variation of I_{SC} is reported for different cells subjected to illumination stress at different temperatures with no applied bias (Figure 5.20(a)) and under -13V reverse bias (Figure 5.20(b)). All the devices show a general decrease in the I_{SC}. At first glance, the cells stressed at 80°C are the only exceptions, due to the competing effects of annealing and degradation, as will be discussed later.

It is worth to note that a similarity can be observed between the J_{PH} characteristics extrapolated from the cell stressed at 80°C/-13V (Figure 5.18) and the cell that underwent the thermal storage at 120°C (Figure 5.17(a)). In particular, the photocurrent of Figure 5.18, in the region near V_{OC}, features a shape more similar to those of Figure 5.17(a) rather than those of Figure 5.14 (cell underwent CCS). This suggests that at relatively high temperature new degradation mechanisms appear, which are not observable after a standard room temperature electrical stress.

Finally, Figure 5.22 shows the photocurrent produced by a cell at six different temperatures (from -25°C to 25°C). The photocurrent model fits well each curve with a fit precision of 5% with respect to the experimental data, while the fitting procedure permits to extrapolate the parameters with an accuracy of 2%. The results obtained from the fitting of the experimental data suggest that photocurrent decrease is associated to the variation of G_X and k_R (i.e. the ratio k_{REC}/k_{SEP}, see notations in Table 6). The exciton generation rate G_X slightly increases from $2.3 \cdot 10^{21} cm^{-3} s^{-1}$ at -25°C to $2.6 \cdot 10^{21} cm^{-3} s^{-1}$ at 25°C. This could be ascribed to the increase in

exciton dissociation probability, likely due to the increase of the spontaneous dissociation. k_R strongly reduces from 6.16 at -25°C to 0.78 at 25°C, as expected since the Braun Onsager model predicts a strong thermal activation for the separation probability (see Equation (2.8)).

5.4.2 OCVD measurements results

After the results obtained from simple J-V measurements, some OCVD measurement results will be shown. The variation during the stress procedures of the extrapolated parameters presentation and its analysis is postponed to 5.4.4.

Among all the devices analyzed in 5.3, the cell degraded at 80°C under -13V will be taken into consideration for the application of the OCVD model. Its photocurrent is plotted in Figure 5.19, while Figure 5.21 shows some V_{OC} transient during the combined electrical and thermal stress. In particular, the transient shown were taken before the beginning of the stress (fresh cell) and after 2700s, 13000s and 60000s.

As observed in Chapter 4, also in these transients two different slopes can be observed in semi-log scale axes. Approximately, during the first 10ms, V_{OC} decreases smoothly, while in the second part of the curve, V_{OC} decreases more sharply. This is true for all the curves but, with every stress step, the time at which the curve slope changes becomes smaller and smaller as the stress procedes. The same can be said for the slopes of the second part of the decay (which is related to the trap assisted recombination): with increasing stress time, the slopes increase as well.

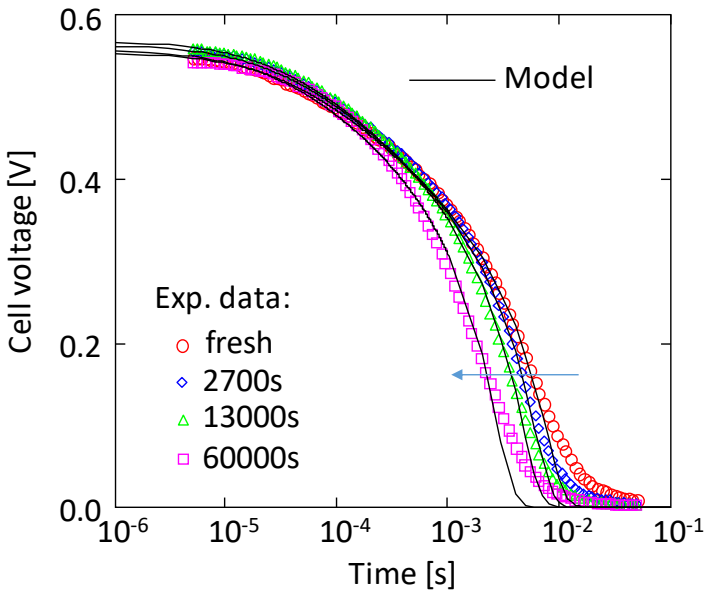

Figure 5.21 Open Circuit Voltage Decay transient for fresh and stressed device. The stress is performed under illumination at 80°C and reverse -13V bias voltage. Each curve is associated to a measurement made after a certain period of time from the beginning of the stress (indicated in figure). Every measurement was made at 25°C.

The OCVD model outputs (solid lines) are superimposed to the symbols of Figure 5.21. For every curves, the transient is fitted very well, even though some discrepancies appear in the last part of it (the extension introduced to the model in Chapter 6 will address this problem).

Noticeably, as already said previously for other measured devices, the geometric capacitance does not play a significant role in the decay of the V_{OC}, even with the structure of these devices. In fact, assuming the geometric capacitance as a parallel plate capacitor, C=Aϵ/d=8.85nF, where A=1cm^2 is the cell area, $\epsilon = \epsilon_0 \epsilon_R$ is the dielectric constant ($\epsilon_R = 3$) and *d*=300nm is the cell thickness. Calculating the resistance from the I-V measurements, the RC constant of the device is 1.8µs, which is much smaller than the decay time of the V_{OC}.

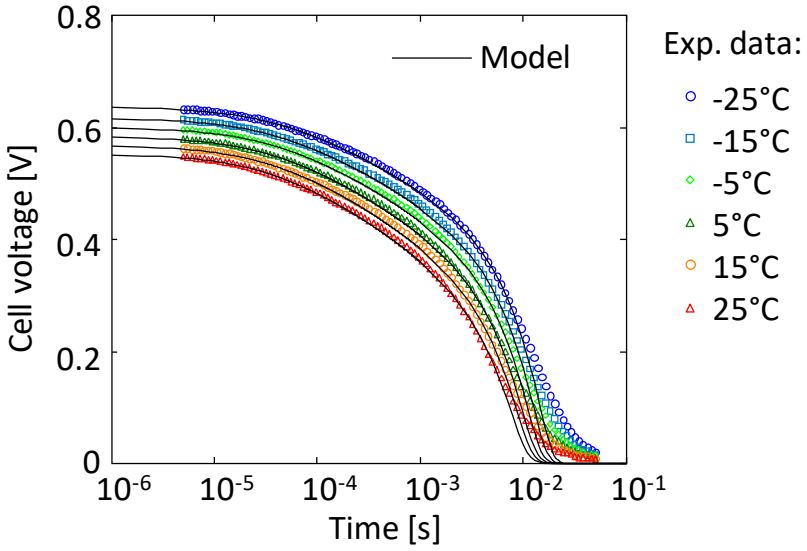

Figure 5.22 Open Circuit Voltage Decay transient for fresh device measured at different temperatures.

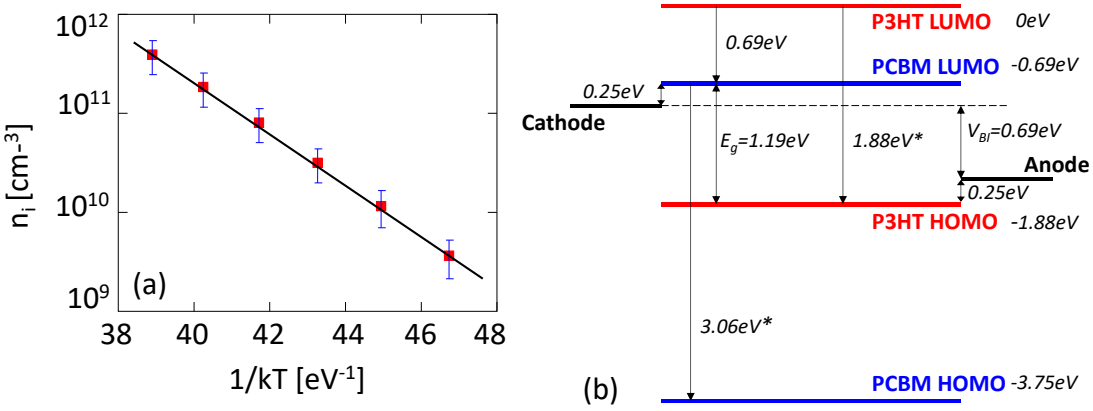

Figure 5.23 a) Arrhenius plot of intrinsic carrier concentration for several identical devices. Each point represents the average value of the concentration and shows its standard deviation. b) Band diagram extrapolated from Eg=1.191eV.

** PCBM and P3HT Energy Gaps used in this diagram are taken from [Ism15]. The energy values on the right are referred to the P3HT LUMO.*

Figure 5.22 reports the OCVD experimental data measured at different temperatures for a fresh cell (different from the cell used to obtain the plot of Figure 5.21, as suggested by the different initial V_{OC}). The model adequately overlaps the experimental data in almost all the decay, and from these curves it can be extrapolated the value of the intrinsic carriers n_i, the recombination coefficient γ and the lifetime τ. The intrinsic carrier concentration n_i remains constant during stress and it only changes with the temperature, as shown in the Arrhenius plot of Figure 5.23(a). Applying the same procedure illustrated in 0 to this Arrhenius plot, it is easy to calculate the energy gap of the active layer, which is E_g=1.19eV.

The energy gap value is in agreement with what reported in [Bis11], where E_g is calculated with more complex electrochemical methods and E_g=*1.20eV*. From this value, the PCBM and P3HT Energy Gaps reported in [Ism15], and the V_{BI} value extrapolated from the photocurrent model, the band diagram of the cell as shown in Figure 5.23(b) can be drawn.

5.4.3 Exciton generation and polaron pairs recombination rate variation during stresses

In order to comprehend the origin of the photocurrent degradation observed previously, it is necessary to study how the electrical stress affects the parameters that can be extrapolated by means of the two model presented in this work.

The photocurrent model predicts a variation only in k_R and G_X, which must be the main responsible for the J_{PH} lowering in the reverse voltage region. In 5.4.4 the analysis will be supported also by the parameters extrapolated from the OCVD measurements.

- **Cell degradation during electrical stress**

Figure 5.24(a) shows the variation of the extrapolated values of k_R for the CCS performed in dark in three different samples. In general, the higher the stress current, the faster the growth of k_R. Nevertheless, a large acceleration appears only in the CCS performed at 150mA/cm^2. As already noticed in [Riz16c], the CCS does not change the mobility. Thus, since k_{SEP} mainly depends on mobility [Bet06], it can be assumed that k_{SEP} remains constant during stress. Hence, the increase in k_R implies a rising polaron pairs recombination rate k_{REC} inside the blend.

Figure 5.25(a) shows the variation of the parameter G_X during stress, normalized with respect to the fresh cell generation value. Once again, the highest degradation that can be observed is associated to the 150mA/cm^2 constant current stress, and it reflects on both G_X and k_R. Furthermore, G_X generally decreases during stress.

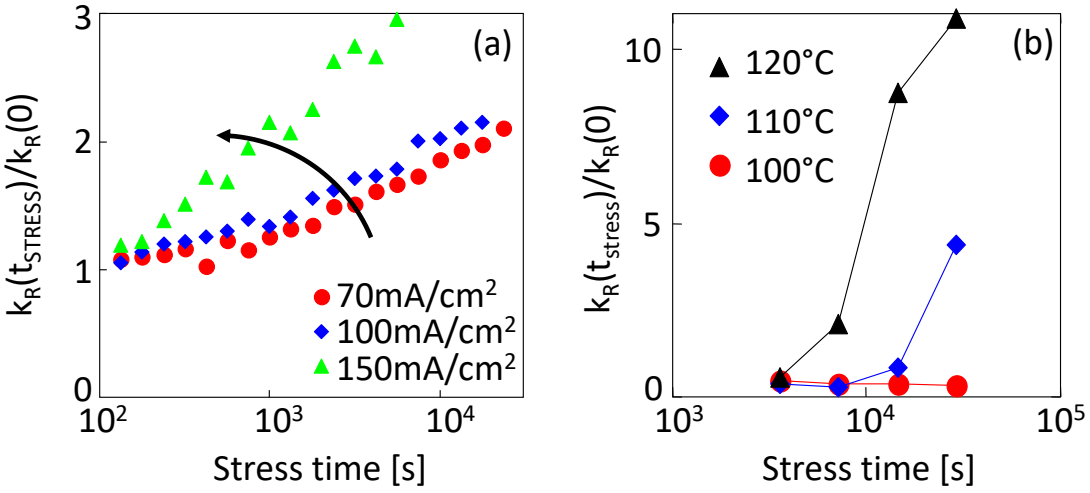

Figure 5.24 Ratio between recombination rate and separation rate (k_R) normalized to the initial value during (a) CCS and (b) thermal stress.

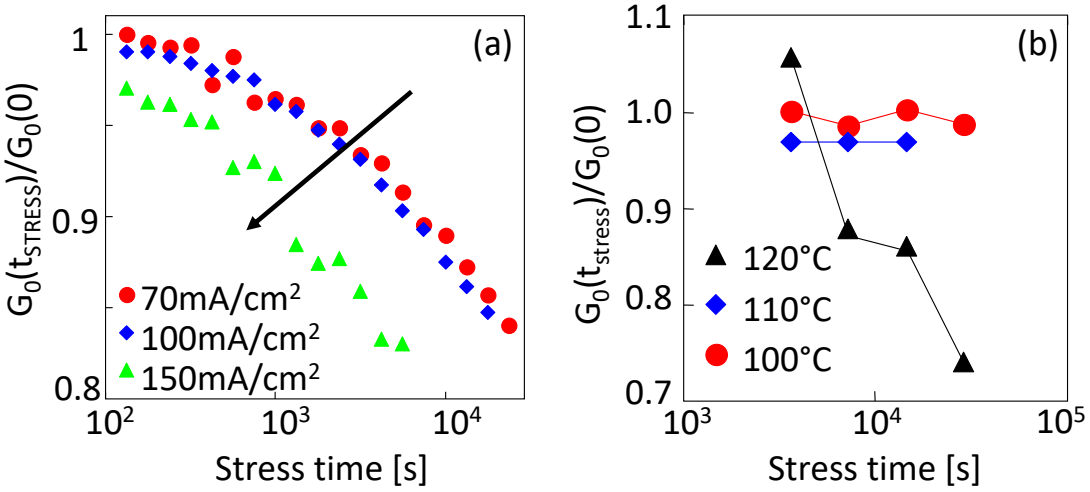

Figure 5.25 Exciton generation rate (G_X) normalized with respect to the initial value.

The results obtained from the fit of I_{PH} data by means of the photocurrent model, suggest that CCS does not impact on the amplitude of the band bending at the interfaces (referred to as Φp and Φn for the anode and for the cathode, respectively. See Chapter 3 for more details). For this reason, only marginal degradation occurs at the contact with the electrodes.

These results indicate that the main reason for the short circuit current reduction shown in Figure 5.15 is the decrease of G_X and the increase of k_{REC}. Besides, it suggests that the generation of defects due to degradation acts as quenching centers for photogenerated excitons and as recombination centers for bounded polaron pairs at the acceptor/donor interface.

- **Cell degradation during thermal stress**

A completely different scenario appears during pure thermal stress. As already noticed in Figure 5.17, the photocurrent shape features a strong change. In particular, one inflection appears in the operative region, differently from what happens during CCS. The photocurrent model explains this behavior with the presence of a partially selective contact, which opposes to the collection of one of the two carriers with respect to the other. Such selection derives from the growth of one of the two band bending Φp and Φn. In fact, it was already demonstrated in 0 that when one of the bendings is much larger than to the other, an inflection in the photocurrent characteristic appears.

This allows to fit almost perfectly the photocurrent produced by the solar devices during thermal stress (see Figure 5.17(a)). Furthermore, using a non-uniform exciton generation rate across the active layer, it is possible to discriminate which of the two interfaces undergoes the heaviest degradation[10]. In Figure 5.26(a) it is shown the evolution of Φp during each thermal stress (each thermal is indicated with a different symbol, according to the stress temperature). The variation is expressed as a difference from the starting value of the barrier with the anode (i.e. $\Phi p(t)- \Phi p(0)$, being $\Phi p(0)$ the value of the barrier in the fresh cell). Because no variation is observed at the interface with the cathode interface (Φn), its variation as a function it time is not shown here. The big change in Φp is related to the formation of defects near the anode interface, which provoke the large band bending. Thus, the photocurrent reduction observed during thermal stress is likely due to some thermally-induced morphological modifications in the active layer. In fact, the stress temperatures are close to the glass transition point of the active layer, estimated to be 110°C [Riz16c][Tor17]. This is why only minor changes appear in the photocurrent, as well as in k_R, G_X, and Φp during the 100°C thermal stress (see Figure 5.24, Figure 5.25 and Figure 5.26). Instead, after the 120°C thermal stress, some morphological rearrangements occur in the active layer, strongly increasing k_R, decreasing G_X and heavily damaging the active layer/PEDOT:PSS interface, increasing Φp.

To obtain more information about the thermal stress effects, the impedance spectroscopy was used, together with the model presented in [Riz16b]. In that model, applied to the same devices here reported, were calculated several parameters such as the transport resistance, the recombination/generation resistance and the interface capacitance of the active layer and ZnO. During thermal stress, the IS parameters show a variation that agrees with that observed by the

[10] This is done simply using the hypothesis about the exponential decay of the generation rate of the excitons, as reported in 3.2.

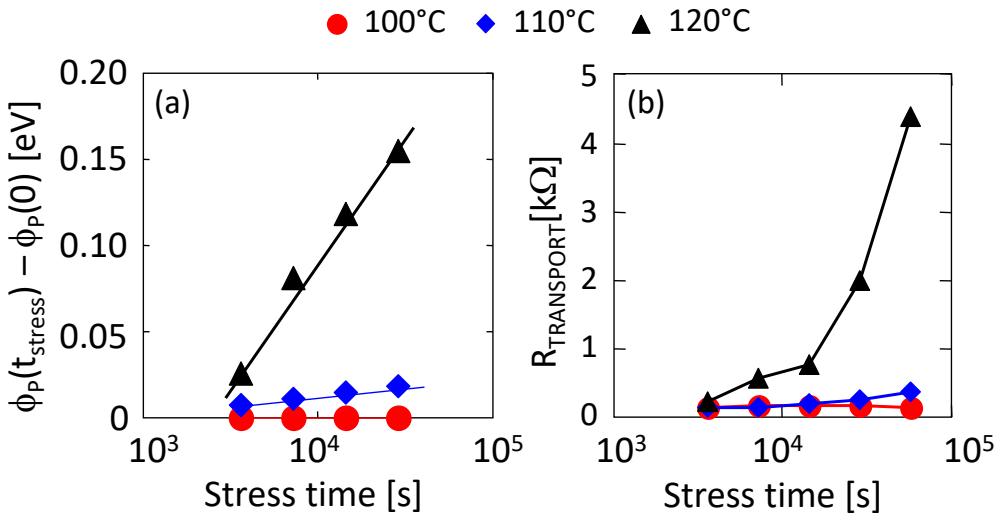

Figure 5.26 (a) Variation of band bending at the anode interface during thermal stress.(b) Transport resistance of active layer estimated by impedance model during thermal stresses.

photocurrent model. As an example, Figure 5.26(b) shows the transport resistance of the active layer calculated from the IS curves. At 100°C the degradation is negligible, while the largest variation occurs at 120°C (in fact the transport resistance becomes almost five times larger).

- **<u>Cell degradation during electrical, thermal and illumination stress</u>**

A third scenario appears when the cells are thermally stressed under illumination with or without reverse bias. The evolution of the parameter extrapolated from the photocurrent analysis shows no clear trend, featuring annealing phases and degradation phases. G_X and k_R for light-soaking stress in unbiased and biased devices are shown in Figure 5.27. Generation shows a similar behavior to what shown in Figure 5.20 by $I_{SC,}$ while the ratio k_R extrapolated from the photocurrent by the model shows a slight increase for all the combined stresses. This is in line with what reported in Figure 5.24(b), where the thermal stress performed at 100°C does not affect heavily the parameter value. In the following, an analysis of all the extrapolated parameters of the stressed cells is reported:

- The cells stressed at 40°C show a decrease in generation and an increase in k_R, independently on the applied bias. This indicates that no recovery occurs during the stress procedure, but only degradation intervenes. To observe an effective recovery, it is necessary to stress the cells at higher temperatures, in order to induce an annealing procedure.

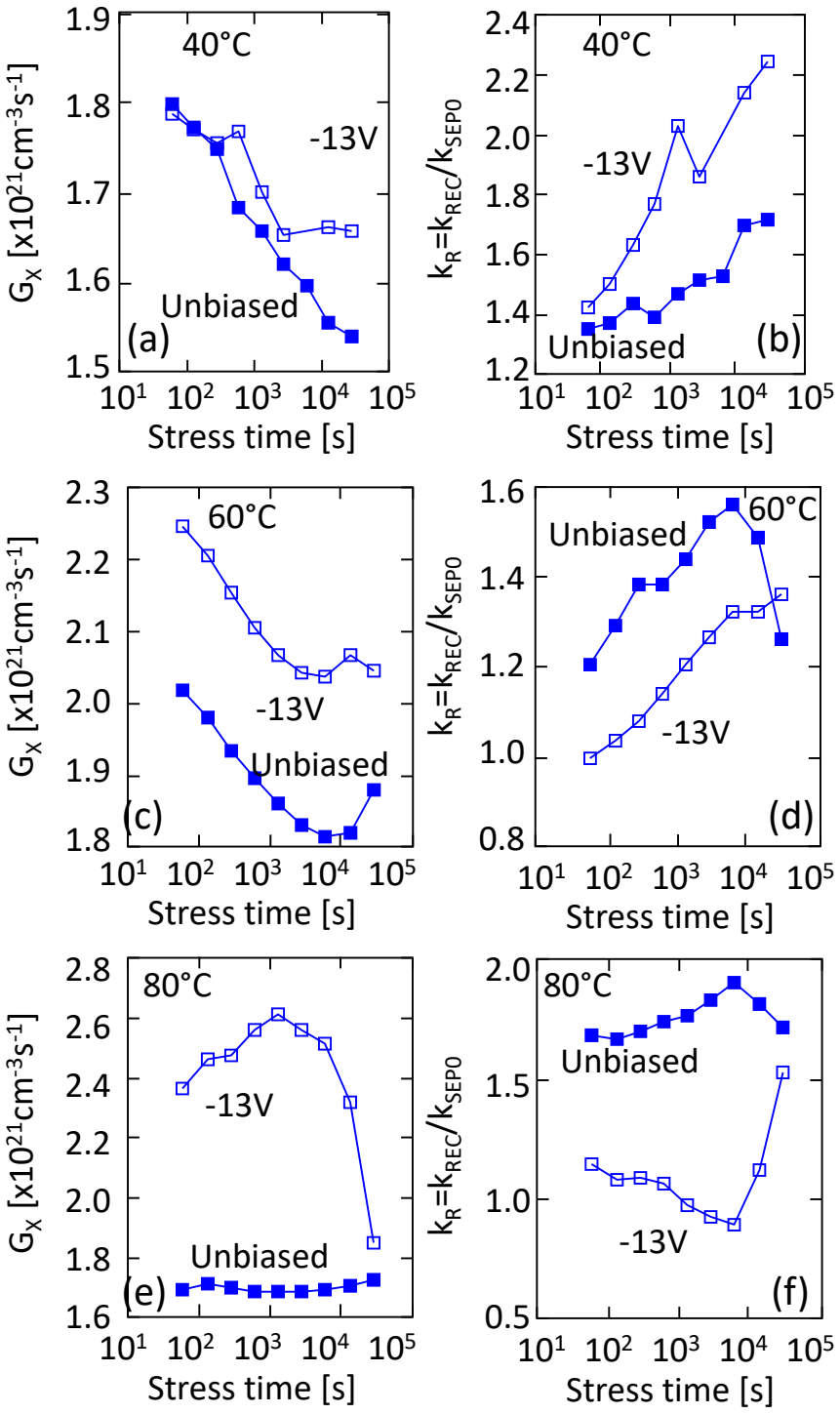

Figure 5.27 Variations of G_X and k_R during illumination stress performed at different temperatures and bias conditions.

- At 60°C, the cells show a degradation during the first part of the stress, and a partial recovery during the last phases. This is due to a recovery effect of temperature, which permits a final reorganization of the polymers inside the blend and the consequent beginning of an annealing process. The annealing is

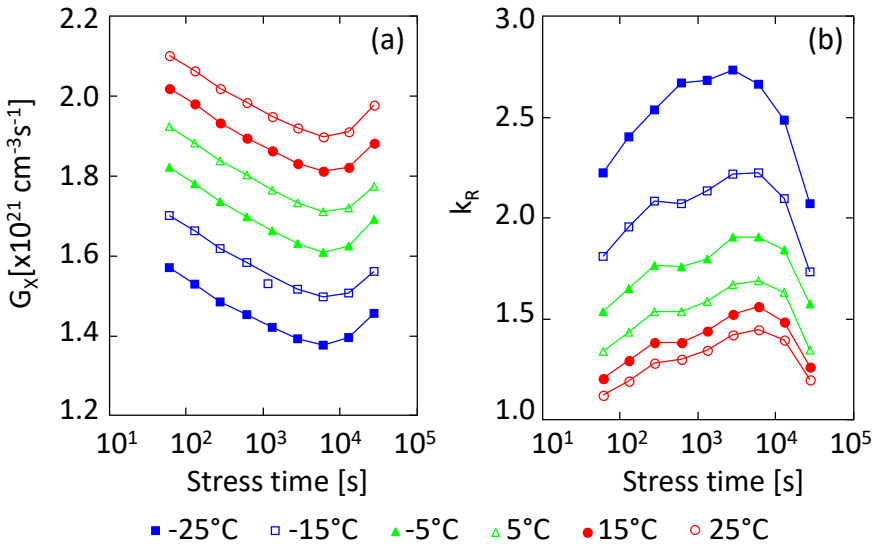

Figure 5.28 Evolution of G_X (a) *and* k_R *(b) extrapolated at different measurement temperatures in a device subjected to illumination stress at 60°C without applied bias.*

emphasized if no bias is applied during stress. On the other hand, when the cells are stressed under -13V, as expected, the recovery rate is smaller.

- The devices stressed at 80°C under no electric bias, show a moderate degradation of k_R during the most part of the stress procedure. The maximum damage is observed after 10000s (when G_X abruptly decreases), and can also be observed in the decrease of I_{SC} (Figure 5.20(a)). Furthermore, after 10000s, k_R reduces. This is in agreement with the increase of I_{SC} in Figure 5.20(a). Instead, only marginal variations occur in the generation rate G_X. On the contrary, the devices stressed under bias, despite the slight recovery during the first thousands of seconds, show a large and fast degradation in the final part of the stress.

All these results clearly highlight the presence of two competing mechanisms that act at the same time: degradation and annealing. The first mechanism is associated to the electrical stress, while the second mechanism is associated to the effects of temperature. Degradation prevails on annealing at 40°C (i.e. when the temperature is relatively low), while the strength of annealing begins to increase at 60°C. At 80°C the annealing effect becomes even stronger, resulting in a partial compensation of the detrimental effects due to the electrical stress. This is the reason why the cells stressed at 80°C shows a slightly different behavior respect to the other cells.

G_X and k_R are also reported in Figure 5.28(a) and (b), respectively, for various measurement temperatures. There is a clear trend in the parameters kinetics. Figure 5.28(a) says

that the lower the temperature, the lower the generation, confirming the reduction of the exciton dissociation probability at the acceptor/donor interface. Furthermore, as shows Figure 5.28(b), when the temperature is low, the ratio k_R becomes high, as discussed above.

Even though Figure 5.28 reports the parameters behavior for one particular device, the same behavior is followed by all devices for each temperature.

Even though it is not possible to find a clear trend in the cell parameters during a pure illumination stress or during illumination and reverse bias stress, it is clear that the degradation in reverse bias condition is smaller than that in forward bias condition. In order to prove this, the cell degradation after 10^4s stress is now considered.

The CCS shows a short circuit current decrease up to 50% in the worst condition (Figure 5.15). Instead, reverse bias stresses show a maximum I_{SC} reduction up to 75% (Figure 5.20). A similar variation occurs if the device is illuminated without bias. These data are in agreement with the variation of G_X and k_R. During CCS, G_X reduces up to 20% and k_R increases very strongly (up to 300%). Instead, during reverse bias stress, G_X variations are within the 10% of its initial value and k_R increases of 50% at most. This suggests that the electrical stress is more damaging when the cell operates in forward bias condition rather than when it operates in reverse bias.

5.4.4 Effects of the stress on OCVDs

A direct correlation exists between the transition point of the voltage decay (see 4.4.4) and the charges lifetime τ. As soon as the light is turned off, all the photogenerated charges are still present inside the active layer and electrons and holes concentrations are much larger than those at equilibrium concentration.

As already observed, Figure 5.21 highlights that the curves change slope earlier with increasing stress time (80°C, -13V for 60000 seconds). This is a clear signature that the stress induces a decrease in τ, probably due to the already mentioned formation of defects that mediate the recombination (see 5.4.3). The change in τ can be observed in Figure 5.29(a), which shows the parameter variation for the devices stressed at 80°C under -13V. The main trend of τ is decreasing, even if an increase can be observed during the first stress steps. Probably, this behavior is correlated to the increasing of the photocurrent shown in Figure 5.18 during the first stress steps. This annealing phase is due to the reduction of the number of trapping centers inside the active layer.

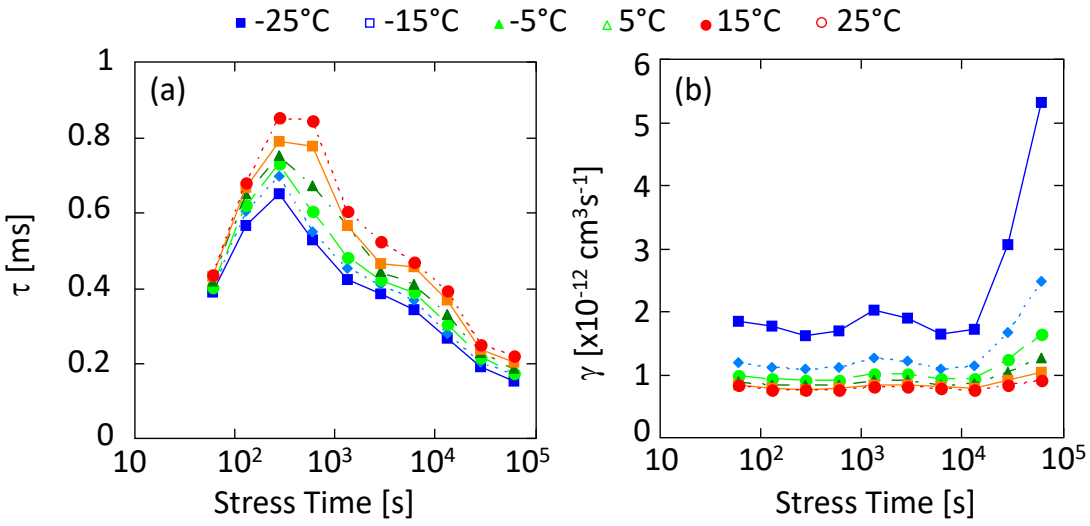

Figure 5.29 (a) Evolution of the lifetime τ during a stress performed at -13V reverse bias under illumination at 80°C. (b) Evolution of the Langevin recombination coefficient γ during a stress performed at -13V reverse bias under illumination at 80°C.

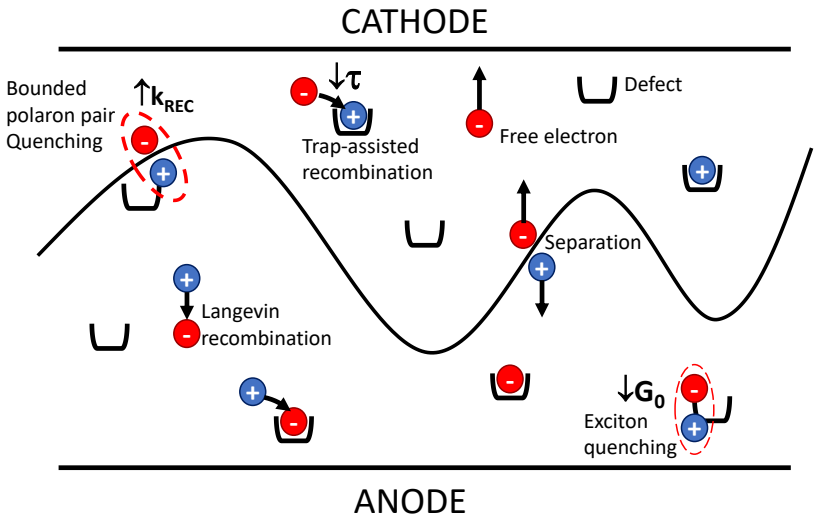

Figure 5.30 Drawing of the different recombination phenomena involving exciton and free carriers in the bulk and interface of the active layer

The Langevin recombination γ, which evolution is shown in Figure 5.29(b), remains constant during stress for the first 10^4s, independently on temperature. The only variations are observed towards the last stress steps, when *γ* grows more and more with lowering temperature.

A schematic picture of what occurs within the active layer of the solar cell is shown in Figure 5.30. It may be assumed that the blend is rich of defects, which are equally distributed both at the interface between donor and acceptor, and in the bulk of the two materials that compose the blend. The behavior of the defects depends on their distance from the acceptor/donor interface: the bulk defects act as quenching center for excitons or as traps for carriers; the defects

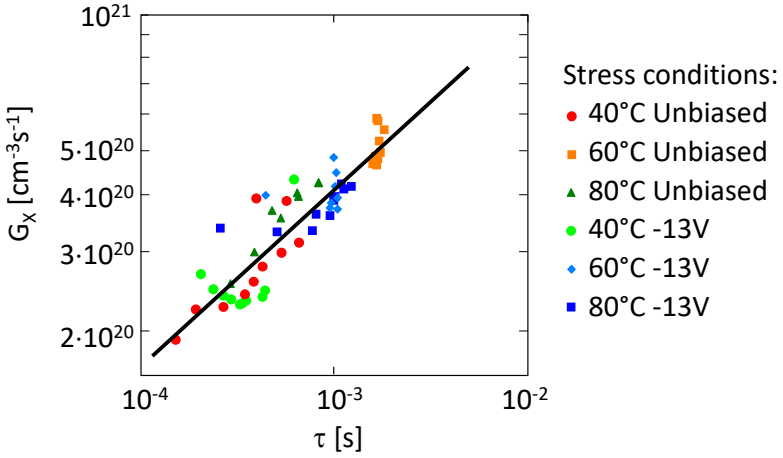

Figure 5.31 Correlation between G_X and τ. Different symbols refer to the data extrapolated from cells subjected to six stresses performed at temperatures of 40°C, 60°C, and 80°C with and without the applied bias. The black, solid line highlights that all the exciton generation rates are linearly correlated with their lifetimes.

at the interface act as recombination centers for the polaron pairs. Thus, an increase in the bulk defects is expected to quench excitons (reducing the generation rate G_X) and to increase the carrier recombination (decreasing τ). On the other hand, the increase of the interface defects is expected to increase the polaron pairs recombination rate k_{REC}.

It is worth to note that τ follows the same evolution of G_X and k_{REC} during the first stress steps, due to a reduction of defects concentration in the active layer. On the contrary, during the last stress steps, G_X decreases, τ decreases and k_{REC} increases, highlighting an increase in the number of defects. This is in agreement with the I_{SC} behavior shown in Figure 5.20. In fact, the results show that the stress has a twofold effect. For instance, during stress performed at 80°C and -13V, the I_{PH} shows an initial increase and then a decrease.

It is clear from this discussion that the parameters extrapolated by means of the photocurrent model must be in close correlation with the parameters extrapolated by means of the OCVD model. This underlines that the approach of the models to the analysis of the solar cells is correct. In order to further confirm this, Figure 5.31 shows the correlation between G_X and τ. The strong proportionality between the two parameters confirms that the same defects that act as recombination centers for excitons are also recombination centers for free carriers.

From the OCVD model it was estimated the value of n_i, N_C and E_g during stress (see Figure 5.23(a) and (b)), which remain almost constant. In particular, the fact that E_g is unchanged, implies that only marginal variations occur in the alignment between the work function of the electrodes and the transport level. Thus, such alignment is determinant for the height of the band bending

localized near the electrodes. This is in agreement with what discussed previously: the banding near the electrodes does not change during electrical stress.

Finally, because n_i, N_C and E_g are not appreciably affected by illumination, electrical stress or the combination of electrical and illumination stress, the materials do not undergo appreciable morphological changes for temperatures below 100-110°C, confirming [Hin11][Zha09].

5.5 Conclusions

In this Chapter several experimental data have been analyzed with the aid of the OCVD model and of the photocurrent model. The analysis was focused on two different groups of solar cells. The first group was made of devices characterized by the same structure, but with different active layer donor polymers (in total 4 different donor polymers, called P1, P2, P3 and P3HT, which was used as reference). The second group was made of devices with an active layer composed of P3HT:PCBM, and the analysis was focused on the reliability.

In the first group of solar cells, several J-V, EQE and OCVD measurements were performed. The results of the measurements were analyzed by means of the models developed in this work, gaining information about recombination mechanisms inside the active layer and about the band diagram of the OSC blend. In particular, the main limiting factors behind the low performances of some devices was discovered.

For instance, among the analyzed polymers, it was found that the devices based on P1, P2 and P3 donor polymers have similar photovoltaic properties, even better than P3HT. Interestingly, for the P3-based devices, the generation capability is very high, even though the polaron pair separation probability is relatively low. Thanks to the model, this was related to the high Langevin recombination coefficient and, to a lesser degree, to a non-optimal energy band alignment of the polymers in the blend.

The behavior of some of these devices during electrical stress was investigated as well. It was discovered that the electrical stress is responsible for the photocurrent reduction and for the increase of the recombination mechanisms of free carriers. Many evidences demonstrated the higher stability and reliability of P1 cells during electrical stress in comparison to the analogous system based on P3HT cells.

The second group of solar cells was analyzed by means of several thermal and electrical stress procedures. The analysis suggests that the electrical stress in forward condition mainly generates defects in the active layer, lowering the photocurrent. This produces the decrease of

generation, the reduction of the probability separation, and the decrease of the carrier lifetime. . On the other hand, the thermal stress has the effect of lowering the photocurrent (due to the modification of exciton generation and recombination rate) and changing its shape, due to the degradation of the anode interface, which causes the growth of the band bending at the anode. The photocurrent produced by the cells degraded with the illumination and reverse bias stresses can be fitted with the modification of only the generation and separation probability. Only minor changes can be observed in the band bending heights, Φp and Φn. This points that a temperature as high as 100°C is needed in order to produce significant degradation at the contact interface. Besides, a stress performed in forward condition is more damaging than a stress performed in reverse bias condition.

To support this analysis, which was mainly made by means of the photocurrent model, OCVD measurements were made, enabling also the extraction of some important information regarding the carrier recombination inside the active layer. The shape of the OCVD characteristics is explainable introducing the effect of the bimolecular recombination and the effect of the trap-assisted recombination (SRH model).

Some discrepancies were found during the fit of some OCVDs produced by some devices, especially in the final part of the decay (i.e. where the SRH recombination is the main recombination mechanism). This fact requires to be addressed by means of some modifications in the OCVD models, which will not allow to use an analytical expression for the V_{OC} fitting. This argument will be treated in Chapter 6.

5.6 References

[Bet06] R. De Bettignies, J. Leroy, M. Firon, C. Sentein, “Accelerated lifetime measurements of P3HT:PCBM solar cells”, Synth. Met., Vol. 156, p. 510–513, 2006.

[Bis11] J. Bisquert and G. Garcia-Belmonte, “On Voltage, Photovoltage, and Photocurrent in Bulk Heterojunction Organic Solar Cells”, J. Phys. Chem. Lett., Vol. 2, p. 1950–1964, 2011

[Hin11] H. Hintz, H. Peisert, H.-J. Egelhaaf, and T. Chassé, “Reversible and Irreversible Light-Induced p-Doping of P3HT by Oxygen Studied by Photoelectron Spectroscopy (XPS/UPS)”, J. Phys. Chem. C, vol. 115, p. 13373–13376, 2011.

[Ism15] Y. A. M. Ismail, T. Soga, and T. Jimbo, “Effect of Composition on Conjugation Structure and Energy Gap of P3HT:PCBM Organic Solar Cell”, Int. J. New. Hor. Phys., Vol. 2, p. 87-93, 2015.

[Riz16a] A. Rizzo, L. Torto, N. Wrachien, M. Corazza, F. C. Krebs, S. A. Gevorgyan and A. Cester, “Application of photocurrent model on polymer solar cells under forward bias stress”, Journal of Photovoltaics, vol. 6, pp. 1542-1548, 2016.

[Riz16b] A. Rizzo, A. Cester, N. Wrachien, N. Lago, L. Torto, M. Barbato, J. Favaro, S. A. Gevorgyan, M. Corazza, F. C. Krebs “Characterization and modeling of organic (P3HT:PCBM) solar cells as a function of bias and illumination”, Sol. Energy Mater. Sol. Cells, Vol. 157, p. 337-345, 2016.

[Riz16c] A. Rizzo, A. Cester, L. Torto, M. Barbato, N. Wrachien, N. Lago, M. Corazza, F.C. Krebs, S. A. Gevorgyan, “Effects of Current Stress and Thermal Storage on polymeric heterojunction P3HT:PCBM solar cell”, IEEE-International Reliability Physics Symposium – IRPS 2016, p. 3C-2-1 – 3C-2-6, Pasadena, CA, USA, April 17-21, 2016.

[Sok82] R. Sokel and R. C. Hughes “Numerical analysis of transient photoconductivity in insulators”, *J. Appl. Phys.*, Vol. 53, n. 11, p. 7414, Nov. 1982. doi: 10.1063/1.330111

[Tor16] L. Torto, A. Cester, A. Rizzo, N. Wrachien, S. A. Gevorgyan, M. Corazza, and F. C. Krebs, “Model of organic solar cell photocurrent including the effect of charge accumulation at interfaces and non-uniform carrier generation”, IEEE Journal of the Electron Devices Society, vol. 4 pp. 387-395, 2016, DOI: 10.1109/JEDS.2016.2602563.

[Tor17] L. Torto, A. Cester, L. Passarini, A. Rizzo, N. Wrachien, M. Seri, M. Muccini, “Open Circuit Voltage Decay as a Tool to Asses the Reliability of Organic Solar Cells:P3HT:PCBM vs. HBG1:PCBM”, IEEE – International Reliability Physics Symposium – IRPS 2017, p. 2F-2-1 – 2F-2-10, Monterey, CA, USA, April 2-6, 2017.

[Zab03] A. Zaban, M. Greenshtein, and J. Bisquert “Determination of the Electron Lifetime in Nanocrystalline Dye Solar Cells by Open-Circuit Voltage Decay Measurements”, Chem. Phys. Chem., Vol. 4, p. 859–864, August 18, 2003.

[Zha09] J. Zhao, A. Swinnen, G. Van Assche, J. Manca, D. Vanderzande, and B. Van Mele, “Phase diagram of P3HT/PCBM blends and its implication for the stability of morphology”, J. Phys. Chem. B, vol. 113, no. 6, pp. 1587–91, Feb. 2009.

Chapter 6 Non-constant carrier concentration OCVD model

6.1 Introduction

In the previous chapters, two models based on two measurement techniques were described: the conventional J-V measurement (see Chapter 3) and the open circuit voltage decay (OCVD, see Chapter 4).

The former permits to extrapolate some figures of merit and transport parameters (such as carrier mobility, shunt resistance, fill factor, etc.). The latter permits to gain information about the electronic band structure of the active layer and about the photogenerated carrier recombination. These parameters are not estimable via conventional J-V measurements, but they permit to obtain a full picture of the mechanisms occurring in the carrier photogeneration process inside an organic solar cell. This was shown in Chapter 5, where the OCVD model has been used as an essential tool to fully investigate the device behavior.

Even if the OCVD model presented in Chapter 4 was accurate enough for a first order parameter extrapolation, further improvements could be desirable, in order to extrapolate better the information on the carrier recombination inside the active layer with a better accuracy. This is a crucial point in the analysis of a solar cell. In fact, the carrier recombination not only affects the voltage decay, but also plays an important role in term of power conversion efficiency and in the health of the photovoltaic cell. Thus, the OCVD measurement becomes an important tool to analyze the solar cell behavior and reliability.

In order to improve the OCVD model previously developed, some hypotheses made in Chapter 4 need to be changed or eliminated, as will be described during this chapter. In order to do this, several drift-diffusion simulations of the organic solar cell in transient regime will be performed. Once the extended model will be fully developed, a better accuracy in the parameter extrapolation will be achieved, as well as more information about the electronic band structure of the device. In particular, the alignment between the electrode work functions and the active layer transport bands will be estimated, permitting to trace the full band diagram of a polymeric solar cell.

6.2 Modification of the OCVD model introducing the non-constant carrier distribution

6.2.1 Model description: non-uniform carrier concentration

The second phase of the OCVD is strongly influenced by the carrier concentration inside the active layer. In particular, the strength of the Langevin recombination is high if a large excess of both photogenerated electrons and holes is present in the same region. In other words, both *n* and *p* must be much larger than the pre-existing equilibrium carrier concentration values in order to have a high bimolecular recombination rate (see 2.7.1). Surely, this is not valid in the proximity of the interfaces with the electrodes. In fact, the Fermi level position at these interfaces is determined by the alignment between cathode (anode) work function and the LUMO (HOMO) of the acceptor (donor) material. This leads to an accumulation of electrons close to the cathode, and to an accumulation of holes close to the anode, as widely discussed in Chapter 3. Hence, even though a large amount of carriers are photogenerated, the pre-existing accumulated charges always dominates over the photogenerated carriers near the interfaces. On the contrary, in the central regions of the active layer (i.e. far from electrodes), the carrier concentration remains almost unchanged. In fact, in this region there is a strong concentration of photogenerated carriers, which are supposed to dominate over the pre-existing carriers. On the whole, the carrier concentration inside the active layer is strongly non constant with position.

The model presented in Chapter 4 did not take into consideration this non-uniform carrier distribution inside the active layer, and it was considered everywhere constant. Instead, a more realistic representation of what happens inside the solar cell can be achieved considering that, with respect to the standard model:

- The carrier concentration remains almost unchanged in the central region of the film, and is equal to the photogenerated charge concentration;

Symbol	Value	Description
E_{LUMO}	-4eV	Acceptor lowest unoccupied molecular orbital
E_{HOMO}	-5eV	Donor highest unoccupied molecular orbital
E_G	1eV	Energy gap (ELUMO-EHOMO)
Φ_A	4.8V	Anode work function
Φ_K	4.2V	Cathode work function
Φ_B	0.2eV	$E_{LUMO} - (-q\Phi_K) = (-q\Phi_A) - E_{HOMO}$
N_C, N_V	10^{20} cm^{-3}	LUMO and HOMO effective density of state
μ_n, μ_p	$10^{-4}cm^2/Vs$	Electron and hole mobilities
ε_R	3	Relative dielectric permittivity
γ	$10^{-11}cm^3/s$	Langevin recombination constant
$\tau_n=\tau_p=\tau$	10µs	Electron and hole lifetimes
L	300nm	Active layer thickness
V_{BI}	Φ_A-Φ_K	Built-in voltage

Table 10 Symbols and notation used in the model

- The global carrier concentration is higher than the photogenerated carrier concentration close to the interfaces with electrodes.

Being the Langevin recombination rate and the SRH recombination rate dependent on the carrier concentration, reasonably the same behavior can be observed in R_L and R_{SRH}. The biggest consequence of this is that they cannot be considered spatially constant anymore. In order to investigate how this affects the recombination rate and the accuracy of the previous model, several drift-diffusion simulations were performed by solving the transport equation in transient regime[11].

As a base-case study – useful to illustrate the carrier recombination dynamics and the approach to improve the model – a simulation of the carrier concentration evolution during an OCVD is shown in Figure 6.1. The simulation was obtained using the simulation parameters listed in Table 10.

In order to give a straightforward explanation of the model the simulated device has symmetrical band structure and identical parameters for electrons and holes. In particular, it is assumed the same difference Φ_B between the LUMO (HOMO) band and the cathode (anode).

[11] The transport equation were solved by means of Crank-Nicolson method [Epp13].

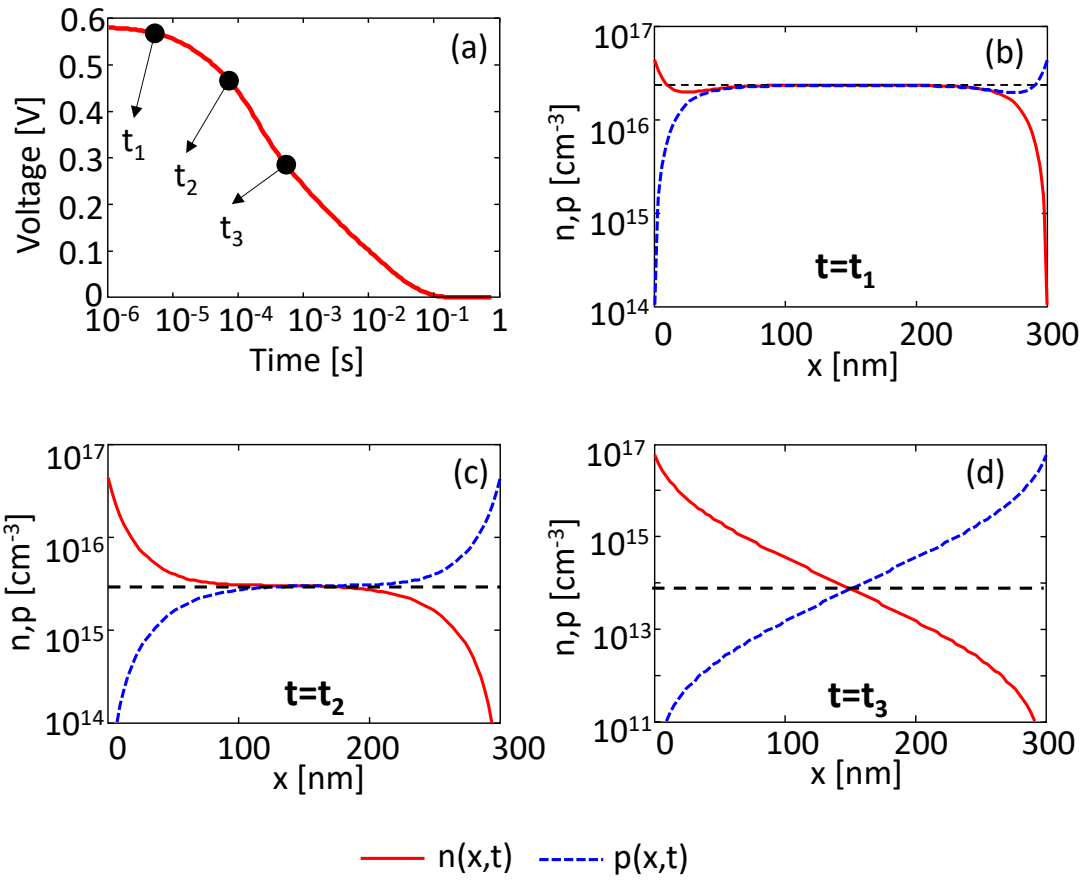

Figure 6.1 (a) Drift-diffusion simulation of a V_{OC} decay transient after illumination. t1, t2 and t3 mark three different instants during the decay. Figs. (b), (c) and (d) show the simulated carrier concentration inside the active layer at the instants t_1, t_2, and t_3.

Thanks to these assumptions, the electron *n(x)* and hole *p(x)* concentration result spatially mirrored each other.

Figure 6.1(a) shows the simulated open circuit voltage decay over a period of 1s obtained by means of an OCVD simulation performed using the above-mentioned solar cell. Figure 6.1(b)-(d) show *n(x)* and *p(x)* at three different moments during this V_{OC} decay transient, marked as t_1, t_2, t_3 in the V_{OC} plot.

At t_1 (Figure 6.1(b)), *n(x)* and *p(x)* are almost everywhere constant and they overlap in most of the film. In this situation, the photogenerated charges concentration is high in almost all the active layer and a pre-existing charge accumulation can be observed in close proximity of the electrodes. At t_2 (Figure 6.1(a) and (c)), V_{OC} reduces due to the general decrease of *n(x)* and *p(x)*. Noticeably, at t_2 they only slightly overlap in the middle of the film. In particular, from the center to the interfaces, they change by more than one order of magnitude and the carrier concentration can hardly be considered constant anymore. This is also true at t_3 (Figure 6.1(d)), when *n(x)* and *p(x)* are much lower in the bulk region of the film than in the regions near the electrodes.

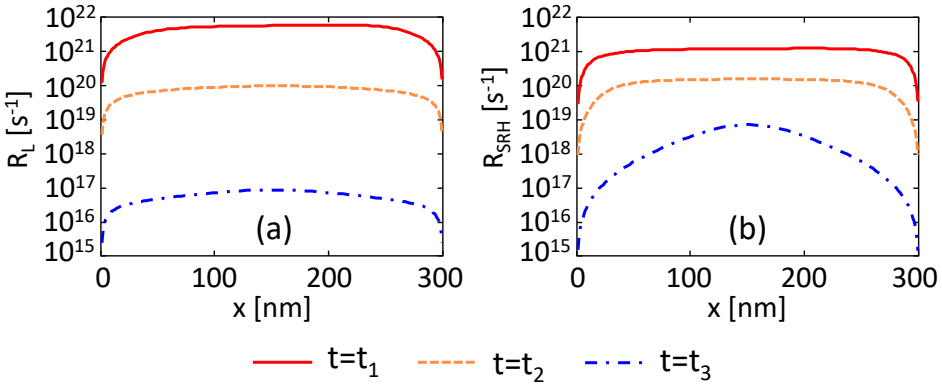

Figure 6.2 Evolution of the recombination rates R_L (a) and R_{SRH} (b) as a function of the position inside the active layer. Each curve represents the different moment in the decay marked in Figure 6.1 (a).

Remarkably, after t_2, *n(x)* and *p(x)* cannot be considered spatially constant anymore. This is due to the presence of charge accumulations induced by the electrodes at the interfaces, both during illumination and in equilibrium.

The non-uniform distribution of the carrier inside the active layer implies that also $R_{SRH}(x)$ and $R_L(x)$ cannot be considered spatially constant after t_2, even though recombination is still present all over the film. This is a very strong difference with the model described in Chapter 4, and it will lead to interesting considerations in the following.

Figure 6.2 shows the evolutions of R_L and R_{SRH} as functions of the spatial position *x* inside the active layer for the instants marked as t_1, t_2 and t_3 in Figure 6.1(a). While at t_1 and t_2 the two recombination rates can be considered almost constant in the central region of the film, this is not true at t_3. In fact, after t_3, the recombination rates inside the active layer may change by several order of magnitude from the center to the interface with the electrodes, especially in the case of R_{SRH}. Close to the interfaces, due to the strong difference between the charge carrier density *n(x)* and *p(x)* (see Figure 6.1(d)), the recombination is weaker than in the middle. The non-uniformity of R_{SRH} and R_L implies that the assumption made in the previous model is true only in the initial part of the decay, i.e. where *n(x)* is approximately equal to *p(x)* in all the active layer. Despite this approximation was suitable in Chapter 4, which was focused on a first order study of the recombination mechanisms, in other cases this could lead to a sub-optimal accuracy.

6.2.2 Model implementation

Even if the V_{OC} decay of an organic solar cell could be accurately simulated by means of a drift diffusion algorithm, it needs large computational effort and is very time consuming (in some cases, a 1-second transient simulation could need more than one hour of processing, if high accuracy is needed). As trade-off, the previous OCVD model is modified in order to take into

account also the effects of the spatial dependence of *n* and *p*, keeping the model as simple as possible. The approach aims to remove the x-dependence of *n*, *p*, R_L, and R_{SRH}, using effective values for concentrations and recombinations, greatly simplifying the computational effort. Once this is done, these parameters will only be functions of time *t*.

To do this, a spatial - mean concentration of electrons and holes across the active layer is defined:

$$\bar{n}(t) = \frac{1}{L}\int_0^L n(x,t)dx$$
$$\bar{p}(t) = \frac{1}{L}\int_0^L p(x,t)dx \qquad (6.1)$$

where *n(x,t)* and *p(x,t)* highlight the dependence of the concentrations of space and time.

In addition, the value $\overline{n_{eq}} = n(\infty)$ is defined as the total carrier concentration in equilibrium conditions, i.e. when all the charges present inside the active layer are only those accumulated at the electrodes. Incidentally, this occurs when the OCVD transient is over, i.e. when the equilibrium is reached and all the photogenerated charges have recombined.

Similarly to $\overline{n(t)}$ and $\overline{p(t)}$, an effective value for the recombination rates was defined:

$$\overline{R_L}(t) = \frac{1}{L}\int_0^L R_L(x,t)dx$$
$$\overline{R_{SRH}}(t) = \frac{1}{L}\int_0^L R_{SRH}(x,t)dx \qquad (6.2)$$

In order to take into consideration the spatial non-uniformity of the concentration during the decay, from the definitions (6.2) the effective values of γ and τ were extrapolated. Their expression always depends on $\overline{n(t)}$ and on $\overline{p(t)}$. Thus:

$$\gamma_{eff} = \frac{\overline{R_L}(t)}{\bar{n}\bar{p} - n_i^2}$$
$$\tau_{eff} = \frac{\bar{n}\bar{p} - n_i^2}{(\bar{n} + \bar{p} + 2n_i)R_{SRH}} \qquad (6.3)$$

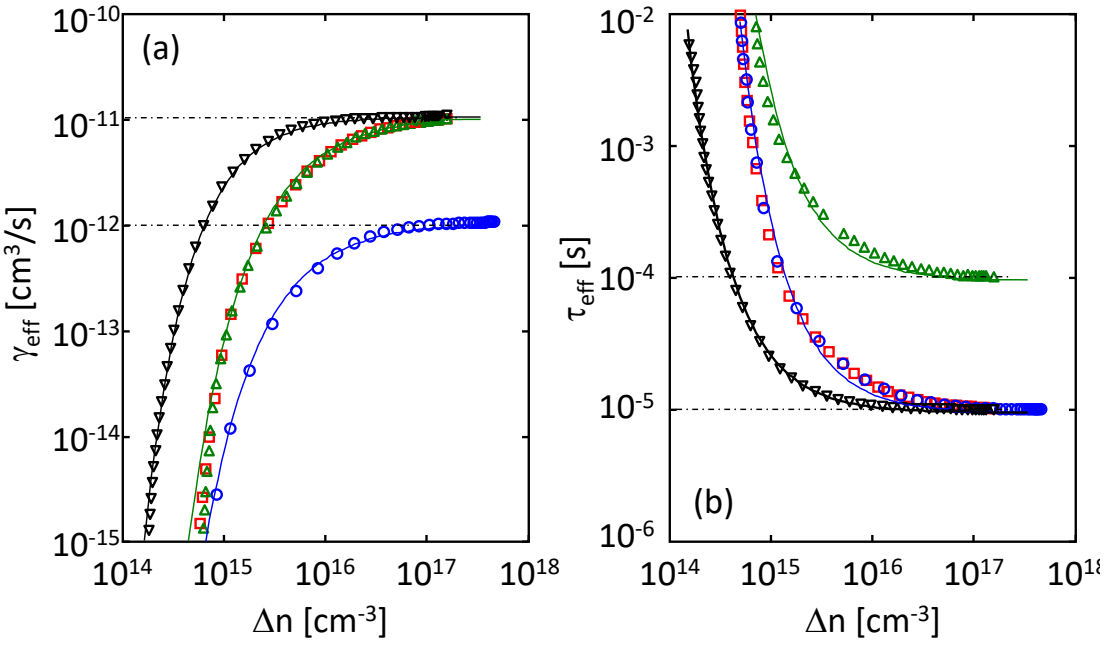

Figure 6.3 Evolution of (a) γ_{eff} and (b) τ_{eff} during the V_{OC} transient. Symbols represent the values of γ_{eff} and τ_{eff} calculated from drift-diffusion simulation using (6.3). Here are shown four sets of parameters, listed in Table 11. Solid lines are the fit obtained using (6.4).

	γ [cm3/s]	τ [s]	Φ_B [eV]
□	10^{-11}	10^{-5}	0.2
○	10^{-11}	10^{-5}	0.2
△	10^{-11}	10^{-4}	0.2
▽	10^{-11}	10^{-5}	0.3

Table 11 Parameters used to simulate the curves shown in Figure 6.3.

When Φ_B (i.e. the difference between HOMO (LUMO) and anode (cathode) work function, see Table 10) is equal at both anode and cathode, as it will be assumed from now on, $\overline{n(t)} = \overline{p(t)}$ and γ_{eff} and τ_{eff} are functions of only $\overline{n(t)}$. Figure 6.3 (symbols) shows the evolutions of both γ_{eff} and τ_{eff} extrapolated from four drift-diffusion simulations as function of $\Delta n(t) = \overline{n(t)} - n_{eq}$ (i.e. the average value of the photogenerated carrier concentration). Each curve represents a simulation performed using the parameter values listed in Table 11.

Independently on the parameters used, the shape of the γ_{eff} curves is similar. The same behavior was found for the τ_{eff} curves. Their evolution can be expressed as an empirical function of Δn:

$$\gamma_{eff} = \gamma \cdot \exp\left(-\left(\frac{N_\gamma}{\Delta n}\right)^{\beta_\gamma}\right)$$
$$\tau_{eff} = \tau \cdot \exp\left(-\left(\frac{N_\tau}{\Delta n}\right)^{\beta_\tau}\right) \qquad (6.4)$$

In these equations, γ is the Langevin constant and τ is the lifetime[12] used in the drift diffusion simulations (supposing $\tau_n = \tau_p$); $\beta\gamma$ and $\beta\tau$ are two empirical damping constants close to 1; N_γ and N_τ are two empirical concentration values.

When Δn is high (i.e. at the beginning of the decay), γ_{eff} and τ_{eff} converge to γ and τ, respectively (this is correct due to the definitions of γ and τ). N_γ and N_τ represent the critical concentration at which γ_{eff} starts to decrease and τ_{eff} to increase.

Note that these expressions are spatially constant and depend only on the average concentrations, which, in turn, depend only on time. In Figure 6.3, the solid lines represent the empirical laws (6.4), which fits the simulated data. The exponential approximation is good for each simulation shown.

At this point, it is worth to remark that γ_{eff} and τ_{eff} represent only empirical functions accounting for the x-dependence of n and p. The real parameters ruling the recombination behavior of the carriers (used in the drift diffusion simulation) are still γ and τ, and they are both supposed space- and time-independent.

Equations (6.4) can be included in the equations that represent the Langevin recombination rate and SRH recombination rate (i.e. $R_L = \gamma(np - n_i^2)$ and $R_{SRH} = \frac{np - n_i^2}{2\tau(n+n_i)}$, supposing $\tau_n = \tau_p$ and $n(x)=p(x)$)) to account empirically for the spatial dependence of n and p.

6.2.3 Effect of model parameters on γ_{eff} and τ_{eff}

In order to illustrate the dependence of γ_{eff} and τ_{eff} on the parameters that characterize the solar cell, several drift-diffusion OCVD simulations were performed using different values for τ, γ, Φ_B and temperature. In these simulations, the parameters are set to what reported in Table 10, unless differently specified. A discussion of the plots presented will be made after the simulation plots.

Figure 6.4(a) shows the simulated V_{OC} decay for different values of γ ranging from 10^{-9}cm^3/s to 10^{-12}cm^3/s, with τ=10μs. The voltage decay was simulated using the expressions of

[12] These parameters represent the value of the Langevin coefficient and of the lifetime when the charge concentration is constant in all the active layer (i.e. at the beginning of the decay).

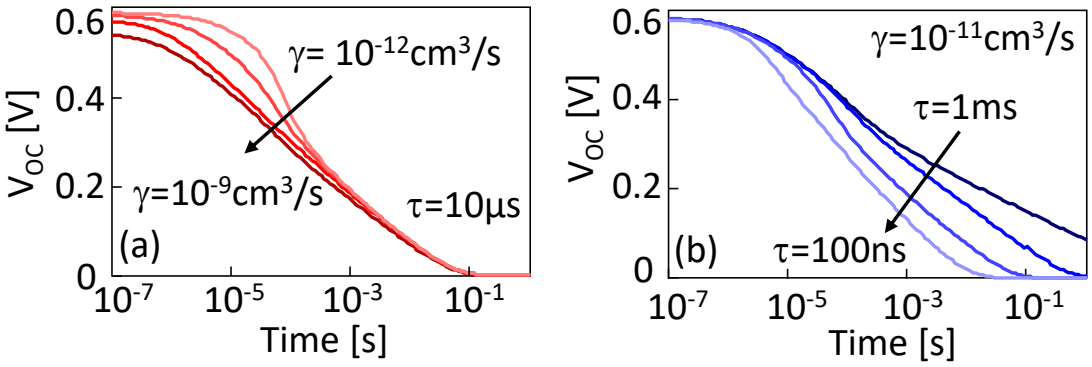

Figure 6.4 Examples of OCVD drift-diffusion simulations. (a) Effect of γ on the V_{OC} transient with τ = 10 μs. (b) Effect of τ on the V_{OC} transient with γ = 10^{-11} cm^3/s. All other parameters are listed in Table 10.

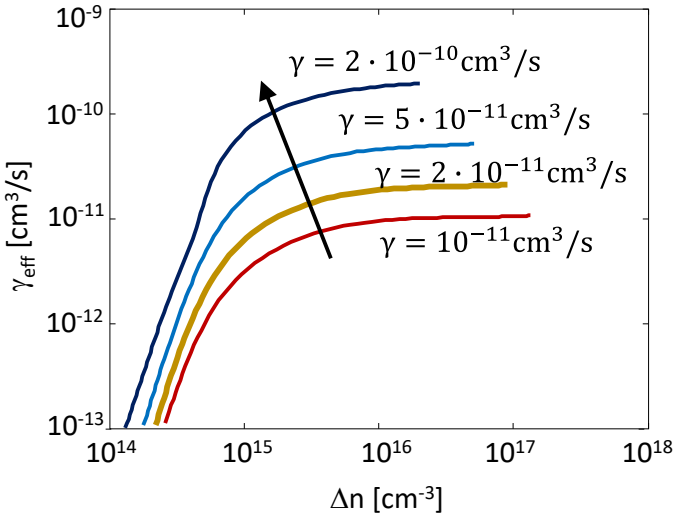

Figure 6.5 γ_{eff} simulated for different values of γ with Φ_B=0.25eV and T=25°C.

γ_{eff} and τ_{eff} found before. The simulation highlights that the higher γ, the faster the voltage decay, in agreement with what discussed in Chapter 5. This is due to the high Langevin recombination rate, which increases with increasing γ. This leads to a fast carrier recombination, and to a consequent V_{OC} faster decrease, even in the first part of the voltage decay. Figure 6.4(b) shows the V_{OC} decay simulated using different values of τ, ranging from $10^{-3}s$ to $10^{-7}s$, and γ = $10^{-11}$$cm^3/s$. According to the previous model, τ only affects the last part of the decay, which is dominated by the SRH recombination, while the first part of the decay does not heavily depend on τ. The only exception is made for the decay simulated when τ is very low (i.e. 100ns), where the charge lifetime is so short that even the first part of the decay is affected by it. Noticeably, this case is purely demonstrative and does not represent any real case, being τ too small to represent a real value (to have a term of comparison, the smallest lifetime associated to the cells analyzed in Chapter 5 is around some tens of microseconds).

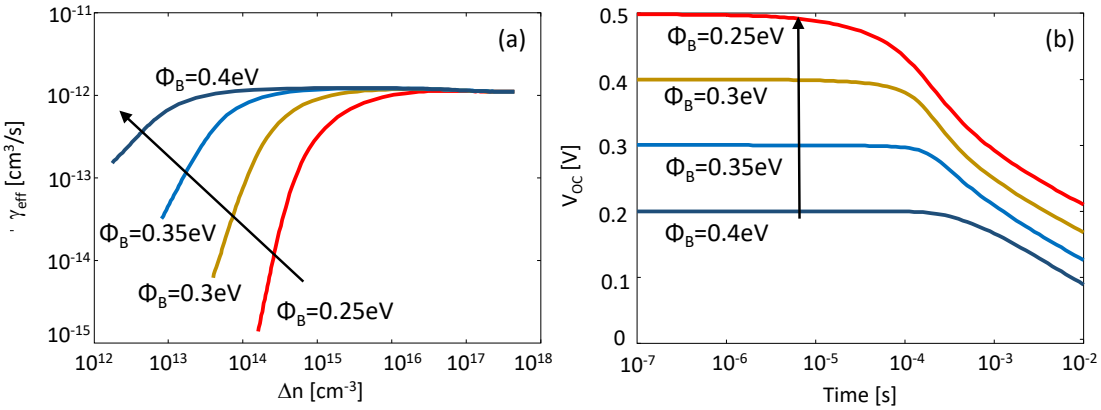

Figure 6.6 (a) Simulation of γ_{eff} at different electrode barrier values ΦB. $\gamma=10^{-12}cm^3/s$ and T=300K. (b) Evolution of the voltage decay for different values of Φ_B. Each curve is obtained using the value of γ_{eff} shown in Figure 6.6 and using the non-constant carrier distribution OCVD model.

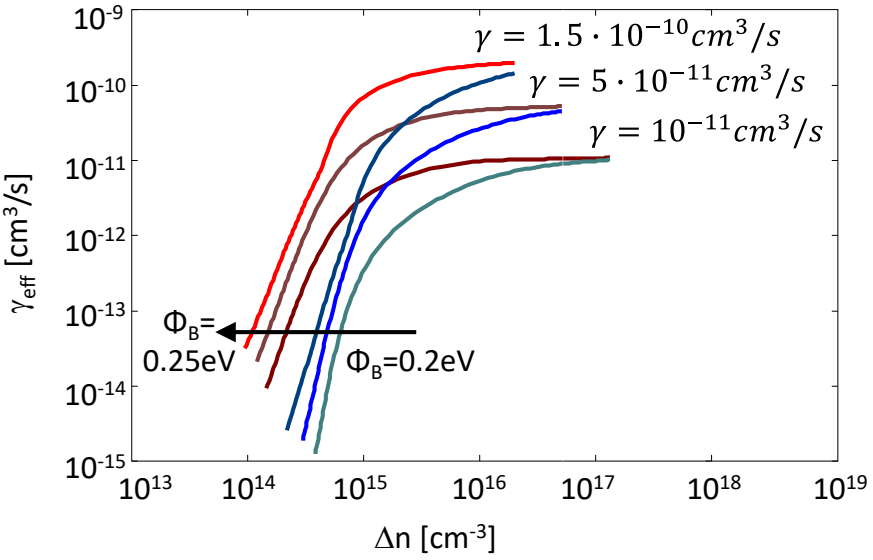

Figure 6.7 Simulation of γ_{eff} at different electrode barrier values ΦB and for different values of γ. Temperature is kept at 300K.

The plots just analyzed confirm what observed in the last chapters, and that the new model shows the same dependence of V_{OC} from γ and τ. The attention will be now focused on γ_{eff} and τ_{eff}, and in particular on their variations with respect to the parameters that characterize the solar cells.

Figure 6.5 shows the simulated evolution of γ_{eff} as function of the carrier concentration inside the active layer for various parameters γ, which ranges from $10^{-11}cm^3/s$ to $10^{-9}cm^3/s$. Remarkably, γ_{eff} tends to γ when Δn is very high (see (6.4)). For this reason, when γ grows, γ_{eff} grows as well. On the contrary, for low carrier concentration, as it is at the end of the decay, γ_{eff} tends to zero, as predicted by the analysis made so far. The corresponding evolution of the voltage decay is similar to that illustrated in Figure 6.4(a) (even if the parameters used for the simulation

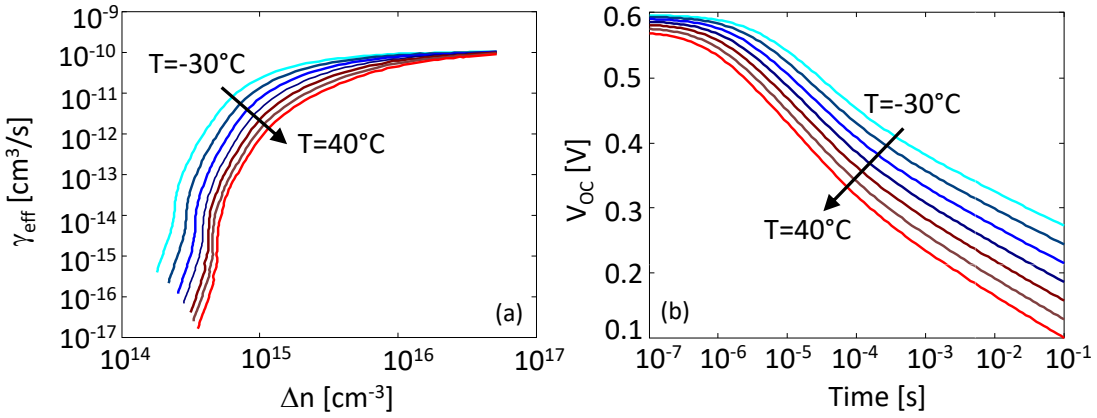

Figure 6.8 (a) Simulation of γ_{eff} at different temperatures. In this case $\gamma=10^{-10}cm^3/s$.(b) Evolution of the voltage decay for different values of temperature. Each curve is obtained using the value of γ_{eff} shown in Figure 6.8 and using the non-constant carrier distribution OCVD model.

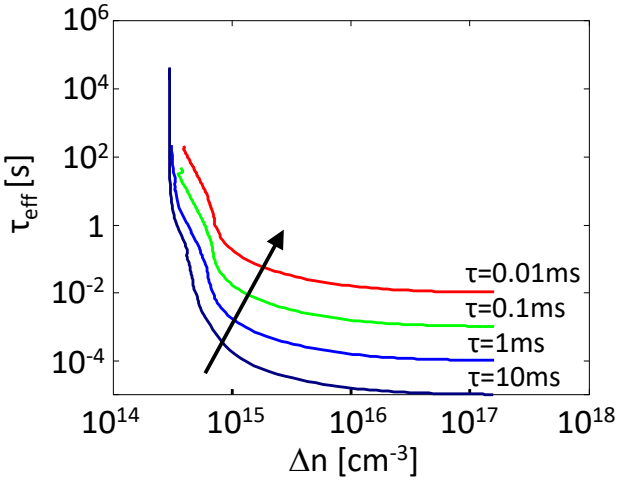

Figure 6.9 Simulation of τ_{eff} at different τ values. In this simulation $\gamma=10^{-11}cm^3/s$, T=25°C, ΦB=0eV.

are slightly different). Furthermore, it has also been verified that the mobilities μ_n, μ_p, and the energy gap E_G do not impact on the shape of γ_{eff}.

The evolution of γ_{eff} is also plotted for different values of ϕ_B, which ranges from 0.25eV to 0.4eV (see Figure 6.6(a)). Clearly, the change in ϕ_B has a strong impact on the position of both N_τ and N_γ, which decrease when ϕ_B increases, inducing a leftward shift in all the curves. The dependence of γ_{eff} on ϕ_B will be further analyzed later. Figure 6.6(b) shows the corresponding variations of the voltage decay. As expected, the only region subjected to change is the region where bimolecular recombination is dominant. In particular, the major parameter to be affected is the initial V_{OC}, which is strictly dependent on the barrier heights.

Combining the variations of both γ and ϕ_B, it is possible to simulate the cumulative effects on the evolution of γ_{eff}, as reported in Figure 6.7. Noticeably, the effect is to shift the curve exactly

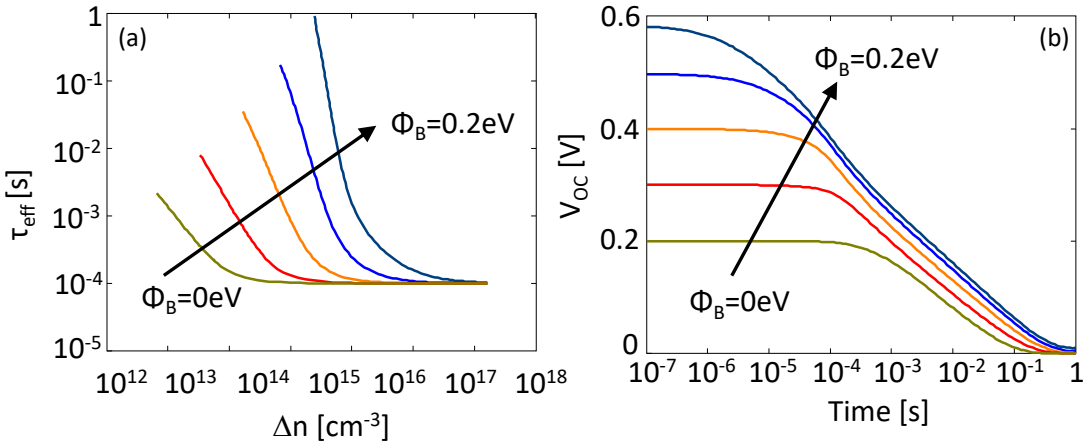

Figure 6.10 (a) Simulation of τ_{eff} at different electrodes barrier values Φ_B. (b) Evolution of the voltage decay for different values of the electrodes barrier. Each curve is obtained using the values of τ_{eff} shown in Figure 6.10(a) and using the non-constant carrier distribution OCVD model.

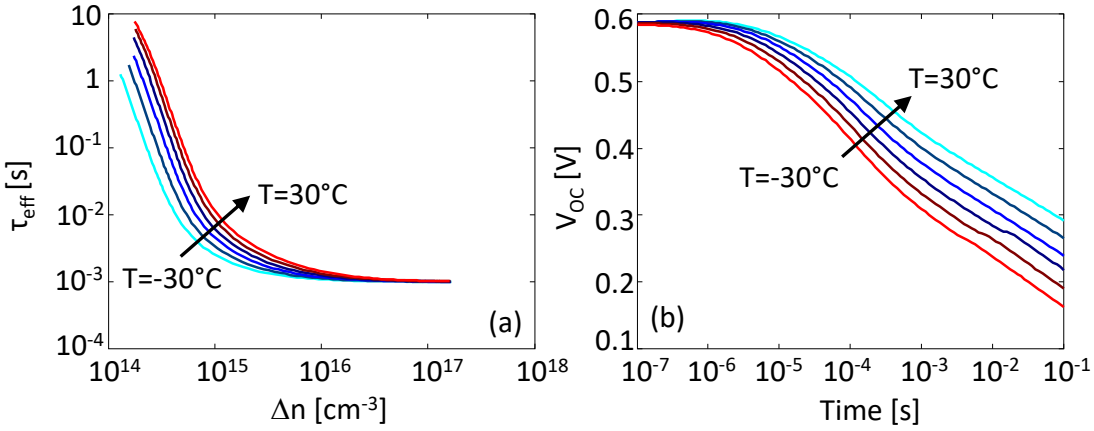

Figure 6.11 (a) Simulation of τ_{eff} at different temperature values. (b) Evolution of the voltage decay at different temperatures. Each curve is obtained using τ_{eff} shown in Figure 6.11(a) and using the non-constant carrier distribution OCVD model.

as happened in Figure 6.5 and Figure 6.6(a), without any further modification in the shape of the curves. This suggests that a change in one of the two parameters is perfectly distinguishable in the analysis of the voltage decay transient.

Temperature heavily modifies γ_{eff} as well, as reported in Figure 6.8(a). If temperature increases, N_γ increases, causing a rightward shifts in the curve when temperature raises from -30°C to +40°C. This suggests that N_γ becomes higher and higher with temperature, determining a lowering in the photocurrent and in the V_{OC} of the solar cell (as observed in the OCVD measurement performed in Chapter 5).

In Figure 6.8(b) is reported the evolution of the voltage decay simulated using γ_{eff} shown in Figure 6.8(a). Noticeably, the curves only shift downward, without modifying their shapes in the

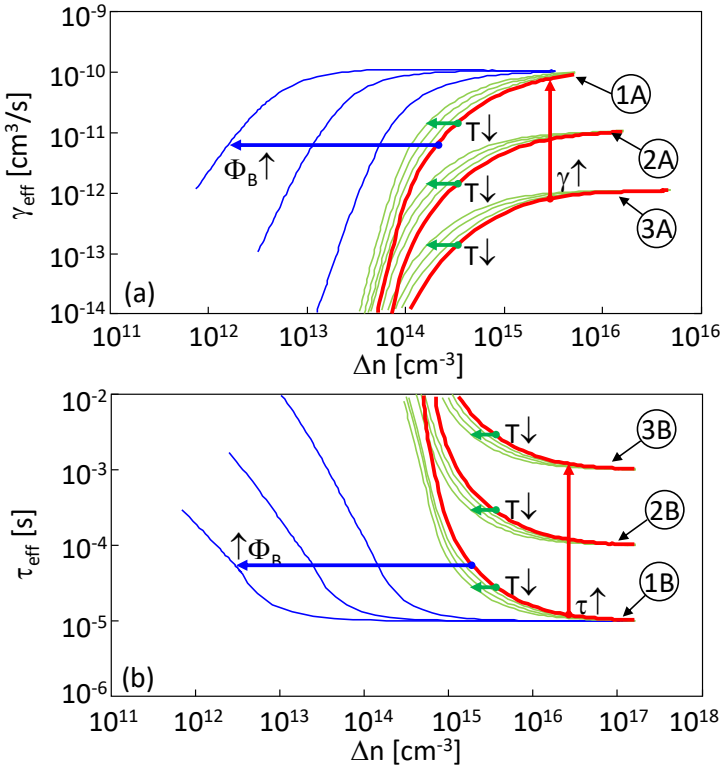

Figure 6.12 Evolutions of (a) γ_{eff} and (b) τ_{eff} as functions of the photogenerated carriers Δn. The simulations are obtained using the default parameters listed in Table 10. The red lines in (a) are obtained for $\gamma = 10^{-12}$ cm^3/s (1A), 10^{-11} cm^3/s (2A), and $\gamma = 10^{-12}$ cm^3/s (3A). The red lines in (b) are obtained for $\tau = 10$ μs (1B), 10 μs (2B), and 1 ms (3B). The blue curves represent the leftward shift of the red curves 1A and 1B when ΦB increases from 0.2 to 0.4 eV (leaving unchanged all other simulation parameters). The three groups of green lines represent the leftward shift of the corresponding red line when the temperature decreases from 300 to 270K (leaving all other parameters unchanged).

second region (where the trap assisted recombination prevails). The first region is only slightly modified, showing that the beginning of the voltage decrease starts earlier with increasing temperature.

A similar analysis can be made on the evolution of τ_{eff}. Figure 6.9 shows the evolution of τ_{eff} for different values of τ. Once more, as expected, τ_{eff} grows for growing values of τ. When $\Delta n >> N_\tau$ (i.e. at the beginning of the decay), τ_{eff} tends to the simulation parameter τ, and it was verified that this happens independently on γ, temperature, ϕ_B, μ_n, μ_p, and E_G.

The voltage decay dependence on τ is the same reported in Figure 6.4(b), even if with some slight changes in the parameters of simulation.

Figure 6.10(a) shows τ_{eff} for different ΦB values. For higher values of ΦB, the curve representing τ_{eff} shifts rightward (i.e. N_τ becomes higher). This implies that the higher the photogenerated carrier concentration present inside the active layer, the higher τ_{eff}. The

corresponding V_{OC} decay transients are shown in Figure 6.10(b). Noticeably, the OCVD decreases slower for higher values of τ_{eff}.

The variation with temperature of τ_{eff} can be observed in Figure 6.11(a), and the corresponding V_{OC} decay is shown in Figure 6.11(b).

Figure 6.12 summarizes all the effects on γ_{eff} and τ_{eff} observed in the last few plots. The red lines marked with 1A, 2A and 3A represent the simulated values of γ_{eff} for different values of γ, with ϕ_B ranging from *0.2eV* to *0.4eV* and *T*=25°C. When Δn decreases below N_γ (i.e. towards the end of the decay), γ_{eff} exponentially decreases. Conversely, when Δn is above N_γ, γ_{eff} saturates to γ, independently from all the other parameters (τ, T and ϕ_B).

The red lines marked with 1B, 2B, 3B in Figure 6.12(b) show τ_{eff} as a function of Δn for different values of τ. In this plot, when $\Delta n << N_\tau$, τ_{eff} increases, while when $\Delta n >> N_\tau$, τ_{eff} tends to the simulation parameter τ, independently on γ, T, ϕ_B, μ_n, μ_p, and E_G.

Noticeably, the extrapolated values of N_γ is very similar to N_τ. Besides, N_γ and N_τ do not depend on γ, τ, μ_n, μ_p, and E_G, but only on ϕ_B and temperature.

A change in ϕ_B has a strong impact on the position of both N_τ and N_γ, which decrease when ϕ_B increases. In fact, the blue lines in Figure 6.12(a) show the variation of curve 1A with ϕ_B increasing from 0.2eV to 0.4eV, and all other parameters unchanged. Similarly, in Figure 6.12(b), the blue lines represent the left shift of curve 1B with ϕ_B increasing from 0.2eV to 0.4eV.

A similar effect is obtained simulating the OCVD at different values of temperature. The three groups of green lines of Figure 6.12(a) and (b) show the behavior of γ_{eff} and τ_{eff} calculated from OCVD simulations at different temperatures. Decreasing T from 300K to 270K, N_γ and N_τ reduces and γ_{eff} and τ_{eff}, represented by the red lines, move left as indicated by the green lines.

As already observed, when the photogenerated carrier concentration dominate over the pre-existing charges, γ_{eff} and τ_{eff} approach their theoretical values γ and τ, respectively[13]. This is due to the presence of a large number of both electrons and holes in the whole active layer, almost uniformly distributed, like in Figure 6.1(b). Conversely, when most of the photogenerated carriers have been already recombined, almost all the carriers inside the active layer come from the charge accumulated near the electrodes. Electrons are mostly concentrated near the cathode, and the holes near the anode. Only few charges co-exist in the center of the active layer, reducing the

[13] The theoretical values are the parameter values imposed at the beginning of the simulation.

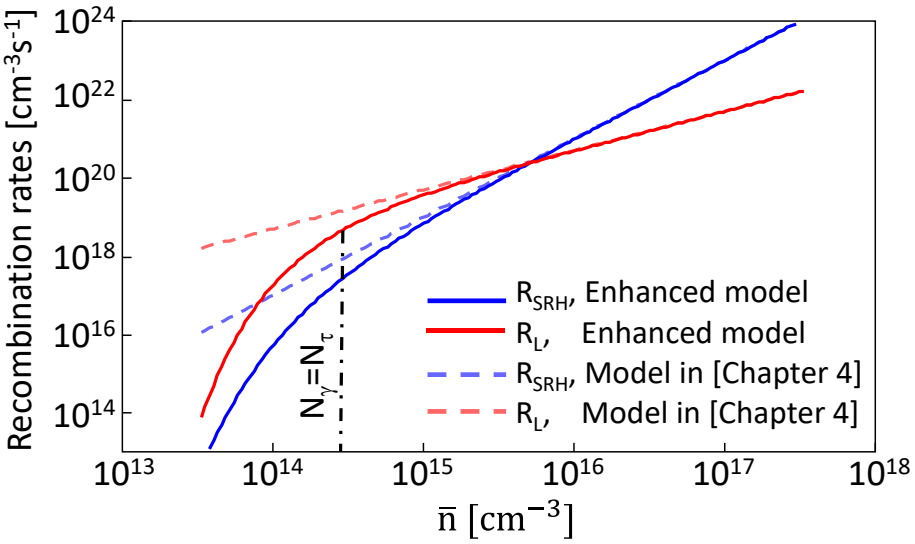

Figure 6.13 Langevin and SRH recombination rate as a function of the average carrier concentration. The dashed lines represent R_L and R_{SRH} calculated with a constant value of γ and τ like was done in Chapter 4 and in [Tor17]. The solid lines represent R_L and R_{SRH} calculated including the variation of τ_{eff} and γ_{eff} as a function of the average carrier concentration (in these simulation $N_\tau = N_\gamma$).

overall recombination efficiency. In the model, this reflects on the reduction of γ_{eff} and on the increase of τ_{eff}.

Figure 6.13 shows the Langevin and SRH recombination rates as a function of $\bar{n}$. The dashed lines are the rates calculated using (4.1) and (4.2) with constant values for $\gamma=10^{-11}cm^3/s$ and $\tau=10^{-5}s$, while the solid lines are calculated including the concentration-dependence of γ_{eff} and τ_{eff} (as was done in Figure 4.7). For both models, the curves representing R_{SRH} and R_L intersect when $\bar{n}$ reaches a threshold value related to the point where the trap-assisted recombination dominates over the Langevin recombination (i.e. $R_{SRH}=R_L$). The model highlights that, when the carrier concentration is small enough, R_L and R_{SRH} decrease faster than in the original model. However, even though both recombination rates become weaker, there is always a point during the decay when SRH recombination starts to dominate over the Langevin recombination. This highlights that, even in this enhanced model, two distinct portions of the decay can be identified: the first is mainly characterized from γ, and the second from τ. These considerations are a consequence of N_γ and N_τ being very similar and independent on the value of γ and τ.

There is an important correlation between the parameters N_γ and N_τ and the pre-existing accumulated charges at the interfaces. This consideration will lead to an important result in the parameters extrapolations of the solar cell. Figure 6.14 and Figure 6.15 show the dependence of N_γ, N_τ and n_{eq} (defined in 6.2.2) on the temperature and on Φ_B. In particular, Figure 6.14 compares the Arrhenius plot of n_{eq} with those of N_γ and N_τ, respectively. Each group of symbols is the result of a simulation made at different Φ_B, ranging from *0.2eV* to *0.4eV* (the values associated to the

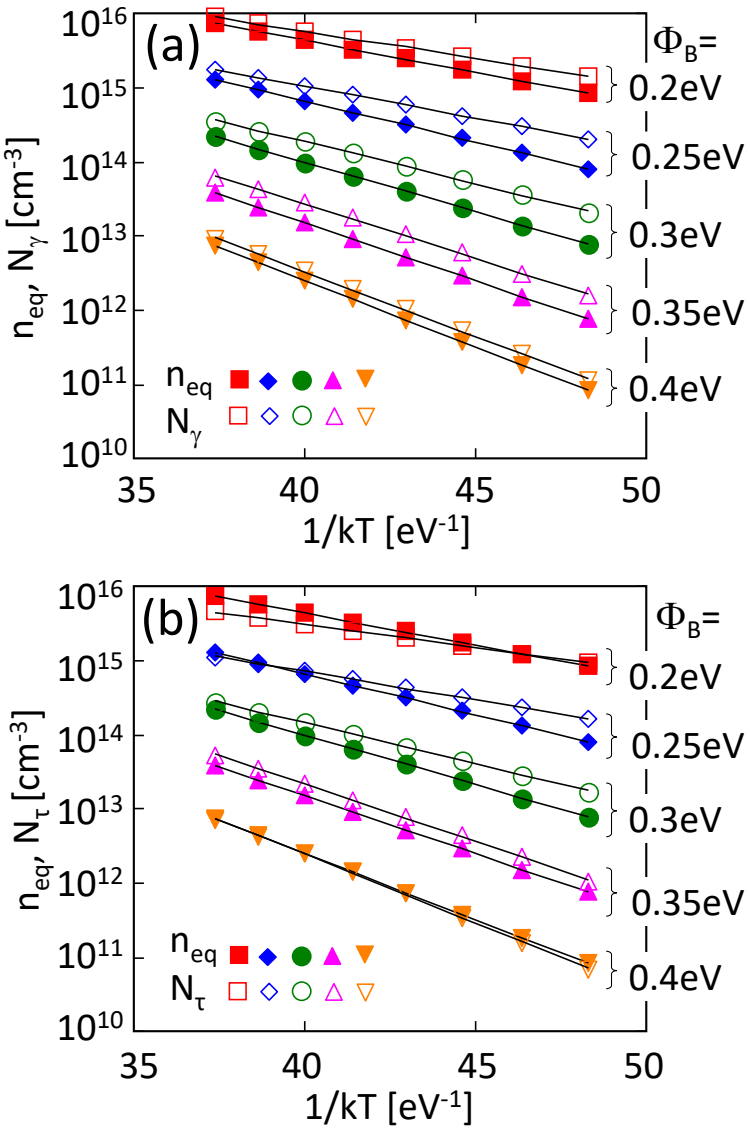

Figure 6.14 a) Arrhenius plot of n_{eq} (closed symbols) and N_γ (open symbols) for five simulations performed with different ϕB, ranging from 0.2eV to 0.4eV. b) Arrhenius plot of n_{eq} (closed symbols) and Nτ (open symbols).

symbols are reported in figure). Note that N_γ and N_τ closely correlate to n_{eq}, and this is even more clear in the correlation plot of Figure 6.15(a), where N_γ and N_τ are plotted as functions of n_{eq} for different and ΦB values (ranging from 0.2eV to 0.4eV). A one to one correlation is observed, highlighting the strong correlation between N_γ, N_τ and n_{eq}.

To quantify approximately the dependence of n_{eq} on Φ_B and temperature, a Sokel-like approach [Sok82] was used to calculate the electron distribution across the active layer, by assuming a constant electric field $F=V_{BI}/L$, where V_{BI} is the built-in voltage.

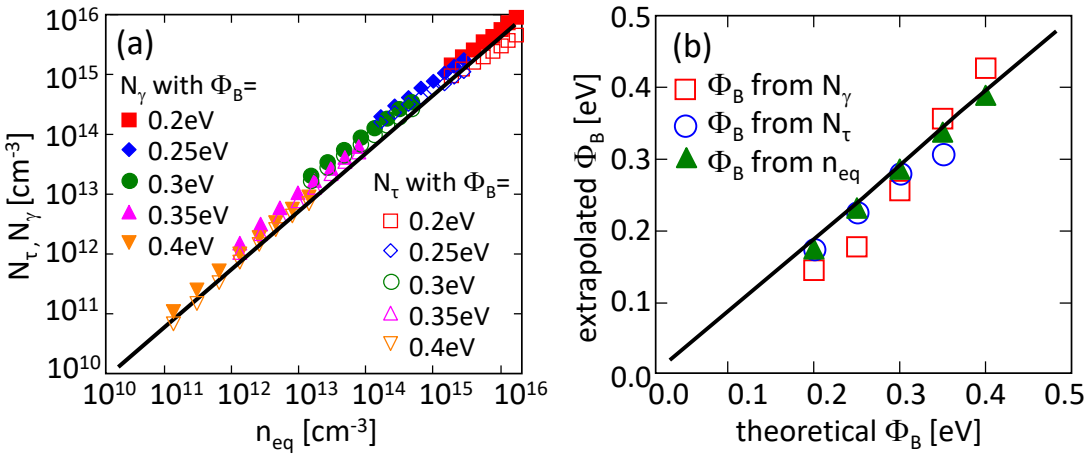

Figure 6.15 a) Correlation between N_γ and N_τ with n_{eq}. Each symbol correspond to a different ϕ_B value. b) Value of ϕ_B extrapolated from the Arrhenius plot of N_γ, N_τ and n_{eq} in Figure 6.13(a) and (b) as a function of the theoretical ϕB used for the simulation. The black, solid line has slope 1.

Following this approach, *n(x)* in equilibrium is approximated[14]:

$$n(x) = N_C \exp(-\frac{\Phi_B}{kT}) \cdot \exp(-\frac{F}{V_T}x) \qquad (6.5)$$

Using the definition given in 6.2.2 it is possible to calculate n_{eq} by integrating (6.5):

$$n_{eq} \cong \frac{N_C V_T L}{V_{BI}} \exp(-\frac{\Phi_B}{V_T}) \qquad (6.6)$$

In these equations N_C represents the effective concentration of states (see also Table 10). n_{eq} depends only on Φ_B and on the temperature[15], while there is no dependence on γ and τ. When Φ_B increases, n_{eq} is expected to decrease exponentially. N_γ and N_τ show the same Φ_B- and temperature-dependence that is exhibited by n_{eq}. This is further confirmed by Figure 6.14 and Figure 6.15(a)).

This correlation between N_γ and N_τ with n_{eq} explains the shift of the green lines and the blue lines in the plots of the simulations shown, as well as the shifts in Figure 6.6, Figure 6.8, Figure 6.10 and Figure 6.11. This correlation confirms that γ_{eff} and τ_{eff} begin to decrease when the photogenerated concentration approaches the value of the pre-existing charges n_{eq}. In other words, both the Langevin and the trap-assisted recombination rates begin to decrease when the average photogenerated carrier concentration Δn approaches n_{eq}.

[14] The equation is valid in inorganic semiconductors. For simplicity, it will be considered valid also for organic semiconductors.

[15] In fact, the thermal potential expression is $V_T=1/kT$, where k is the Boltzmann constant

As a further confirmation of (6.6), in Figure 6.15(b) are shown the values of Φ_B extrapolated from the slope of the Arrhenius plot of N_γ and N_τ in Figure 6.14(a) and Figure 6.14(b). The Φ_B values extrapolated fairly approaches the theoretical Φ_B values used for the drift-diffusion simulation (solid line in the plot).

6.3 Model Validation and band diagram extrapolation

Now that the non-uniform carrier distribution OCVD model has been fully developed, described and discussed, the attention will be focused on its validation using some experimental data. From these data, an application of the model will be shown, also extrapolating some key parameters and the energy gap of the solar cells used.

To validate the model, bulk heterojunction solar cells used in 5.3 were employed. In particular, the cells used are those made of P3HT, P1 and P2 donor polymers, blended with $PC_{61}BM$ as acceptor counterpart.

Figure 6.18 shows the fits of OCVDs taken in the three different OSCs for four different temperatures. Symbols are the experimental data taken from the above-mentioned cells, solid lines are the enhanced model proposed in this chapter. In the fits made in Chapter 5, there were some deviations between model and experimental data due to the simplicity of the model, which assumed that the concentrations inside the active layer were constant. The solid lines of Figure 6.18 show the better quality achieved with the new enhanced model, which strongly reduces the discrepancies in the largest part of the decay (especially until the voltage V_{OC} falls below *0.1-0.2V*, depending on the considered material). Some deviations between the experimental data and the model still appear at the end of the decay, due to some phenomena that were neglected in the model development. Among them, it may be considered the presence of small shunts, the recombination of the charges at the electrodes and the internal conduction of the parasitic diode of the solar cell.

All these phenomena could be reasonably neglected at the beginning of the transient, when Langevin and/or trap-assisted recombination still have a strong impact. However, these effects might not be negligible in the very final portion of the transient, when the recombination rate approaches zero. Of course, the strength of these secondary effects may depend on temperature, and this could explain the different quality of the fit obtained in the experimental data measured at different temperatures.

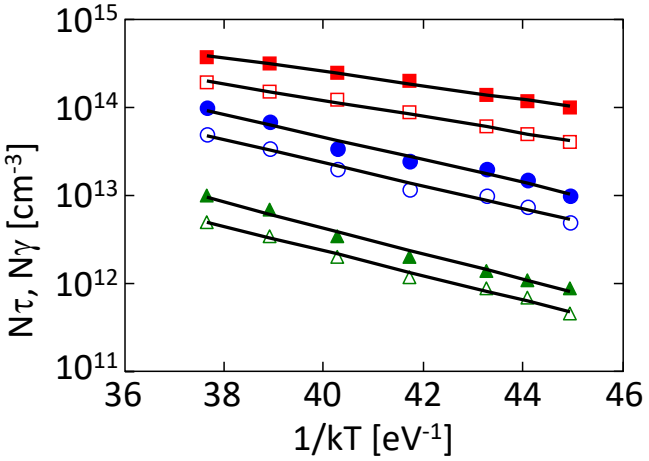

Polymer	Φ_B [eV]
P3HT	0.2
P1	0.3
P2	0.33

Figure 6.16 Arrhenius plot of N_τ and N_γ extrapolated from the fitting of Figure 6.18.

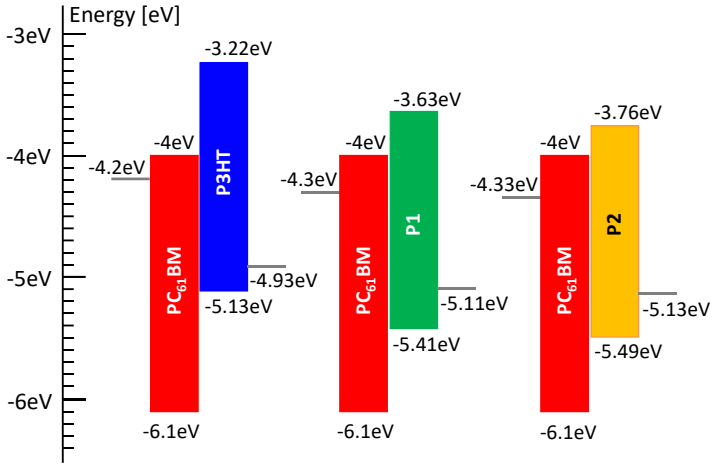

Figure 6.17 Band diagrams of the three devices of Figure 6.18. The energy values are referred to vacuum level.

The Arrhenius plot of Figure 6.16 shows the extrapolated values of N_γ and N_τ fitting the OCVD curves in the three polymers. As expected, N_γ and N_τ are similar, confirming the validity of the approach.

Being N_γ and N_τ almost identical to n_{eq}, from the slopes of the Arrhenius plot of Figure 6.16 it is possible to calculate the alignment between electrode Fermi level and transport bands (Φ_B) using (6.6).

The model presented in Chapter 4 permits to extrapolate only the alignment between the acceptor LUMO and donor HOMO bands. The introduction of a method to take into account the non-constant charge distribution, though, permits to extrapolate N_γ and N_τ, which in turn permit to obtain more important information about the band structure of the device analyzed. This, together with some information about the polymers used, allows to achieve a more comprehensive picture of the OSC electronic band structure.

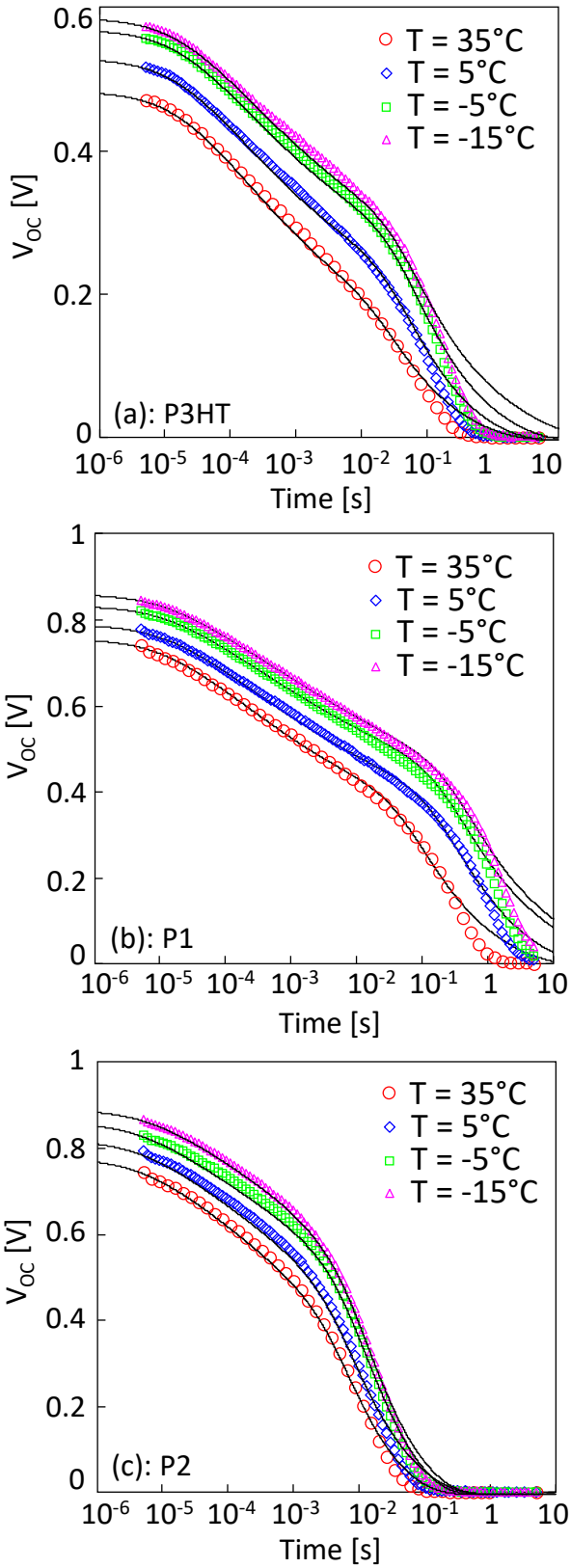

Figure 6.18 Comparison between experimental data taken at different temperatures (symbols) and the enhanced model in three polymers.

This is shown in Figure 6.17, where the entire band diagrams of the same devices of Figure 6.18 is shown. In the three band diagrams, the red box represents the band diagram of $PC_{61}BM$ (which is equal in every device). The other boxes represent the band diagram of P3HT (blue), P1 (green) and P2 (orange). The band diagram of the donor and acceptor materials are put in close proximity one another in order to represent the polymers interface inside the active layer.

In the following it is described the procedure used to draw the diagrams reported in figure. Noticeably, this is only a possible procedure for the extrapolation of the band diagram, and many other options may exist. Most important, though, is the fact that this model allows to gain the alignment between the band diagrams of the materials used in the blend and the electrodes.

The LUMO of $PC_{61}BM$ is used as energy reference, and it is set to -4eV. This is an average estimation obtained by several works reported in literature (see for instance Refs. [Pro16], [Irw17], [Jun11], [Bli14]). The band gap of $PC_{61}BM$ was obtained by [Zhe17].

The energy gap of the donor materials were extrapolated by EQE measurements, as described in Chapter 4, while the energy gap of each blend was calculated from the model. The procedure is identical to that that reported in Chapter 4.

Finally, the band alignment between the electrodes and the corresponding transport bands are those reported in Figure 6.16, and they were calculated by means of this model.

The reported values for Al/LiF work function and for PEDOT:PSS work function are in agreement with those typically reported in the majority of the works present in literature [Pro16], [Irw17], [Jun11], [Bli14]. Also the HOMO of P3HT is in agreement with the values reported in literature, which ranges from -5eV to -5.2eV. Instead, the HOMO of P1 and P2, which are non-conventional polymers, are -5.49eV and -5.41eV, respectively. The HOMO energy level of these two pure donor polymers was measured by cyclic voltammetry (CV), obtaining the same value of -¬5.37eV for both, which is in perfect agreement with other reported works based on nearly identical polymeric structures (See Table S1 in supporting information of [Zhe17]). Furthermore, it is close to the value extrapolated by means of the model. The small mismatch could be ascribed to the small changes that occur once the two polymers are blended with $PC_{61}BM$.

6.4 Conclusions

In this chapter, some drift diffusion simulations were used to analyze the accuracy of the OCVD model described in Chapter 4, which assumed constant parameters and constant carrier distributions inside the active layer during the voltage decay transient. Of course, this was only an

approximation introduced for the sake of simplicity: in fact, during normal operations, the charge distribution inside the active layer is not spatially constant, but changes in time. This was confirmed by the simulations, which also provided a numerical evaluation of the charge concentration during the voltage decay. This is an important information, and it needs to be included in the OCVD model in order to achieve a better precision on the extrapolated parameters.

In order to do this, an effective value of the carrier concentrations during every instant of the voltage decay was considered. This allows to keep the parameters independent on position, and it makes possible to find an empirical relation of the recombination coefficients (which is function of the carrier concentration).

Thanks to the modified model, it was achieved a good accuracy during most part of the V_{OC} transient. In fact the fit becomes much better than the fit obtained with the previous model, even though in the very final part of the decay a small mismatch with the experimental data appears. This might be due to the presence of some neglected phenomena, such as the presence of small shunts, the recombination of the charges at the electrodes and the internal conduction of the parasitic diode of the solar cell. All these phenomena are worth to be considered in a future development of this work.

Despite these approximations, thanks to this enhanced model it is possible to have the complete picture of the electronic band structure of the cell, gaining more information not only on the active layer energy gap (like in the original model), but also on the alignment between the electrode work functions and the transport bands of the active material.

6.5 References

[Bli14] V. N. Bliznyuk, J. Gasiorowski, A. A. Ishchenko, G. V. Bulavko, N. A. Derevyanko, N. S. Sariciftci, “Photoresistance and photo induced current hysteresis in bulk heterojunction systems P3HT–PCBM–polymethine dye”, Organic Electronics, Vol. 15, pp. 1105–1112, 2014.

[Epp13] J. F. Epperson, “An introduction to numerical methods and analysis”, 2nd edition, New Jersey: , Wiley, 2013.

[Irw07] M. D. Irwin, D. B. Buchholz, A. W. Hains, R. P. H. Chang, and T. J. Marks, “p-Type semiconducting nickel oxide as an efficiency-enhancing anode interfacial layer in polymer bulk-heterojunction solar cells”, PNAS, Vol. 105, no. 8, pp. 2783–2787, 2007.

[Jun11] [24] Y. S. Jung, Y.-H. Hwang, A. Javey, and M. Pyoa, “PCBM-Grafted MWNT for Enhanced Electron Transport in Polymer Solar Cells”, Journal of The Electrochemical Society, Vol. 158, no. 3, A237-A240, 2011.

[Pro16] M. Prosa, M. Tessarolo, M. Bolognesi, O. Margeat, D. Gedefaw, M. Gaceur, C. Videlot-Ackermann, M. R. Andersson, M. Muccini, M. Seri, and J. Ackermann, “Enhanced ultraviolet stability of air-processed polymer solar cells by Al doping of the ZnO interlayer,” Appl. Mater. Interfaces, vol. 8, pp. 1635–1643, 2016.

[Sok82] R. J. Sokel and R. C. Hughes “Numerical analysis of transient photoconductivity in insulators”, J. Appl. Phys., vol. 53, no. 11, pp. 7414-7424, Nov. 1982.

[Tor17] L. Torto, A. Cester, L. Passarini, A. Rizzo, N. Wrachien, M. Seri, M. Muccini, “Open circuit voltage decay as a tool to assess the reliability of organic solar cells: P3HT:PCBM vs. HBG1:PCBM” in Proc. IEEE-IRPS, Monterey, CA, USA, 2017, pp. 2F2.1-2F2.10.

[Zhe17] Z. Zheng, O. M. Awartani, B. Gautam, D. Liu, Y. Qin, W. Li, A. Bataller, K. Gundogdu, H. Ade, and J. Hou, “Efficient Charge Transfer and Fine-Tuned Energy Level Alignment in a THF-Processed Fullerene-Free Organic Solar Cell with 11.3% Efficiency”, Adv. Mater., Vol. 29, 1604241, 2017.

Chapter 7 **Conclusions**

This work was focused on the analysis of the hetero junction solar cells (also named polymeric solar cells), which are a subset of the wide field of organic solar cells. The analysis provided the description of an innovative measurement technique (the Open Circuit Voltage Decay, OCVD) together with the extensive development of a new analytical model capable of extrapolating some key parameters of the solar cell. These parameters are useful to gain information about the degradation of the devices and about their strengths and weaknesses. Thus, the OCVD measurement and model have been used to analyze and discuss several samples. In addition, the photocurrent produced by these solar cells has been analyzed and discussed by means of another analytical model, which has been developed and described in this work as well.

Both models have proven important tools for cells characterization and qualification, and they have been also used during reliability tests, to monitor the degradation of the cells by means of electrical, noninvasive measurements such as OCVD and photocurrent measurement).

The first model discussed was the photocurrent model, and it allowed to estimate the effect of a voltage drop at the cells electrodes and, consequently, the effect on the internal electric field. In particular, this allowed to explain why the position of the built in voltage does not correspond to the point of zero photocurrent, as supposed by the previous models. The voltage at which the photocurrent nullifies has been identified as *zero field voltage*, and it has been demonstrated that it strictly depends on a charge accumulation close to the electrodes, which are responsible for the already mentioned voltage drop. Thanks to the model, it was also demonstrated that the band bending at the electrodes plays only a minor role as a barrier in the transport of charges toward the contacts. The height of such barriers plays an important role in the shape of the photocurrent density vs. voltage characteristics. On the contrary, it has been

demonstrated that the band bending shape have only a marginal role in the photocurrent dependence on voltage. This allowed to use the modification of the photocurrent shape as an indicator of the degradation of a solar cell interface under test. In fact, it has been shown that such degradation reflects on the appearance of multiple inflections in the photocurrent shape. This is an important fact because it allows to directly understand what characteristic of the solar cell is degrading. Furthermore, this methodology of analysis is directly applicable to the device under operating conditions, corroborating the usability of the photocurrent model.

The second model developed is the OCVD model, and it is capable of fitting the open circuit voltage decay in polymeric solar cells. This measurement monitors the open circuit voltage decay transient starting from the moment when the incident light on the solar cell is turned off. To develop the model it has been taken into account the contribution of both the bimolecular recombination and the trap-assisted recombination for free charges. Thus, the model gave information about these two mechanisms. In addition, from OCVD performed at different temperatures on several organic solar cells, the model permitted to extract the value of the energy gap of the blend starting from the estimation of the intrinsic charge distribution. In turn, this value was obtained from the information brought by the study of the recombination mechanisms.

In the last chapter, it was presented an improvement to this model in order to take into account the contribution of non-constant carrier distribution inside the active layer during the voltage decay transient. In order to do this, some supporting drift diffusion simulations were made. This allowed to define a new parameter to include the effects of non-constant charge distribution into the expression of bimolecular and trap-assisted recombination rates. This allowed to achieve a better fit accuracy during most part of the V_{OC} transient and to a better precision of the extrapolated parameters. Furthermore, the extrapolation of the whole device band diagram was obtained. Remarkably, this is a very important result. In fact, the estimation of the band diagram of an entire organic materials-based device is very difficult due to the presence of dipoles that may alter the alignment between the bulk region bands and the electrodes work functions.

Combining the two models, several experimental results have been analyzed and discussed. Particular attention was paid to the accelerated stress-induced evaluation of the devices degradation, and to the differences shown by devices made with different materials.

The experimental analysis was focused on two case studies.

- The first case was focused on devices characterized by the same structure, but with different active layer donor polymers.

- In the second case we focused on the reliability devices with a standard P3HT:PCBM active layer.

The analysis of the first group gave information about the main limiting factors behind the low performances of some devices. For instance, among the analyzed polymer-based solar cells, it was found that some of the devices had good photovoltaic properties, which are even better than the properties of standard P3HT:PCBM devices. Interestingly, for other types of devices, the generation capability has been evaluated to be very high, even though the polaron pair separation probability was relatively low. This was related to the high Langevin recombination coefficient and, to a lesser degree, to a non-optimal energy band alignment of the polymers in the blend.

The accelerated electrical stresses performed on the first group of solar cells evidenced that the electrical stress is responsible for the photocurrent reduction and for the increase of the free carrier recombination rate. Of course, the effect is more observable in some devices rather than in others. In particular, one of the different cells showed a better resistance to thermal stress if compared to the other types of devices. In fact, it shows low degradation even at relatively high reverse bias stress. This is an example of application of the model: it can be applied to different solar cells to find which one of them is that made with the most reliable or most performing structure or material.

The second group of solar cells was analyzed by means of several thermal and electrical stress procedures. The analysis suggested that the electrical stress in forward bias condition mainly generates defects in the active layer, lowering the photocurrent. This is responsible for the decrease of polaron generation, for the reduction of the polaron probability separation, and for the decrease of the carrier lifetime.

On the other hand, the thermal stress has the effect of lowering the photocurrent due to the modification of exciton generation and recombination rate. Furthermore, it induces the already mentioned change in the photocurrent shape, due to the degradation of the anode interface, which causes a local band bending growth at the anode.

The cells that underwent accelerated reverse bias stresses during illumination showed a photocurrent that could be fitted with the modification of only the generation and separation probability. Only minor changes could be observed in the band bending heights, Φ_{Bp} and Φ_{Bn}. This points that at least 100°C is needed in order to produce significant degradation at the contact interface. Besides, it has been observed that a stress performed in forward condition is more damaging than a stress performed in reverse bias condition. This analysis was confirmed by the results obtained by means of OCVD measurements regarding the carrier recombination inside the

active layer. Furthermore, the OCVD analysis allowed to relate the decrease of some solar cell parameters to the presence of the defects inside the active layer. In particular, it was discovered that the defects located closely to the interfaces between the two active layer polymers mainly act on the increase of the polaron pair recombination, while the defects located in the bulk regions of the active layer act as quenching sites for excitons.

The results described in this work are very useful to understand how an organic solar cell works, and they allow to evaluate with a high precision the cells characteristics, its weaknesses and its strengths. Nevertheless, there are still some investigations that are required to be done in order to gain a full understanding of the device working mechanisms.

One of these further investigations regards the Open Circuit Voltage Decay measurement. In particular, it would be very interesting to further analyze the first microseconds of the voltage decay, using a very fast voltage sampling. This would allow to understand which other phenomena are involved in the voltage decay, especially those closely related to the presence of excitons inside the active layer. In order to do this, it would be necessary to employ a measurement tool capable of a very fast sampling (for example 5ns per sampling). Furthermore, the model for the OCVD analysis presented in this work should be extended, including the effects of the photogenerated excitons.

Furthermore, it would be desirable to investigate the behavior of solar cells made of many other materials, comparing their performances and understanding which of them lend a better durability to the device. In particular, it would be very useful to extend this work to hybrid materials-based device (such as Perovskite – based devices). Being these devices very different from the polymeric-based devices presented in this work, the work would require a strong effort. Nevertheless, this is an essential work that has to be done in order to facilitate the development of new devices based on new materials.

In conclusion, this work provides some important tools to characterize the polymeric solar cells, as it was clearly demonstrated applying them to several experimental results. Being them very suitable for reliability analysis, their usefulness can be appreciated during the development of the organic solar cells. In fact, they are very important to study the devices weaknesses, allowing to fix those problems that may become not negligible during ageing, and that may bring to the devices failure. Furthermore, the analytical approach to extrapolate the experimental data may be employed even after a possible commercialization of the polymeric solar cells. In fact, the

measurements on which the models are based are non-invasive and non-destructive, and they permit to continuously monitor the health of the device.

Without any doubt, it has been shown that still many efforts need to be done in order to improve the reliability of hetero junction solar cells and organic solar cells in general. The analysis developed in this work, though, provides several important instruments to achieve this goal and to support strongly the investigation for more reliable materials and structure for the photovoltaic device.